Doctoral (Ph.D.) Thesis

Application of layered double hydroxide nanoparticles to combat oxidative stress

Adél Szerlauth

Supervisor:

Dr. István Szilágyi

Associate Professor

Doctoral School of Chemistry

MTA-SZTE "Momentum" Biocolloids Research Group

Department of Physical Chemistry and Materials Science

Faculty of Science and Informatics

University of Szeged

Szeged

2024

Table of contents

List of Abbreviations

AFM	Atomic force microscopy
Alg	Alginate
ASP	Adsorption saturation plateau
ATR	Attenuated total reflectance
BHA	Butylated hydroxyanisole
BSA	Bovine serum albumin
CAT	Catalase
CCC	Critical coagulation concentration
CCT	Critical coagulation time
Cys	Cysteine
DLS	Dynamic light scattering
DLVO	Derjaguin, Landau, Verwey, Overbeek
DMEM	Dulbecco's modified eagle medium
DPPH	2,2-Diphenyl-1-picrylhydrazyl
dSTORM	Direct stochastic optical microscopy
EC_{50}	Effective concentration
EDL	Electrical double layer
ELS	Electrophoretic light scattering
FAT	Fixed analyzer transmission
FBS	Fetal bovine serum
FLIM	Fluorescence lifetime microscopy
GPx	Glutathione peroxidase
GSH	Glutathione
GSSG	Glutathione disulfide
HEPES	4-(2-hydroxyethyl)-1-piperazineethanesulfonic acid
HNT	Halloysite nanotube
HR	High resolution
HRP	Horseradish peroxidase
IC_{50}	Inhibitory concentration
IEP	Isoelectric Point
IR	Infrared spectroscopy
LbL	Layer-by-layer
LDH	Layered double hydroxide
NBT	Nitro blue tetrazolium
PBS	Phosphate buffer
PEI	Poly(ethylene imine)
PDI	Polydispersity index
ROS	Reactive oxygen species
RNS	Reactive nitrogen species
SAXS	Small angle X-ray scattering
SEM	Scanning electron microscopy
SOD	Superoxide dismutase
TA	Tannic acid
TBHQ	*Tert*-butylhydroquinone
TCSPC	Time-correlated single photon counting
TEM	Transmission electron microscopy
TG-MS	Thermogravimeter coupled mass spectrometry
TIRF	Total internal reflection fluorescence
TMC	Trimethyl chitosan
XPS	X-ray photoelectron spectroscopy
XRD	X-ray diffractometry

1. Introduction

Reactive oxygen species (ROS) (*e.g.,* hydrogen peroxide (H_2O_2), hydroxyl radical ($^{\bullet}OH$), superoxide radical ($O_2^{\bullet-}$)) play an important role in many vital physiological processes in living organisms. They play a crucial role in cellular signaling, differentiation, and regulation of cell death. However, when their concentration increases above normal levels, oxidative stress occurs leading to lipid peroxidation, DNA damage, protein denaturation, and many other severe consequences that are responsible for the development of serious diseases such as cancer. To maintain optimal ROS levels, they are balanced with antioxidants.

Antioxidants are molecules of various structures and sizes that can prevent or delay ROS-induced harmful effects. Natural antioxidants have many different sources, they can be extracted from plants such as fruits, vegetables, and herbs. Based on their structure, they are divided into two main groups: enzymatic and molecular antioxidants. Enzymatic antioxidants possess a well-defined protein structure, some with a catalytically active metal ion in their active site, which is responsible for the antioxidant activity. The best-known representatives are superoxide dismutase (SOD), glutathione peroxidase (GPx) and catalase (CAT), which are responsible for the degradation of the superoxide radical anion and hydrogen peroxide. Molecular antioxidants include, *e.g.,* polyphenols, carotenoids and vitamins which can react with ROS by electron transfer, H-atom transfer, or complexation.

Protection against ROS is required in many biomedical and industrial fields. Product shelf life is important in industrial applications, such as paints, fuels, plastics, cosmetics, and food, where antioxidants are important additives. For instance, they are applied in cosmetic industry, endowing the products with anti-aging properties and extending their shelf life. In addition to industry, there is a great potential for antioxidants to be used in some biomedical treatments. Several research activities were devoted to the development of antioxidant coatings for implants, or antioxidant treatments for various inflammatory conditions (*e.g.,* inflammatory bowel disease). However, antioxidants have a major drawback; they are sensitive to environmental conditions (*e.g.,* pH, temperature, light) and mostly have limited solubility, which makes their use difficult. To overcome such problems, many researchers attempted to improve their stability and robustness by immobilizing molecular and enzymatic antioxidants.

Layered double hydroxides (LDHs) served as potential host materials for the immobilization of antioxidants. LDHs have a brucite-like ($Mg(OH)_2$) structure, with the

difference that divalent cations are partially replaced by trivalent ones. This phenomenon, the so-called isomorphous substitution make the layers positively charged, which is compensated by hydrated interlayer anions. In addition to the original lamellar structure, the delaminated form (dLDH) has also been extensively studied in the last decades. Nowadays, many different synthesis strategies are known for the preparation of dLDHs, and their structural modification has also been comprehensively studied. Due to the useful properties of LDHs and dLDHs (*e.g.,* remarkable anion exchange capacity, tunable structure, biocompatibility) their applications have attracted great attention in many fields (*e.g.,* catalysis, support materials, environmental remediation). Their tunable structure offers the possibility of incorporating metal ions, originally located in the enzyme active centers, into the layers. Furthermore, the anion exchange capacity enables the intercalation of biomolecules among the LDH layers, while surface modification offers the possibility of anchoring antioxidants, which is also a promising method to produce heterogeneous antioxidant systems.

Development of artificial enzymes is also a possible solution to address the above mentioned problems. Nowadays, several researchers work on the design of so-called nanozymes, which can be defined as nanoparticles of enzyme-like potential. The first nanomaterials with unexpected enzyme-like characteristics were metal-based nanoparticles and since then, several different syntheses were developed to produce nanozymes with a wide range of shape, size and composition. Eliminating natural enzymes from the industrial processes can make the antioxidant treatments cost-effective, while nanoparticles also have a lower sensitivity towards harsh environmental conditions compared to natural enzymes.

Heterogenization of antioxidants did not overcome all challenging problems. Accordingly, nanoparticles should be well homogenized and form a stable colloidal dispersion when used in a liquid phase. Therefore, studying and improving the colloidal properties of such antioxidant dispersions is an important issue in the preparation of heterogenized antioxidant systems. For instance, polyelectrolytes, *i.e.,* highly charged polymer chains, can be adsorbed on the nanozyme surfaces to stabilize their dispersion. Functionalization with polyelectrolytes can prevent particle aggregation processes and thus, produce fine, processable colloidal dispersions. The preparation of such a stable dispersion is a critical issue in many applications, both in industrial and biomedical fields.

2. Literature Review

2.1. Reactive oxygen species and antioxidants

ROS and reactive nitrogen species (RNS) are formed as free radicals and highly reactive molecules by both endogenous and exogenous processes from molecular oxygen and nitrogen species (Figure 1). Their production can be enhanced by exogenous sources, like UV- or ionizing radiation, air pollution and cigarette smoke, but endogenous processes such as the mitochondrial electron transport chain and inflammatory processes also contribute to their formation.[1] The three main known ROS molecules are the hydrogen peroxide (H_2O_2), the superoxide radical anion ($O_2^{\bullet-}$) and the hydroxyl radical (•OH). The mitochondrial electron transport chain or the oxidation reaction of NADPH by enzymes are responsible for the formation of $O_2^{\bullet-}$, which is then converted to H_2O_2 by SOD. Under normal conditions, they are present at a regulated level, but the increase of their concentration can lead to molecular damage. The increased H_2O_2 concentration can react with transition metal ions forming •OH, which can easily cause lipid peroxidation.[2] It is worth noting if ROS/RNS is present in normal concentrations in living organisms, they play an important role in many physiological processes.[3] However, when there is an increase in their concentration beyond their expected levels, oxidative stress can occur giving rise to many serious problems, such as lipid peroxidation, DNA damage and protein denaturation.[4]

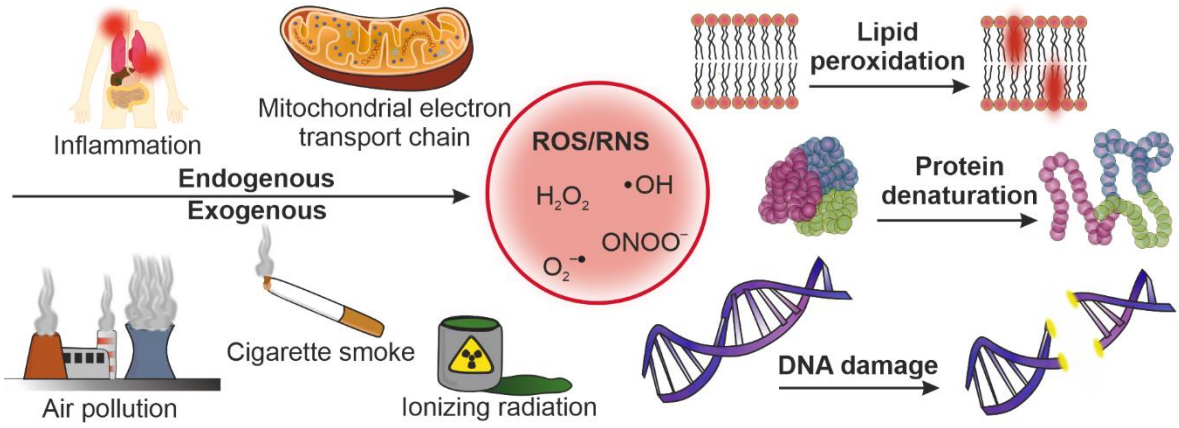

Figure 1. Schematic representation of some endogenous and exogenous sources of ROS/RNS and ROS/RNS-induced diseases.

To avoid the development of oxidative stress, living organisms have built an antioxidant defense system to regulate the concentration of ROS and thus, the formation of oxidative stress. Antioxidants are molecules that can delay or prevent the oxidation of another substrate.[1] One way to classify antioxidants is by their solubility, *e.g.,* water soluble

and liposoluble antioxidants. Besides, they can also be grouped by their source. Some antioxidants are external, while many are produced in the living organisms and hence they are internal antioxidants. The most common distinction is based on their structure. Enzymatic antioxidants have a well-defined protein structure, while molecular representatives are organic molecules such as vitamins, carotenoids, and phenolic acids.[5] A comprehensive interpretation of enzymatic and molecular antioxidants is presented in the following subsections.

2.1.1. Molecular antioxidants

Molecular antioxidants can be divided into two main groups: natural and synthetic antioxidants.[6] Synthetic antioxidants have been developed to mimic the activity of natural antioxidant molecules. They are mainly used in the food industry to extend the shelf life of various food products. The most known representatives are butylated hydroxyanisole (BHA), butylated hydroxytoluene, *tert*-butylhydroquinone (TBHQ), propyl gallate and octyl gallate. In commercial products, BHA is used to control fatty acid oxidation, while TBHQ is present in many edible animal fats, vegetable oils and meat products. However, combined use is also a popular method because of its synergistic effect. In recent decades, efforts were made to replace them by natural antioxidants.[7]

Natural antioxidants have many sources, such as fruits,[8, 9] vegetables,[10] teas,[11] herbs[12, 13] and seeds[14] and they include vitamins, flavonoids, phenolic acids, carotenoids, tannins and several other organic molecules.[6, 7] The most known representatives of vitamins are vitamin C and vitamin E, which are able to protect lipids from lipid peroxidation processes by terminating the chain reactions of lipid peroxidation. After the reaction occurred, vitamin C becomes a very stable radical. It can also neutralize the radical form of vitamin E, which is produced during the reaction with lipid peroxyl radicals.[15] Flavonoids have many biological activities, such as anti-allergic, antiviral and also anti-inflammatory effects. Moreover, they can act as antioxidants. Namely, they can interfere with the normal operation of ROS producing enzymes (*e.g.,* xanthine oxidase, protein kinase C), chelate metal ions which are responsible for the formation of •OH radicals and reduce highly reactive ROS molecules by hydrogen atom donation.[16] Tannins are high molecular weight phenolic compounds derived from plants.[17] They are also known as antinutrients, because they can precipitate proteins and inhibit enzymes and vitamins. However, they have several beneficial biological properties, such as anticarcinogenic, antimicrobial and also antioxidant

activity. Similar to the previously mentioned natural antioxidants, they can decompose the ROS molecules by reducing them, chelate metal ions, and inhibit enzymes in a secondary way.[18]

In addition to the antioxidants already described, glutathione (GSH), a thiol antioxidant, also has major impact in living organisms. It was found not only in plants, but also in animal and human cells; it is present in high concentrations in the cytosol, nuclei, and mitochondria. GSH can act as a cofactor for important intracellular enzymes (e.g., GPx), it is able to reduce ROS molecules, involved in amino acid transport and can regenerate vitamin C and vitamin E after their antioxidant action. GSH transforms into glutathione disulfide (GSSG) upon operation and therefore, the GSH/GSSG ratio could serve as a potential marker for oxidative stress.[1, 19]

2.1.2. Antioxidant enzymes

Enzymes are catalytically active tertiary protein structures with molecular weight in the range of 5 000 – 5 000 000 Da. Tertiary proteins are composed of 3-dimensionally arranged polypeptides (α-helix, β-sheet, β-turn, random coil), derived from α-amino acids. The catalyzed reaction takes place in the active site of the enzyme, called the active centre.[20] The structure of the active site defines the substrate that can bind to the enzyme, its shape and charge allow high specificity for the substrate molecule. It is worth noting that although most enzymes are composed only of proteins, many of them require cofactors for optimal function. Both organic and inorganic molecules can act as cofactors, and in the case of the former, the essential part can also be called a coenzyme (*e.g.,* nicotinamide adenine dinucleotide). Three theories are known for substrate binding, the "lock and key hypothesis", the "induced fit model" and the "conformational selection" theory. The first hypothesis assumes a perfect fit of the substrate molecule, while the second assumes that the active site is flexible enough to fit the substrate.[21] The "conformational selection" claims that there is a substrate-induced specific conformation change of the enzyme protein structure that enables a highly selective interaction with the ligand.[22] Many biological processes are catalyzed by enzymes, and the main role of them is to reduce the activation energy and thus, accelerate the reaction. The substrate molecule binds to the active center, and after the reaction terminated, the product leaves the active site.[22, 23]

In addition to the molecular antioxidants already mentioned (*Chapter 2.1.1.*), antioxidant enzymes are also involved in combating oxidative stress. The three main known

antioxidant enzymes in living organisms are SOD, CAT and GPx.[24, 25] They operate with cofactors such as copper(II), zinc(II), iron(III) and selenium and are involved in scavenge of ROS molecules. SOD was first described by Irwin Fridovich and Joe M. McCord in the 1960s.[26] There are three types of SOD enzyme in the human body; Cu/Zn-SOD in the cytosol, Mn-SOD in the mitochondria and extracellular SOD. The main function of SOD enzyme is to convert the highly active $O_2^{\bullet-}$ radical into O_2 and H_2O_2 (Figure 2). Mn-SOD is essential for the normal operation of the human body, but Cu/Zn is not.[25] The Cu/Zn type is also present in other mammals, Gram-negative bacteria, and in plants, while Mn-SOD and Fe-SOD are found in various types of bacteria.[27]

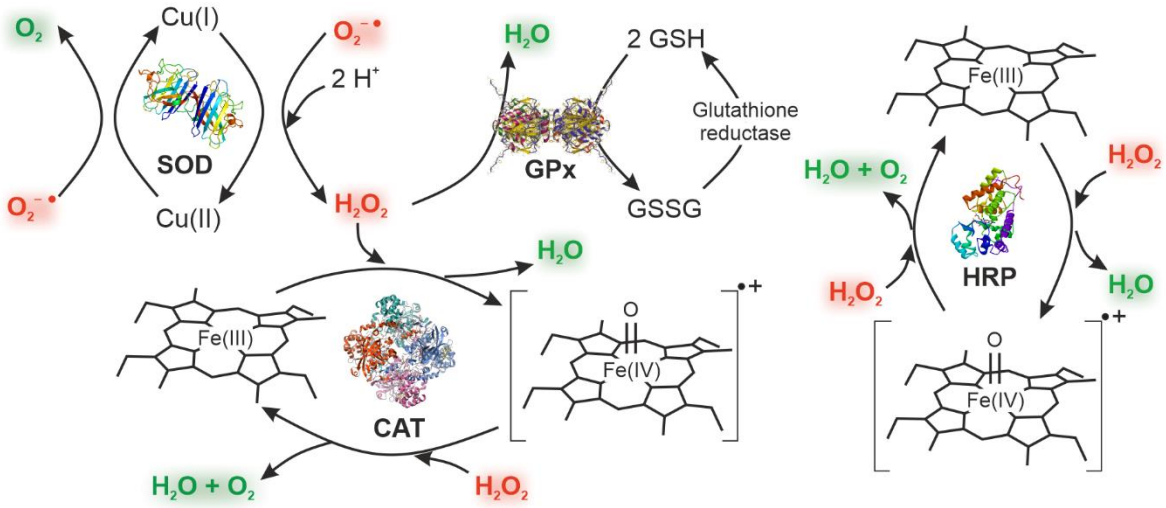

Figure 2. The mechanism of SOD, CAT, GPx and HRP antioxidant enzymes.

CAT is composed of four subunits, each with the catalytically active protoporphyrin (heme) moiety.[28] It can enable the degradation of H_2O_2 to H_2O and O_2, which occurs in a two-step mechanism (Figure 2). Therefore, H_2O_2 molecule reacts with the heme subunit to form a porphyrin radical cation, which then reacts with a second H_2O_2 molecule, regenerating the original heme unit and producing H_2O and O_2.[25] Since the 1980s, the existence of a non-heme containing CAT-type was also confirmed and obtained from many types of bacteria. It is less sensitive to azide and cyanide inhibitors and also responsible for the degradation of H_2O_2.[29] GPx also reduces H_2O_2 to water and oxygen and also responsible for the degradation of other hydroperoxides (Figure 2). To maintain catalytic activity, each noticed subunit contains selenocysteine residues, while GSH is an essential cofactor for the normal function of GPx. During its operation, reaction with peroxide leads to the formation of selenenic acid, which is then regenerated to its original form by GSH in several substeps.[30]

In addition to CAT and GPx, a plant-based enzyme, namely horseradish peroxidase (HRP), also possesses excellent peroxidase activity (Figure 2). Similar to CAT, HRP also contains a heme residue supplemented by two calcium atoms connected by hydrogen bonds. The presence of the calcium atoms significantly affects the normal operation of HRP, as the loss of these atoms results in a loss of enzyme activity and thermal stability. As a peroxidase enzyme, it converts H_2O_2 into water in several substeps.[31]

2.1.3. Application of antioxidants

There is an increased contemporary interest in the application of natural antioxidants in various industrial and biomedical fields (Figure 3). The ROS scavenging effect of antioxidants can be used in the food,[32-36] cosmetic,[37-39] polymer,[40, 41] and oil[42-44] industries, as well as in several biomedical applications.[45-48]

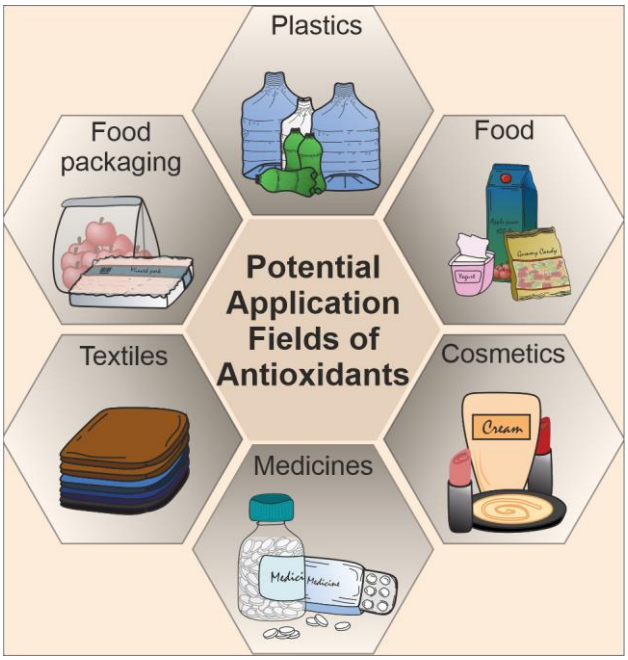

Figure 3. Schematic representation of the potential application areas of antioxidants.

Nowadays, synthetic antioxidants are still more favorable in the food industry than their natural counterparts because they are more stable, of higher performance, more cost-effective, and widely available. Despite the former advantageous properties, safety concerns about synthetic antioxidants have been raised over time, and several research focused on their replacement with natural antioxidants. However, the strict safety regulations applied in the food industry do not facilitate their use.[33] Antioxidants typically serve in the food industry as preservatives, to inhibit color changes and extend shelf life,[49] or as additives in bioactive films[50] and food packaging that protect food from enzymatic browning and oxidative rancidity.[51]

Cosmetic products containing antioxidants have several beneficial effects on the skin. These antioxidants are in the form of natural extracts such as cocoa, green tea, pomegranate or grape extract, which contain various types of antioxidant molecules. These extracts are a source of several dietary antioxidants such as catechins, galloyl residues and polyphenols,

which may have antimicrobial, anti-inflammatory, and anticarcinogenic properties in addition to their antioxidant effects.[39] SOD is also a popular additive in cosmetics because it can prevent hair greying, promote hair growth, reduce wrinkles and hyperpigmentation, and also has an anti-aging effect.[52]

Natural antioxidants are also common additives in polymers to improve their stability. Polymer oxidation occurs under the harsh conditions encountered during their production, when free radicals are generated what can result in chain scission reactions, crosslinking or autocatalysis of oxidation.[40] Based on polymer research data reported to date, flavonoids are better stabilizers than the industrially applied hindered phenolic antioxidants. However, several issues affect the effectiveness of antioxidants in industrial polymer production nowadays. [40, 41] In addition, the application of antioxidant enzymes is an essential step in the commercial production of textiles. CAT is used in bleach cleaning processes, while other peroxide enzymes are able to remove the excess dye in the appropriate manufacturing steps.[53, 54]

Besides industrial processes, biomedical treatments are important applications of antioxidants. For instance, ROS induced oxidative stress is significantly associated with ischemic stroke. The brain is very sensitive to ROS-induced damage and thus, administration of exogenous antioxidants may be a potential treatment for ischemia-related brain injury. Several free radical scavengers (*e.g.,* lipoic acid, N-acetylcysteine, edaravone, GSH monoethyl ester) are in clinical or preclinical testing for the treatment of stroke; however, the use of these compounds remains to be addressed (e.g., therapeutic time window, dose, administration route).[45] Many studies found that oxidative stress is an important pathophysiological factor for inflammatory bowel disease in humans. Therefore, several research efforts are focused on the antioxidant treatment of gastrointestinal inflammation.[46-48] In clinical studies, supplementation of SOD also showed promising results in ROS-induced processes. During the normal operation of SOD, H_2O_2 is also formed. Therefore, in some studies, the use of SOD was combined with CAT to eliminate the excess amount of H_2O_2.[52]

Apart from the fact that antioxidants are promising additives in many applications, their use has some limitations due to their disadvantageous properties (e.g. solubility problems, sensitivity to environmental conditions). Their immobilization on host materials can overcome these problems. One of the best known host materials are layered double hydroxide (LDH) particles, which are presented in the followings.

2.2. Layered double hydroxides

LDHs are usually presented as hydrotalcite-like materials or as anionic clays. Both names refer to their structural properties, i.e., LDHs have a brucite-type [$Mg(OH)_2$] structure with slight modification, and they also contain anions in the interlayer space. Since the 1960s, interest in LDH research has been growing. More and more scientists are studying the structural aspects, structural modification, and potential applications of LDH particles.[55]

The structure of LDH is similar to brucite, however, divalent metal cations are partially replaced by trivalent metal ions. The schematic representation of a typical LDH particle is shown in Figure 4. The metal ions are surrounded by an octahedron formed by hydroxide ions, while the octahedrons are connected along their edges to form a sheet. The metal hydroxide sheets stack on top of each other to build up the lamellar structure. The positive excess charge of the layer forming sheets, which results from the isomorphous substitution, is compensated by the interlayer hydrated anions. The general formula of an LDH is: $[M^{2+}_{1-x}M^{3+}_{x}(OH)_2]^{x+}[A^{n-}]_{x/n} \times y\ H_2O$, where M^{2+} and M^{3+} are di- and trivalent metal cations, respectively, while A^{n-} are the interlayer anions.[56] LDHs have several advantageous properties. Their structure is easily tunable, the metal ion composition is widely variable, while the interlayer anions are also exchangeable.

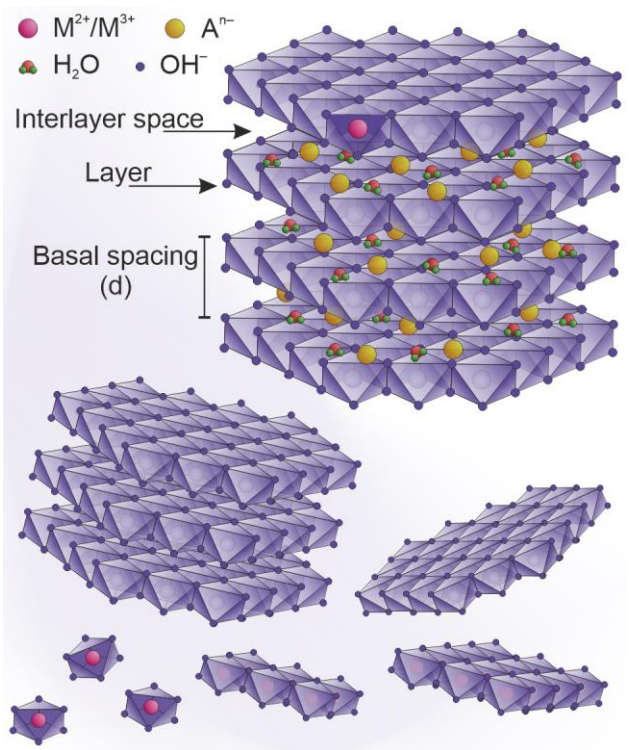

Figure 4. Schematic representation of the structure of an LDH particle.

Several methods are known for the preparation of LDH particles. The most common synthesis technique is the coprecipitation approach, in which a metal salt solution containing di- and trivalent metal cations is mixed with an alkaline solution to form LDH particles in the mixture. The urea hydrolysis method is another possible synthesis technique that uses urea as an ammonia and carbonate source to precipitate metal ions as hydroxides.[55] In addition, the sol-gel method employs hydrolysis of alkoxide precursors and is particularly

well suited for the preparation of nanoscale particles or LDH thin films.[57] The structure of LDHs is highly tunable, they can be synthesized in different M(II)/M(III) compositions, moreover, the interlayer anions can also be changed. Several LDHs with various metal ion compositions have been synthesized, the most common divalent metal cations are from Mg, Mn, Fe, Co, Ni, Cu and Zn, and the most common trivalent ones are from Al, Mn, Fe, Co, Ni, Cr and Ga. In addition, more specific compositions (e.g., Cd/Cr, Mg/In, Ba/Fe), LDHs containing M(IV) metal ions (e.g., Ni/Ti, Fe/Ti), and ternary/multinary LDHs have already been prepared in addition to binary systems.[58] There are several ways to modify the LDH structure after synthesis, *e.g.,* anion-exchange, hydrothermal treatment, or the calcination-rehydration process. Anion-exchange provides the opportunity to replace the intercalated anions with other negatively charged ions or molecules. Hydrothermal treatment proposes a better lateral size distribution, while rehydration also offers the possibility to intercalate suitable negatively charged molecules among the layers. In addition, both methods can control the surface area and the porosity of LDHs.[59]

2.2.1. 2D layered double hydroxide nanosheets

Beside the understanding of the fundamental properties, modification and potential application of layered materials, their delamination and exfoliation became a new research area in 2D materials science. The flagship in this field is graphene, the exfoliated form of the layered graphite structure.[60] In addition, clay minerals also consist of stacked layers that form a lamellar structure. In recent decades, several methods have been worked out to delaminate these structures and create nanosheets with large specific surface area, which is a critical point in many applications.[61]

Adachi-Pagano et al. was the pioneer in delamination of Zn_2Al LDH particles using dodecyl sulfate as an anionic surfactant and butanol as a solvent. After anion exchange, the interlayer Cl^- was replaced by dodecyl sulfate molecules leading to an expansion of the basal spacing. The intercalation of organophilic anions, like fatty acid salts or anionic surfactants, may give rise to the weakening of the van der Waals interactions between the layers and/or hydrated anions and thus, to a stronger hydrophobicity of the interlamellar space enhancing a more favored interaction with non-aqueous solvents. These properties can lead to the exfoliation of LDH particles.[62, 63] Since the first described exfoliation process, several other strategies have been published. The synthesis methods can be divided into two groups: top-down and bottom-up methods. In the top-down method, the distance between the layers is

first increased by the intercalation of a large anion, whereupon exfoliation takes place, while the bottom-up technique is based on the direct synthesis of single layered nanosheets. The delamination processes are usually based on the intercalation of surfactants, the application of a polar solvent, the use of mechanical effects (*e.g.,* ultrasound treatment) or a combination of these methods.[64, 65] Formamide is a commonly used solvent for the preparation of delaminated LDH particles. The synthesis is usually supported by ultrasonic treatment, but the intercalation of amino acids could also support the delamination processes induced by formamide.[66-68] Other direct synthesis procedures are also used for the production of exfoliated LDH particles, like ammonium solution-induced preparation[69] and lactate-assisted exfoliation mechanisms.[70]

Beside the comprehensive investigation of delamination processes, the restacking of unilamellar LDH nanosheets in solid form has also been extensively studied. In most reports, the original form of LDH was restored by evaporation or freeze-drying.[63, 71-73] However, restacking can also be achieved by the addition of a polar solvent or multivalent anion in colloidal dispersions of the nanosheets.[67, 74] Notably, the restacking phenomenon and mechanism were mostly studied in solid state. However, LDHs are often used in colloidal dispersions, so it is necessary to investigate the restacking processes in colloidal systems in more detail.

2.2.2. Application of layered double hydroxides

The aforementioned advantageous properties of LDHs (*e.g.,* tunable structure, anion exchange capacity, cost-effective preparation, biocompatibility) have led to their wide range of applications in various fields. LDHs or their composites can be used in water remediation, catalysis, polymer or sensor technology, ceramics, biomedical treatments and also in electro-photoactive materials.[64, 75]

Heavy metal pollution has become an increasing problem as they pose a threat to animals and, via the food chain, to humans due to their bioaccumulation. Many scientists are therefore focusing on the removal of such contaminants from wastewaters. In addition to various nanomaterials studied, clay minerals have come to the forefront of interest in recent decades (Figure 5). Due to their structural variability, high specific surface area and ion exchange capacity, lamellar and exfoliated/delaminated LDHs have been proposed as potential candidates for this purpose.[76-79] MgAl LDH and its delaminated counterpart were tested in Cr(VI) removal processes. The results showed that the MgAl LDH nanosheets are

the most efficient ones to remove Cr(VI) due to their higher specific surface area caused by delamination. The mechanism relied on adsorption and reconstruction of the original layered structure, during which intercalation of Cr(VI) occurred due to the in-situ formation of negatively charged Cr(VI)-containing complex anions.[76] In another study, LDH particles modified with cysteine (Cys) were used to improve the removal of Cu(II), Pb(II) and Cd(II) pollutants. Accordingly, –SH group in Cys is a soft base, capable of forming primary chemical bonds with soft metals to form M – S bound. As a result, Cys-LDH showed a higher affinity to metal ions and was therefore more effective in wastewater treatment than the unmodified LDH particles.[79] In addition to the former systems discussed, several other types of LDHs have been used for the removal of arsenic,[77] nitrate and dichromate ions,[78] ionic dyes,[80] but also for the removal of emerging contaminants, such as nanoplastics.[81-83]

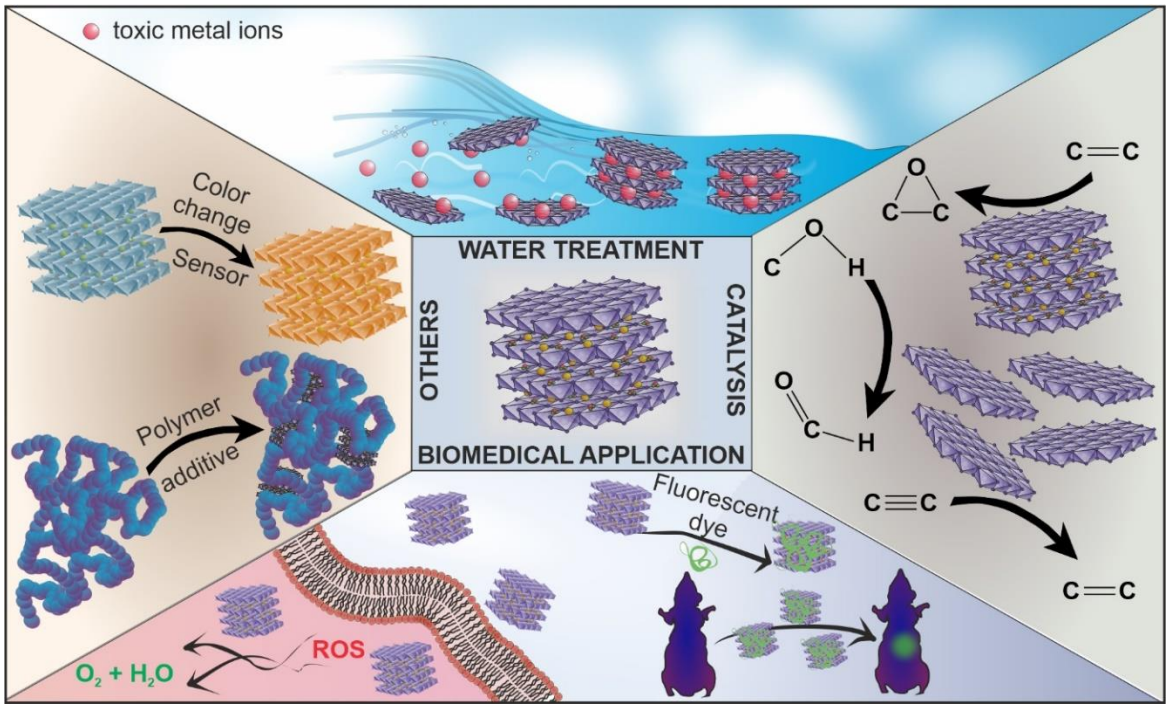

Figure 5. Schematic representation of the possible applications of LDH nanoparticles.

Numerous studies have focused on the application of LDHs as catalysts in various catalytic processes (Figure 5). One of the most common is epoxidation reaction, which originally take place under harsh conditions. However, the use of LDH as a heterogeneous catalyst could be a potential tool to facilitate this process. LDHs with different compositions[84, 85] and also with intercalated Mn-amino acid complex[86] have already been investigated and proved to be effective in epoxidation reactions. Nowadays, electrochemical oxygen evolution reactions (OERs) are considered as a potential source of renewable energy. The potential catalytic properties of NiFe and CoFe LDHs in OERs have been widely

studied,[87-89] but also Ru-doped CuCr LDHs[90] showed high catalytic activity in such reactions. Beyond the two examples mentioned so far, different types of LDHs have been shown to be potential catalysts also for various photocatalytic reactions[91-93] and for other organic reactions.[94, 95]

The most relevant application field to the present work is the potential use of LDHs in biomedical processes (Figure 5). Due to their biocompatibility, bio-related applications attract widespread contemporary attention.[96-98] The most common research areas related to the biomedical application of LDHs concern bioimaging, drug delivery and tissue engineering.[98-100] Despite their numerous advantageous properties, conventional materials for bone tissue engineering (*e.g.,* hydroxyapatite, polylactic acid, chitosan, collagen) do not have osteoinductivity or the ability for drug delivery. Therefore, there is a need to develop therapeutic bone scaffolds that possess these properties to improve bone regeneration. LDHs could act as drug carriers in such scaffolds, in addition, the Mg(II) ions in the LDH structure can also play an important role in bone metabolism. When incorporating LDH particles intercalated with pifithrin-α into a chitosan matrix, the obtained composite showed promising performance in bone tissue regeneration increasing osteoinductivity.[101] Magnesium could serve as a next-generation biomedical material; however, its clinical application is hindered by corrosion. LDH provides a potential solution to this problem. Coating Mg implants with LDHs makes the surface more resistant to corrosion, and Mg/Zn/Al LDH also has an antibacterial effect due to the release of Zn.[102] As mentioned before, LDH can also serve as a drug carrier. Several types of drugs have been intercalated among LDH layers or anchored on the LDH surface so far, to improve stability, and efficacy of drugs or to control their distribution and release.[103-106] LDHs could serve as carrier particles for anti-inflammatory,[103, 107] antibiotic[106] and anti-cancer[108, 109] agents. There are numerous cases where antibiotics would be more effective if they were located directly at the site of infection. Combining them with LDH particles and incorporating the composites into polymeric matrices can therefore dictate their localization in living organisms and control their release, thus improving the treatment of microbial diseases.[110] In addition, the combination of drugs/molecules for joint activity is a common tool in biomedical applications. In cancer treatment, co-immobilization of anti-cancer drugs and biomarkers is a common method to combine drug delivery with bioimaging, in which the active ingredient and the fluorescent molecule is simultaneously anchored on the LDH particle.[111, 112] The immobilization of antioxidants in/on LDH particles is also an important area of LDH research, which will be detailed in the next chapter.

2.2.3. LDH-based antioxidant systems

As discussed earlier, considerable research activity has focused on the scavenge of ROS molecules by antioxidants. However, several antioxidants are sensitive to environmental conditions (e.g., pH, temperature, light), so it is necessary to increase their stability and control their release, water solubility and efficacy. Among others, LDHs were reported to be appropriate carriers for intercalation or adsorption of antioxidant substances (Figure 6).[113]

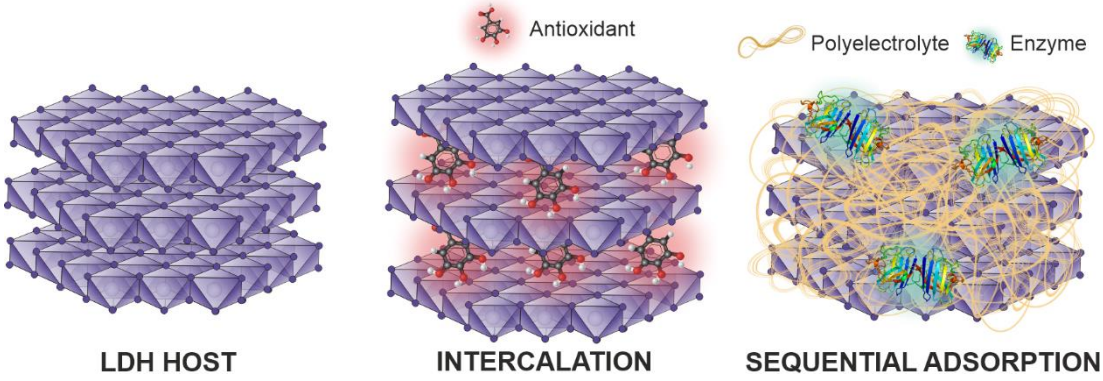

Figure 6. Schematic representation of the immobilization techniques on LDH host materials

LDHs served as protective carriers against environmental influences, like temperature and light or improved limited water solubility of the antioxidant molecules by encapsulating them. Ellagic acid is a phenolic compound that has excellent free radical scavenging activity, but its applicability is hindered by its poor water solubility. LDH layers allowed the host materials to mask its lipophilic character and offers the possibility of using them at higher concentrations in aqueous media. However, its activity decreased after intercalation, organic solvent treatment could improve the free radical scavenging activity, thus it seemed to be a promising material for industrial and medical applications in aqueous media.[114] Antioxidants are common additives in polymers to prevent polymer degradation. However, their main disadvantages are sensitivity to light and heat as well as migration. By intercalating Irganox 1425, a phenolic compound, into the LDH interlayer space and using the composite as an additive in the polypropylene matrix, the thermal stability and the antioxidant anti-migration ability were improved, extending the shelf life of the polymer.[115] The intercalation of 3-(3,5-di-tert-butyl-4-hydroxyphenyl) propionate into the LDH interlayer gallery endowed polypropylene with similar properties, and was able to enhance its thermal stability and extend its shelf-life.[116, 117] Gallic acid (GA) was also stabilized within LDH layers. The GA was intercalated by the restacking mechanism of the delaminated LDH

nanosheets. Upon intercalation, GA was released from the interlayer gallery in a controlled manner. Moreover, it was also more resistant to UV irradiation, approximately twice as many GA remained active after immobilization than in native form.[118] In addition to the formerly mentioned antioxidant-LDH composites, vanillic acid, glutathione and ferulic acid were also intercalated into the LDH interlamellar region to control their release and thus, localize their antioxidant action.[119-121]

Another potential anchoring technique on LDH particles is the layer-by-layer (LbL) technique (also known as sequential adsorption), which has become a widely investigated area approach in the past few decades to prepare multicomponent materials and thin films. The method is based on the adsorption of oppositely charged polyelectrolyte layers on the surface of interest, building up a tunable characteristic. The immobilization of polyelectrolytes can be based on electrostatic interactions, hydrogen bonding, coordination bonding, charge transfer, hydrophobic interactions, or a combination of these. Nowadays, the LbL technique is one of the most popular methods for functionalizing nanoparticles to immobilize enzymes and proteins and to control and modify permeability and release. Another unique feature of the LbL technique is the adsorption of different types of enzymes and thus, the possibility to produce composites with multienzymatic activity.[122-124] SOD and HRP have already been adsorbed on LDH surface individually[125, 126] and altogether by the sequential adsorption method.[127] The adsorption of SOD on the LDH surface was based on electrostatic interaction between the positively charged LDH surface and the negatively charged enzyme. The adsorption was confirmed by Bradford test, indicating that no SOD remained in the solution phase. The immobilized SOD maintained its radical scavenging activity, moreover, the polyelectrolyte layer adsorbed on the outer surface of the composite increased its stability.[126] HRP was similarly anchored on LDH surface. However, since LDH has a net positive charge, the charge of LDH was first tuned by heparin adsorption, resulting in negatively charged particles. Thereafter, positively charged HRP (isoelectric point ~ 8.8)[128] could be anchored on the heparin-coated particles and there was a negligible difference in activity between native and immobilized enzyme. In addition, the composite kept its influence over 6 days, which is important in many applications.[125] To combine their effect, SOD and HRP were adsorbed simultaneously on the LDH surface separated by polyelectrolyte layers. Both enzymes remained active and the cascade showed remarkable ROS scavenging ability in cellular measurements.[127] HRP was also immobilized on the LDH surface parallel with gold nanoparticles, however, the simultaneous adsorption did not prove

to be efficient, as the gold nanoparticles had an inhibitory effect on the normal operation of the HRP enzyme.[129]

2.2.4. LDH-based nanozymes

Although the immobilization of molecular or enzymatic antioxidants in/on LDHs is a common method to endow nanoparticles with radical scavenger activity, artificial enzymes without the use of natural representative have been intensively investigated in the past decades. Nanozymes are nanoparticles with enzymatic activity that can be divided into two subgroups. Type I nanozymes are the aforementioned immobilized enzymes on a solid support, while type II nanozymes derived their activity from the nanoparticle without any enzymatic modification. In the first half of 2000s, most studies dealing with nanozymes investigated type I nanoparticles, while in 2022 the study of type II nanozymes became more popular.[130] Type II nanozymes of antioxidant effects are discussed below.

Several natural enzymes do not possess metal-containing components and do not require metallic cofactors for optimal working conditions. Therefore, in addition to metal oxide and metal sulfide materials, non-metallic nanoparticles also can possess enzyme-like activity. However, most published nanozymes are metal-based nanoparticles that function via electron transport reactions.[131] Initially, the focus was on redox systems mimicking peroxidase, oxidase, catalase and superoxide dismutase enzymes, but later, hydrolase-like nanozymes were also developed.[132] The first nanozymes were metal-based nanoparticles, such as iron-,[133] noble metal-,[134] copper-[135] and cerium-based ones,[136] which possessed peroxidase, oxidase or superoxide dismutase activity. Due to their layers built up by metal ions, LDHs may represent a suitable structure for the preparation of metal-based enzyme mimicking nanostructures.

Metal ion composition of LDHs allows them to act as both ROS generator and scavenger nanoparticles. ZnMnAl,[137] MgAl doped with Ru single atom,[138] NiCo[139] and FeCo LDH[140] nanoparticles with peroxidase-like activity and CoAl LDH[97] with SOD-like activity have already been published in the literature. MgAl LDH doped with Ru single atoms showed not only peroxidase-, but also multienzymatic activity. It could efficiently remove $O_2^{\bullet-}$ and H_2O_2, and scavenge $OH^{\bullet}$, $NO^{\bullet}$ and 2,2-diphenyl-1-picrylhydrazyl (DPPH) radicals. Furthermore, it showed excellent ROS scavenging activity in the cellular environment.[138] ZnMnAl LDH functioned in the opposite way. Instead of neutralizing ROS molecules, it was able to produce them by catalyzing the Fenton reaction. By producing ROS molecules, it can

be applied in anti-cancer treatment, as the increased concentration of ROS can trigger cancer cell death.[137] For CoAl LDH, the nanosheets with the as-prepared surface defects were shown to have significantly higher SOD activity than the unmodified LDH particles. This could be due to the more active sites generated by the surface defects. In addition to the chemical test reactions, it showed remarkable ROS scavenging activity in cellular measurements, so it appeared to be applicable against oxidative damage in the mitochondria.[97]

Although some examples of enzyme-like LDH particles were detailed in the previous paragraph, there is still a lack of comprehensive investigation of LDH-based nanozymes, so there is a need to produce stable, inexpensive and effective artificial enzymes. In most applications, nanozymes and antioxidant-containing nanoparticles are used in dispersed phase. One of the most important requirement for them is their stability, therefore, the investigation of their colloidal behavior is a major aspect. Hence, the concept of colloidal stability is introduced below.

2.3. Stability of colloidal- and nanoparticle dispersions

In the second half of the 1800s, Thomas Graham defined colloidal particles in the size range of 1 nm - 1 μm.[141] Colloidal systems are present in many forms; they can contain all possible combinations of the three states of matter.[141, 142] Nanoparticles are a subgroup of colloidal particles that lie in the range of 1 – 100 nm in at least one of their dimensions.[143] Nanoparticles can be produced by fragmenting a solid particle (top-down method) or from atoms or molecules through chemical reactions (bottom-up technique). These two approaches include multiple methods such as different types of milling, chemical vapor deposition, physical vapor deposition, chemical reduction, sol-gel method and coprecipitation. The control of particle size, shape, size distribution and crystal structure are among the most important aspects that should be considered in the synthesis of nanoparticles. Improving purity and controlling aggregation are also crucial, as all of these parameters can influence the behavior of the particles and thus, their applicability.[143, 144]

The stability of colloidal dispersions is an important aspect of their application in liquid media. Aggregation of the particles leads to various unintended consequences, like phase separation, limited storage stability and shelf life. Stable colloidal dispersions are also important in biomedical applications where the formation of aggregates can have serious consequences (*e.g.,* thrombus formation and clogged veins). The most recent example

nowadays is the Nobel Prize-winning COVID19 vaccine developed by Pfizer-BioNTech. The mRNA-based vaccine was effective, safe and could be produced in large quantities, however its long-term storage posed problems. The solution to this problem was a lipid nanoparticle-based system, which resulted in a 12-week-long stability at room temperature and a 24-week-long stability at 4°C for the system. This stabilization was a major step forward in the development of the COVID19 vaccine as it significantly improved storage stability.[145]

The fundamentals of colloidal stability were described in the 1940s by two independent research groups, Derjaguin and Landau[146] in the Soviet Union and Verwey and Overbeek[147] in the Netherlands as the so-called DLVO theory, derived from the first letters of their names. This theory is based on the balance of attractive van der Waals forces and the repulsive electrical double layer (EDL) forces between charged particles immersed in electrolyte solutions. In order to explain the DLVO theory in more detail, first, EDL will be defined as follows.[141]

In aqueous media, van der Waals forces acting between identical particles are attractive. Therefore, there must be other repulsive forces present to prevent particle aggregation and destabilization. This repulsive force is derived from the EDL. The EDL was first modeled by Helmholtz with a very simple idea that the charged flat surface was compensated with oppositely charged spatial counterions. Gouy, Chapman and Debye and Hückel completed this theory. They hypothesized that the average charge distribution and the electrical potential function follow a Poisson-Boltzmann function, i.e., the potential decreases exponentially away from the particle surface. Stern further modified this model by combining the adsorbed charge compensating layer on the particle surface with the diffuse layer slightly away from the surface.[148, 149] In some cases, a more precise representation of the EDL is required, in which the Stern layer is divided into an inner and an outer Helmholtz layer, which are divided by the inner and outer Helmholtz planes (IHP and OHP, respectively). A more specific explanation is required for specifically adsorbed ions, whose adsorption is not based solely on electrostatic forces, but which have a chemical affinity to the surface.[150]

The schematic representation of the EDL is shown in Figure 7. The counter ions are located near to the oppositely charged surface, while their concentration decreases with the distance from the particle surface. The potential shows a similar tendency, reaching its maximum at the surface, while decreasing with increasing the distance (first linearly then exponentially). The potential measured in the onset of the diffuse layer is the diffuse layer potential (Ψ_D), while in the slip plane it is the so-called zeta potential (ζ). The slip plane is formed by the surrounding liquid phase, which adheres to the particles and moves with the particles during diffusion or in an electrical field.[150]

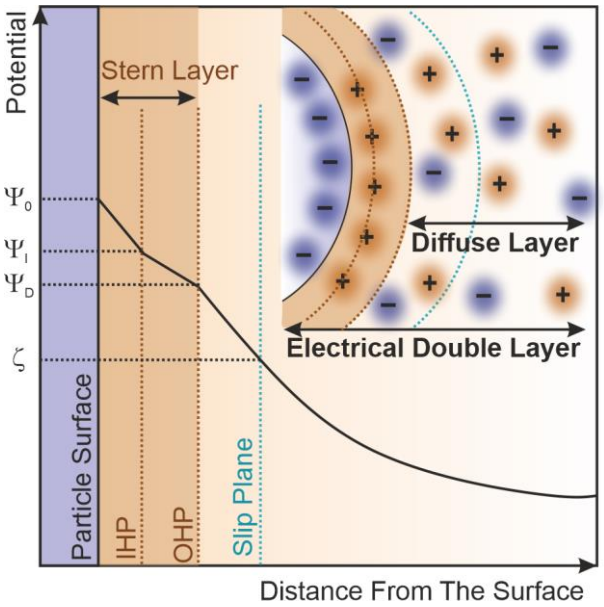

Figure 7. Schematic representation of the electrical double layer and the potential as a function of the distance to the surface. (IHP: inner Helmholtz plane, OHP: outer Helmholtz plane, Ψ_0: surface potential, Ψ_I: IHP potential, Ψ_D: diffuse layer potential, ζ: zeta potential)

The DLVO theory describes the interaction between charged particles in liquid media. Accordingly, the interaction is based on the attractive van der Waals forces and the repulsive forces resulting from the overlap of the EDL. The DLVO theory states that the total interaction energy ($V(h)$) between two particles at a distance of h above each other is the sum of the van der Waals ($V_{vdW}(h)$) and the EDL potential energy ($V_{EDL}(h)$):

$$V(h) = V_{vdW}(h) + V_{EDL}(h) \quad (1)$$

Later, the DLVO theory was completed by other, non-DLVO type forces, which also contribute to the colloidal stability of particles in a dispersion. Among the non-DLVO forces we can also classify steric, osmotic, hydration and Born forces.[151] Based on the Derjaguin approximation, the van der Waals interaction energy for two spherical particles are:[152]

$$V_{vdW}(h) = -\frac{HR}{12h} \quad (2)$$

, where H is the Hamaker constant, and R is the radius of the particles. Furthermore, the repulsive force component of Eq. (1) can be defined as:

$$V_{EDL}(h) = 2\pi R\varepsilon_0\varepsilon\kappa\psi_D^2 e^{-\kappa h} \quad (3)$$

, where ε_0 is vacuum permittivity, ε is the dielectric constant of water, ψ_D is the diffuse layer potential and κ is the inverse Debye length, which can be calculated as:

$$\kappa = \sqrt{\frac{2\,N_A e^2 I}{\varepsilon_0 \varepsilon\, k_B T}} \quad (4)$$

, where N_A is the Avogadro constant, e is the elementary charge, I is the ionic strength, k_B is the Boltzmann constant, while T is the absolute temperature.[141, 152, 153]

The interaction energy as a function of the distance between the two particles is shown in Figure 8 (A). At small distances, the van der Waals forces dominate, and the potential energy has a primary minimum. By increasing the separation distance, the potential energy function initially goes through a maximum (referred to as energy barrier), and after a certain distance the system reaches a second minimum before it finally becomes constant. The energy barrier, which derives from the superposition of the attractive van der Waals and repulsive EDL forces, has a considerable influence on the colloidal stability of particle dispersions. If the constantly moving particles come close enough to each other, they can attach and form dimers. The screening effect of the ions due to the high ionic strength reduces the repulsive forces derived from the EDL, so that the van der Waals forces dominate and the energy barrier decreases. In contrast, at a low electrolyte concentration, the particles cannot overcome the energy barrier and the system remains stable.[141, 152]

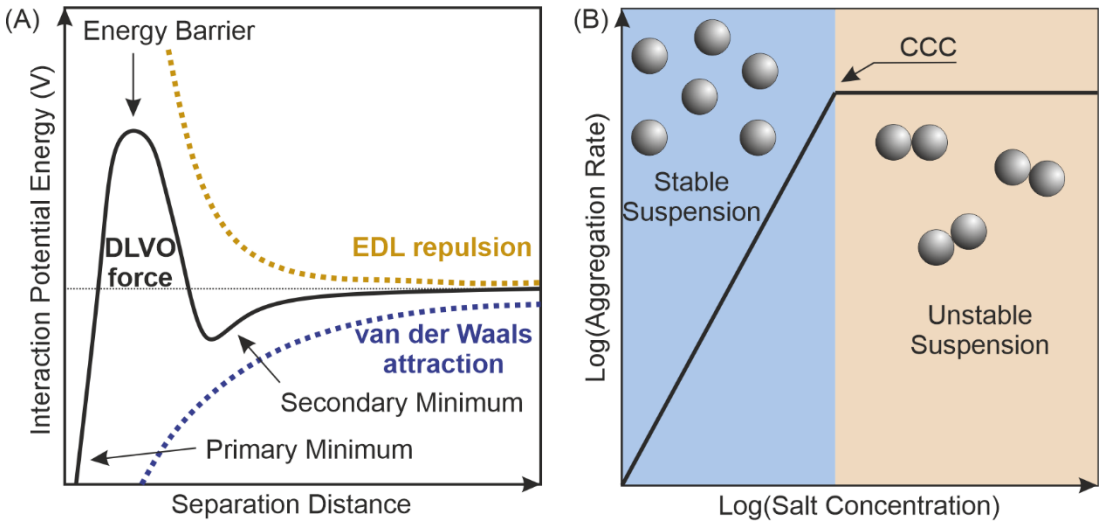

Figure 8. Schematic representation of the interaction potential energy as a function of the separation distance between the particle surfaces (A) and the change in the aggregation rate as a function of the salt concentration (B).

Aggregation rate coefficient (k) can be used to describe the aggregation process. Smoluchowski developed the relation for the diffusion controlled aggregation, which is described as follows:[142, 151]

$$k = \frac{8k_BT}{3\eta} = 1.2 \times 10^{-17}\ m^3s^{-1} \quad (5)$$

, where η is the viscosity of the solvent, while the numerical value is valid for the water medium at 25 °C.

The aggregation rate is strongly related to the ionic strength of the dispersion (Figure 8 (B)). At low electrolyte concentrations, the aggregation rate is low, or even undetectable, whereas it begins to increase with increasing salt concentrations. Above a certain salt concentration, each collision leads to aggregation and the aggregation rate becomes constant. The first, increasing and the second, constant part are denoted as slow and fast aggregation regimes and are separated by the critical coagulation concentration (CCC). The CCC is an important parameter for describing the colloidal stability, i.e. it can predict the salt-induced aggregation of a system in a certain medium.[141]

2.3.1. Tuning colloidal stability by polyelectrolyte adsorption

The colloidal stability also depends on DLVO forces, which can be induced by surface modification with surface active substances. Among them, polyelectrolytes are highly charged polymers that carry a covalently bonded cationic or anionic group and a charge-compensating counterion in their chains.[154] They adsorb on oppositely charged surfaces and form saturated and highly charged layers provided their dose is properly adjusted. In the case of highly charged surfaces and polyelectrolytes, all macromolecules adsorb on the oppositely charged surface at low polyelectrolyte doses and no polyelectrolyte remains in the liquid phase. The adsorption initially has no significant effect on the charge of the particles (Figure 9 (A)). However, by increasing the polyelectrolyte dose, it converts to zero at the isoelectric point (IEP), while at higher doses overcharging occurs and the particles become oppositely charged. At a threshold dose, the particle surface becomes completely saturated and above this concentration, the excess amount of polyelectrolytes remains in the liquid phase. The maximum amount of adsorbed polyelectrolyte is the onset of the adsorption saturation plateau (ASP).[153]

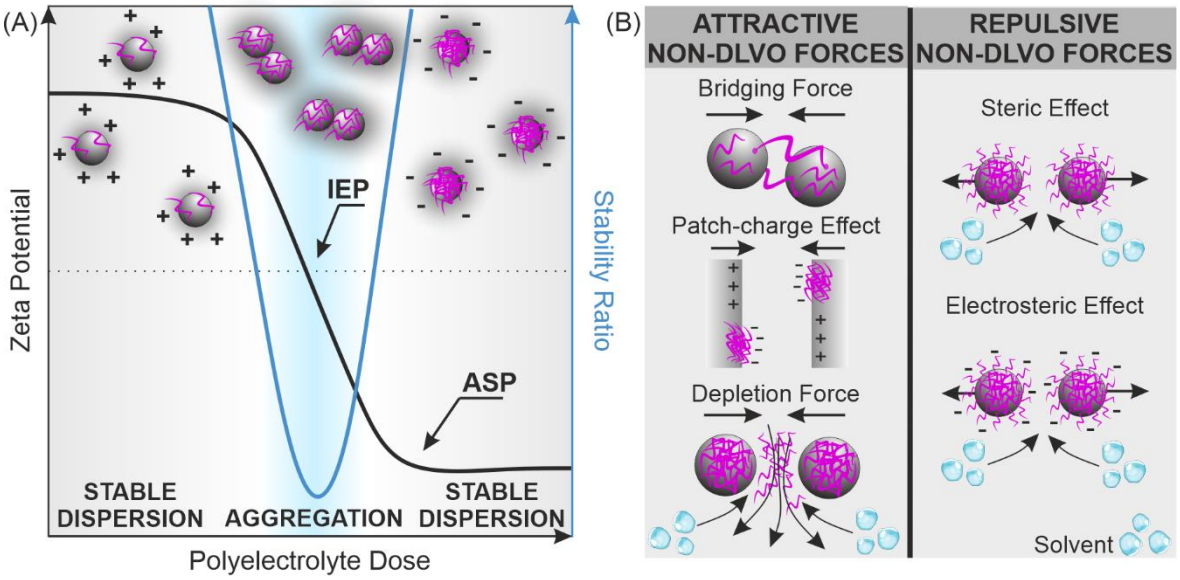

Figure 9. Schematic representation of charging and stability properties as a function of polyelectrolyte dose (A) and non-DLVO forces (B).

At low doses, where the particle charge is high, the EDL repulsion prevents aggregation, and the dispersion is stable (Figure 9 (A)). By increasing the polyelectrolyte dose, particles start to be neutralized and at the IEP the dispersion becomes unstable, aggregate formation occurs. By further increasing the polyelectrolyte dose the particle charge increases, whereby the electrostatic repulsion between the particles becomes favorable again and the stability of the dispersion increases steeply.[155]

Stable colloidal dispersions caused by polyelectrolyte adsorption are mainly due to electrostatic repulsion, but other, non-DLVO forces can also affect stability (Figure 9 (B)). In addition to electrostatic repulsion, steric repulsion can also enhance the colloidal stability of the particles, furthermore it is not affected by the high salt concentration. The swollen polyelectrolyte layer contains tails and loops on the particle surface, whose overlap causes an osmotic pressure, thus an additional repulsion, which further prevents the formation of aggregates. The joint effect of EDL and steric repulsion is denoted as electrosteric stabilization.[153, 156, 157] In the case of unsaturated polyelectrolyte layers, an attractive non-DLVO force can occur, known as the patch-charge force.[153, 158] Accordingly, polyelectrolytes can adsorb on the particle surface and form oppositely charged islands. These islands are attracted by the non-covered bare surface charge of another particle leading to an electrostatic attraction, which is not involved in the DLVO force profile. Similar to the patch-charge effect, the bridging force can also lead to the destabilization of a colloidal dispersion. Namely, when a polymer chain attaches to a particle, the end of the chain can also adsorb to another nearby particle and form a bridge between them, leading to the

formation of aggregates.[155] The third important destabilization phenomenon that can occur due to polyelectrolytes is the depletion force. Unlike the previously mentioned non-DLVO forces, the depletion force arises if polyelectrolyte concentration is high and significant amount of polyelectrolytes remain dissolved in the solution phase. In this case, the difference in osmotic pressure within the interparticle space and in the bulk solution can lead to aggregation, and thus destabilization of the dispersion.[153]

2.3.2. Colloidal stability of LDH particles

In several studies, the stabilization ability of polyelectrolytes on different types of colloidal particles were investigated. In most cases, the polyelectrolyte adsorption gave rise to an oppositely charged particle surface, which increased the colloidal stability due to electrostatic or steric interactions. The colloidal stability of LDH particles were enhanced by functionalization with heparin,[159] poly(ethylene imine),[156] poly(acrylamide-*co*-diallyl dimethyl ammonium chloride),[156] protamine sulfate.[156] Of the previously mentioned molecules, heparin (a well-known anticoagulant) is a promising polyelectrolyte for stabilizing LDHs and can improve the biomedical application of the particles. By choosing the appropriate amount of heparin, overcharging occurred and the LDHs were completely covered by the polyelectrolyte. The experimentally determined surface charge densities were twice as high for the coated particles as for the bare ones, resulting in 20 times higher CCC values for the functionalized LDHs. In addition to the repulsive electrostatic forces, the steric repulsion between the swollen polyelectrolyte chains is also become significant. Therefore, polyelectrolyte coating, such as heparin, can cause significantly higher dispersion stability, promising a potential carrier for biomedical applications.[159]

It was also shown that colloidal stability can be improved by the adsorption of polyelectrolyte-bilayer coating. The aggregation properties of the poly(styrene sulfonate) coated LDH particles followed the DLVO theory, and the CCC values increased steeply compared to the bare particles. However, after adsorption of the second polyelectrolyte ((poly(dyallil dimethyl ammonium chloride)) layer, the colloidal behavior of the system was atypical. The formation of the polyelectrolyte bilayer resulted in steric rather than electrostatic stabilization, which possessed higher stability for the system. This overall can even lead to a such stable system that the high ionic strength was unable to destabilize.[160]

Several studies are focusing on the stabilization of LDHs with other suitable materials, like proteins[161, 162] or polysaccharides.[163] Serum albumin is one of the most

important protein found in blood plasma of mammals. Bovine serum albumin (BSA), the animal variant of serum albumin, was successfully immobilized on the LDH surface, possessing higher colloidal stability for the nanoparticles. The BSA-coated LDH nanoparticles remained stable in electrolyte solution, furthermore, the coating also enhanced the cellular uptake efficiency.[161] Another study showed, that the protein corona formed by albumin not only protects the particles from aggregation, but also prevents their dissolution at acidic pH, and thus offers the possibility of prolonged circulation in physiological fluids.[162] Alginate, a negatively charged natural polysaccharide found in brown algae, can form strong interactions with the positively charged LDH nanosheet surfaces. Through the functionalization, the exfoliated LDHs were effectively stabilized, the formation of the original stacked structure was hindered by the saturated polysaccharide layers.[163]

3. Objectives

The main goal of the doctoral research was to produce LDH-based nanomaterials to combat ROS. Colloidal and structural features of dLDH and LDH particles were systematically designed and studied, while surface functionalization and structural modification were applied to endow the nanomaterials with antioxidant activity, which was assessed in both chemical test reactions and intracellular assays. The sub-objectives can be summarized as follows.

First, the restacking and aggregation mechanisms of delaminated LDH nanosheets were aimed to study in the presence of monovalent salt. The main question was to determine experimental condition, at which the lamellar structure forms of delaminates.

Second, immobilization of antioxidant enzymes (HRP, SOD, CAT) on the delaminated nanosheet surfaces were aimed to be performed by the sequential adsorption method. The enzymes were separated by Alg and trimethyl chitosan (TMC) polyelectrolyte layers to enhance enzyme adsorption on the particle surface, and tune the particle charge.

Third, molecular antioxidants were subjected to immobilization in/on LDH particles, to develop antioxidant composites with advantageous colloidal, structural and scavenging properties.

Fourth, LDH particles with enzyme-like characteristics, *i.e.,* LDH nanozymes, were prepared by tuning their metal ion composition. The main question was whether or not such a single phase LDH nanozyme is able to exhibit multiple enzyme mimetic features.

In summary, the detailed characterization of the colloidal behavior of dLDH nanosheets can enhance their possible application in water remediation processes. However, the immobilization of molecular and enzymatic antioxidants and the structural modification of LDH nanoparticles propose their use in biomedical or industrial processes, where ROS elimination is an important aspect.

4. Experimental Part

4.1. Materials

The following reagents were purchased in analytical grade and were not further purified before application. The solutions were prepared in ultrapure water produced with a Puranity TU 3 UV/UF+ (VWR) device. To remove insoluble impurities, the water and salt solutions were filtered using a Millex syringe filter of 0.1 μm pore size. The experiments were carried out at 25 °C.

Table 1. Reagents used in the experiments with formula and manufacturer.

Name/Abbreviation	Formula	Manufacturer
Magnesium nitrate hexahydrate	$Mg(NO_3)_2 \times 6\ H_2O$	VWR International
Aluminium nitrate nonahydrate	$Al(NO_3)_3 \times 9\ H_2O$	VWR International
Ammonium solution (ca. 25 %)	NH_3	VWR International
Sodium hydroxide solution (4 M)	NaOH	VWR International
Tannic acid (TA)	$C_{76}H_{52}O_{46}$	VWR International
Glutathione (GSH)	$C_{10}H_{17}N_3O_6S$	VWR International
Magnesium chloride hexahydrate	$MgCl_2$ x 6 H_2O	VWR International
Copper chloride dihydrate	$CuCl_2$ x 2 H_2O	VWR International
Aluminium chloride hexahydrate	$AlCl_3$ x 6 H_2O	VWR International
Sodium hydroxide pellets	NaOH	VWR International
Sodium chloride	NaCl	VWR International
Sodium alginate (Alg)	$(C_6H_8O_6)_n$	VWR International
Trimethyl chitosan (TMC)	$(C_9H_{18}ClNO_4)_n$	University of Queensland (I. Toth's research group)
Superoxide dismutase from bovine liver (SOD)	–	Sigma Aldrich
Horseradish peroxidase (HRP)	–	VWR International
Catalase from bovine liver (CAT)	–	Sigma Aldrich
2,2-diphenyl-1-picrylhydrazyl (DPPH)	$C_{18}H_{12}N_5O_6$	VWR International
Methanol	CH_3OH	VWR International
Nitro blue tetrazolium (NBT)	$C_{40}H_{30}Cl_2N_{10}O_6$	VWR International
Xanthine	$C_5H_4N_4O_2$	VWR International
Xanthine oxidase	–	Sigma Aldrich
Disodium hydrogen phosphate anhydrous	Na_2HPO_4	VWR International
Sodium dihydrogen phosphate	NaH_2PO_4	VWR International
Hydrogen peroxide (30 wt%)	H_2O_2	VWR International
Guaiacol	$C_7H_8O_2$	VWR International
Ammonium molybdate (para) tetrahydrate	$(NH_4)_6Mo_7O_{24} \times 4\ H_2O$	VWR International
2'7'-dichlorodihydrofluorescein diacetate (H2DCFDA)	$C_{24}H_{16}Cl_2O_7$	Sigma Aldrich
Triton-X-100	$C_{14}H_{22}O(C_2H_4O)_n$	Sigma Aldrich

Anti-HRP monoclonal antibody	–	Sigma Aldrich
Glucose oxidase	–	Sigma Aldrich
Glucose	$C_6H_{12}O_6$	Sigma Aldrich
Cysteamine hydrochloride	$HSCH_2CH_2NH_2$	Sigma Aldrich
Dulbecco's modified eagle medium (DMEM)	–	Gibco
10% fetal bovine serum (FBS)	–	Gibco
Kanamycin sulfate	$C_{18}H_{38}N_4O_{15}S$	Gibco
Antibiotic-antimycotic solution	–	Gibco
GlutaMaxTM supplement	–	Gibco
Dulbecco's phosphate buffer saline (PBS)	–	Gibco
Alexa Fluor 488 Goat anti-Rabbit secondary antibody	–	Thermo Scientific
Goat anti-Rabbit Alexa Fluor 568 secondary antibody	–	Thermo Scientific
Donkey anti-Mouse Alexa Fluor 647 secondary antibody	–	Thermo Scientific
4',6-diamidino-2-phenylindole (DAPI)	$C_{16}H_{15}N_5$	Invitrogen
Anti-CAT	–	Invitrogen
Anti-SOD	–	Invitrogen
Filter set for 2',7'-bis-(2-carboxyethyl)-5-(and-6)-carboxyfluorescein acetoxymethyl ester (BCECF-AM)	–	Biotium
4% Paraformaldehyde	$OH(CH_2O)_nH$	Alfa Aeser
10 % bovine serum albumin in PBS (BSA-PBS)	–	Pan-Biotech
Primary antibody against γH2AX histone	–	Cell Signalling Technology
Human cervical adenocarcinoma (HeLa) cells	–	ATCC

4.2. Synthesis methods

4.2.1. Preparation of delaminated layered double hydroxide particles

The synthesis of dLDH dispersion was based on the protocol of Zhang et. al.[69] A mixed metal salt solution, containing 0.225 mol/L $Mg(NO_3)_2 \times 6\ H_2O$ and 0.075 mol/L $Al(NO_3)_3 \bullet 9\ H_2O$, was added dropwise to a beaker simultaneously with 7 wt% NH_3 solution under vigorous stirring and N_2 atmosphere. Thereafter, the obtained slurry was stirred for 5 min followed by ultrasonication of 30 min and centrifugation of 10 min at 4200 rpm. The sample was washed three times with deionized water, thereafter a final centrifugation step was performed with the former mentioned settings to remove trace amounts of aggregates. The following experiments based on dLDH particles were performed with the resulting supernatant.

4.2.2. Preparation of layered double hydroxide particles

Mg_2Al LDH particles were synthesized by a coprecipitation method. A mixed salt solution with a total salt concentration of 0.3 mol/L (0.2 mol/L $Mg(NO_3)_2 \times 6\ H_2O$ and 0.1 mol/L $Al(NO_3)_3 \times 9\ H_2O$) was stirred vigorously under N_2 atmosphere. The pH of was set to 10 by adding the proper amount of 4 mol/L NaOH solution. After a stirring of 30 min, the solution was centrifuged and redispersed. The LDH dispersion was transferred to an autoclave for 24 h at 120 °C. The final product was centrifuged, washed three times with deionized water and dried in an oven at 50 °C overnight. For the further use, the LDH powder was dispersed in ultrapure water.

4.2.3. Preparation of tannic acid (TA) and GSH containing LDH particles

Two independent methods (adsorption and coprecipitation) were used to immobilize TA and GSH in/on Mg_2Al LDH particles. The structure of TA and GSH is shown in Figure 10. First, the adsorption method was carried out in 10 mL of 0.1 mol/L tannic acid solution. 0.5 g LDH powder was redispersed in the antioxidant solution and was stirred at room temperature under N_2 atmosphere overnight. The sample was then centrifuged at 4200 rpm for 10 min, washed three times with deionized water and the slurry was dried in an oven at 50 °C overnight. The final composite was denoted as LDH/TA/a. The same procedure was applied for the GSH-containing sample, which is denoted as LDH/GSH/a in the following.

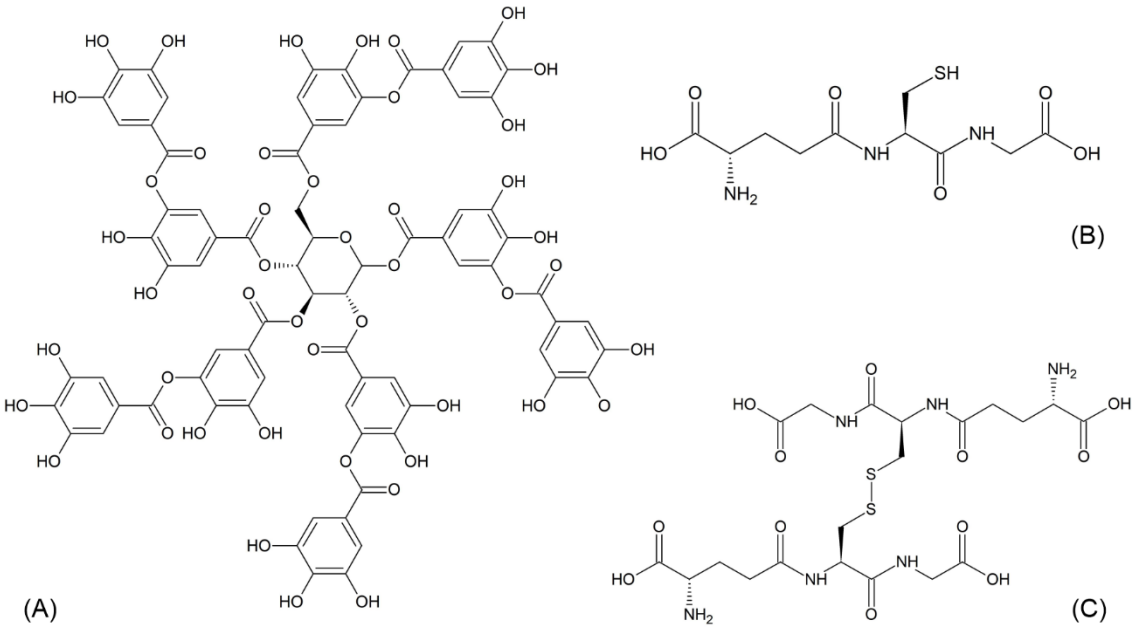

Figure 10. Structure of TA (A), GSH (B) and disulfide form of GSH (GSSG) (C)[164]

The coprecipitation method was similar to that described above. 0.01 mol/L $Mg(NO_3)_2$ • 6 H_2O, 0.005 mol/L $Al(NO_3)_3$ • 9 H_2O and 0.005 mol/L GSH were dissolved in 50 mL ultrapure water. The vigorously stirred, appropriate amount of 4 mol/L NaOH solution was added to the solution under a N_2 atmosphere to adjust the pH to 10. After a 24-hour-long stirring, the sample was centrifuged (4200 rpm, 10 minutes) and washed three times with deionized water. The slurry was collected and dried in an oven at 50 °C overnight. The as-prepared sample was denoted as LDH/GSH/c. The same procedure was used for the TA-containing sample, however, the TA concentration in the salt solution was 0.0005 mol/L. The TA-containing sample was denoted as LDH/TA/c.

To compare the antioxidant structures before and after synthesis, the antioxidant solutions were treated with NaOH. 0.005 mol GSH and 0.0005 mol TA were dissolved in distilled water of 50 mL. The pH of the solutions was set to 10 with 4 mol/L NaOH/1 mol/L HCl solutions, then the solutions were dried in an oven at 60 °C overnight.

4.2.4. Preparation of copper containing LDH nanoparticles

$Cu_xMg_{3-x}Al$ LDH nanoparticles were synthesized by a modified coprecipitation method. A solution with an initial metal salt concentration of 0.8 mol/L (total 0.6 mol/L of $MgCl_2$ x 6 H_2O and $CuCl_2$ x 2 H_2O, 0.2 mol/L $AlCl_3$ x 6 H_2O) was prepared in 5 mL of distilled water. The ratio of divalent to trivalent metal ions was set to 3:1, while the initial ratio of Mg : Cu was systematically varied (x = 0.2, 0.4, 0.6). The mixed salt solution was added to 20 mL of 0.4 mol/L NaOH solution with vigorous stirring. After a 40-min-long stirring, the solution was centrifuged (4200 rpm, 10 minutes), washed three times with distilled water. The slurry was redispersed in 20 mL distilled water, transferred to an autoclave and treated at an autogenic pressure at 100 °C overnight. The resulting dispersion was centrifuged (4200 rpm, 15 minutes) and the supernatant was used in the following. The copper-containing samples were denoted as CMA1, CMA2 and CMA3, in which the numbers represent the increasing copper content.

For control measurements, Mg_3Al LDH was also prepared using a similar procedure. In this case, a salt solution containing 0.6 mol/L $MgCl_2$ x 6 H_2O and 0.2 mol/L $AlCl_3$ x 6 H_2O was added to 20 mL of 0.4 mol/L NaOH solution. After 40 min stirring, the solution was centrifuged (4200 rpm, 10 minutes) and washed three times. The slurry was redispersed in 20 mL distilled water and used for the following experiments.

4.3. Light scattering methods

Electrophoretic light scattering (ELS) and dynamic light scattering (DLS) measurements were performed with a Litesizer 500 (Anton Paar) instrument, equipped with a 40 mW laser source operating at 658 nm wavelength. All measurements were taken in back scattering mode at a scattering angle of 175°. For the ELS measurements, Ω-shaped plastic cuvettes of 400 µL total volume were used, while for DLS measurements, polystyrene plastic cuvettes of 2 mL total volume were used.

4.3.1. Surface charge and aggregation assessment in salt solutions

For the salt-induced ELS measurements, appropriate amounts of ultrapure water, NaCl and particle dispersion were used. The particle concentration was set to 10 ppm for all systems, while the NaCl concentration was systematically varied. The final volume of the mixtures was 2 mL and the pH was 7. After the samples were equilibrated for an appropriate time, the zeta potentials (ζ) were calculated from the measured values of electrophoretic mobility (µ) using the Smoluchowski's equation:[150]

$$\mu = \frac{\varepsilon \times \varepsilon_0 \times \zeta}{\eta} \tag{6}$$

, where ε is the relative permittivity of water, ε_0 is the permittivity of vacuum, and η is the dynamic viscosity of the solvent.

To determine surface charge densities (σ) zeta potentials were plotted against NaCl concentration and the points were fitted with Gouy-Chapman equation:[142]

$$\sigma = \frac{2 \times k_B \times T \times \varepsilon \times \varepsilon_0 \times \kappa}{e} \times \sinh\frac{e \times \zeta}{2 \times k_B \times T} \tag{7}$$

, where k_B is the Boltzmann constant, T is the absolute temperature, κ is the inverse Debye length and e is the elemental charge.

Sample preparation for the DLS measurements was similar to the ELS procedure, except that monitoring of the hydrodynamic radius (R_h) in time started right after the mixing of reaction component. The particle size was determined using the cumulant fit applied to the intensity correlation function, then R_h values were calculated based on Einstein-Stokes equation from the translation diffusion coefficient (D):[165]

$$R_h = \frac{k_B \times T}{6 \times \pi \times \eta \times D} \tag{8}$$

Colloidal stability was estimated based on the stability ratio versus NaCl concentration diagrams. Stability ratio was calculated based on the following equation:[159]

$$W = \frac{k_{fast}}{k} \tag{9}$$

, where k is the apparent aggregation rate determined by fitting the change of R_h in time caused by particle aggregation,[166] while k_{fast} is the fast aggregation regime, measured at 1 mol/L NaCl concentration, at which repulsive double layer forces are screened, and diffusion-controlled aggregation occurred. Note that stability ratio close to one means, that the dispersion is unstable, all particle collision result formation of dimers.

Critical coagulation concentrations (CCCs), which terminates the slow and fast aggregation regime, were calculated from the stability ratio versus NaCl concentration diagrams with the following equation:

$$W = 1 + \left(\frac{CCC}{c_s}\right)^{-\beta} \tag{10}$$

, where c_s is the NaCl concentration, and β is the slope of the stability ratio in the slow aggregation regime.

4.3.2. Polyelectrolyte and enzyme immobilization by sequential adsorption method

To produce enzymatically active nanocomposites, dLDH nanosheets were functionalized with three antioxidant enzymes (SOD, HRP and CAT). The enzymes were separated with two polyelectrolyte layers, Alg and TMC. The appropriate amount of polyelectrolytes and enzymes were simply mixed with the calculated amount of dLDH dispersion and equilibrated at room temperature overnight to obtain the saturated layers. The polyelectrolyte and enzyme doses were chosen based on the ELS measurements, keeping the particle concentration at 10 mg/L, adjusting the pH to 7, and using 1 mM NaCl as background electrolyte. The polyelectrolytes and enzymes were immobilized in the following order (the dose applied during immobilization is indicated in the brackets): dLDH – Alg (300 mg/g) – HRP (10 mg/g) – TMC (400 mg/g) – SOD (10 mg/g) – CAT (10 mg/g). Note that mg/g means the adsorbed mg polyelectrolyte/enzyme on 1 g dLDH particle. The final composite was denoted as dLDHaHtSC. ELS and DLS measurements with the composite were performed as described earlier.

4.4. Turbidity measurements

Turbidity measurements were also performed to assess the colloidal stability of the dLDH dispersion. The measurements were carried out with a UV-3100PC spectrophotometer (VWR) at 340 nm wavelength. Similar to DLS measurements, calculated amounts of water, dLDH dispersion and NaCl were mixed to adjust the reaction mixture. The final dLDH concentration was set to 2000 mg/L for the critical coagulation time (CCT) studies, while 50 mg/L for the stability ratio measurements. The samples were constantly stirred during the measurements. Stability ratios were calculated likewise to DLS measurements; however, first, relative turbidity was estimated:

$$\tau_r = \frac{\tau}{\tau_0} \tag{11}$$

, where τ is the turbidity of the reaction mixture, while τ_0 is the turbidity of dLDH dispersion.

Calculating relative turbidity values, stability ratios can be described with the following equation:

$$W = \frac{\tau_{r\_fast}}{\tau_r} \tag{12}$$

, where *fast* refers to the fast aggregation as it described earlier for DLS measurements.

4.5. Antioxidant tests

4.5.1. DPPH assay

The radical scavenging activity of LDH/Ta/a, LDH/TA/c, LDH/GSH/a and LDH/GSH/c as well as native TA and GSH was revealed by the DPPH assay.[167] The test is based on the color change occurred by the reduction of the DPPH radical to DPPH-H (Figure 11).

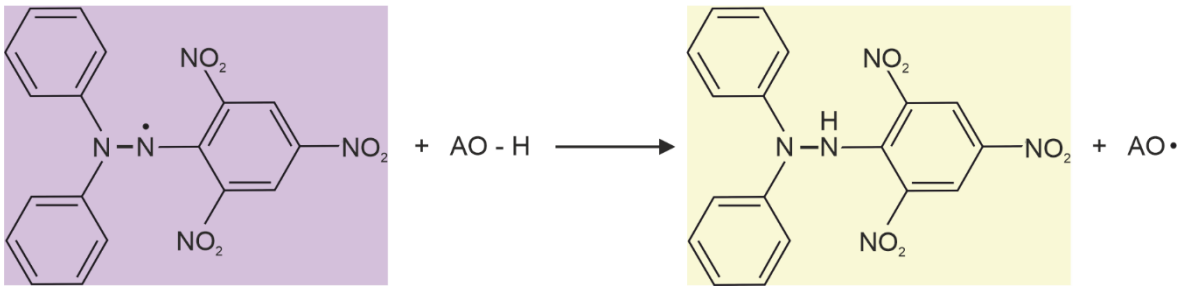

Figure 11. Schematic representation of the reaction between the DPPH radical and the antioxidants. The colors represent the color change during the reaction.

During the test, 3.5 mL of 20 mg/L DPPH solution was completed to 3.6 mL with the test samples. The color change is also visible to the naked eye, the initially purple solution turns yellow after an appropriate time. The concentration of the samples was systematically varied, while the absorbance was measured at λ = 517 nm, the absorption maximum of DPPH. After the DPPH solution was mixed with the antioxidants, the reaction mixture was allowed to stand until the absorbance reached a constant value when the reaction was considered to be completed. The absorbance was monitored by a Genesys 10S UV-Vis spectrophotometer. Based on the change in absorbance values, the remaining percentage of DPPH (DPPH (%)) could be calculated:

$$\text{DPPH (\%)} = \frac{A}{A_0} \tag{13}$$

, where A_0 is the initial absorbance of DPPH without antioxidant in the solution, and A is the absorbance value after the reaction is completed.

For LDH containing samples the following, corrected equation was used:

$$\text{DPPH (\%)} = \frac{A - A_{sample}}{A_0} \tag{14}$$

, where A_{sample} is absorbance value measured for the LDH dispersion without the addition of DPPH solution to detect any light scattering effect.

By plotting DPPH (%) as a function of the antioxidant concentration, the efficient concentration (EC_{50}) values could be determined. EC_{50} is the antioxidant concentration, responsible for the decomposition of half of the radicals present in the reaction mixture. The standard deviation determined based on three independent measurements was within 5 %.

The recyclability test was only measured with the LDH/TA/a sample. For these measurements the total volume of the reaction mixture was 15 mL, including 4.2 mg LDH/TA/a, and the DPPH concentration was adjusted to 23.3 mg/L (as in the original protocol). To estimate the reusability of the sample, after the appropriate reaction time, 1.5 mL reaction mixture was removed from the solution, and the absorbance was measured. Then the concentration of the reaction mixture was set back to 23.3 mg/L, by completing the reaction mixture to 15 mL. These steps were repeated until the activity of the sample decreased significantly. The calculation was performed in a similar way as described above, but here the reduced DPPH (%) was plotted against the recycling number. For a better understanding, reduced DPPH (%) means the amount of DPPH that reacted with the antioxidant:

$$\text{Reduced DPPH (\%)} = 100\ \% - \text{DPPH (\%)} \quad (15)$$

4.5.2. SOD assay

Fridovich assay[168] to estimate the SOD activity of the samples was measured on dLDHaHtSC and on CMA1-3 samples. The assay is based on the reaction of xanthine and xanthine oxidase. The reaction of xanthine with xanthine oxidase produces superoxide radicals that can be readily detected with the aid of the dye nitro blue tetrazolium (NBT). The schematic representation of the reaction is shown in Figure 12.

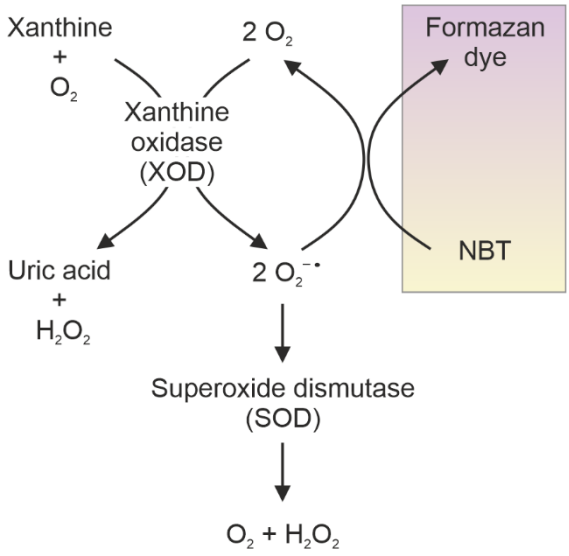

Figure 12. Schematic representation of the reaction mechanism in the SOD assay. The colors represent the color change due to the oxidation of NBT.

The final reaction mixture consisted of 100 µL xanthine (3 mM), 150 µL xanthine oxidase (3 g/L), 50 µL NBT (3 mM) in phosphate buffer (10 mM). This mixture was completed to total volume of 1.5 mL with SOD, dLDHaHtSC and CMA1-3 samples. The concentration of the active ingredient was systematically varied in the reaction mixture. After mixing the reaction components, the absorbance was monitored at 565 nm wavelength for 6 minutes using a Genesys 10S UV-Vis spectrophotometer. The inhibition of the superoxide radical anion was calculated with the following equation:

$$I = \frac{\Delta A_s - \Delta A_0}{\Delta A_0} \quad (16)$$

, where ΔA_s is the change in absorbance measured with the sample, and ΔA_0 is the change in absorbance value without any enzymatically active ingredient.

Fitting the inhibition values plotted against the enzyme concentration, inhibitory concentration (IC_{50}) values can be determined. IC_{50} value is the enzyme concentration responsible for the decomposition of 50 % of the superoxide radicals in the reaction mixture.

4.5.3. HRP assay

The guaiacol assay[169] was performed to detect the HRP-like activity of the dLDHaHtSC samples. During the reaction mechanism, HRP reacts with the H_2O_2 in the reaction mixture. Due to the decomposition of H_2O_2 to molecular oxygen and water, oxygen can oxidize guaiacol to tetra-guaiacol, while the color of the solution changes to brownish. The schematic representation of the reaction mechanism is shown on Figure 13.

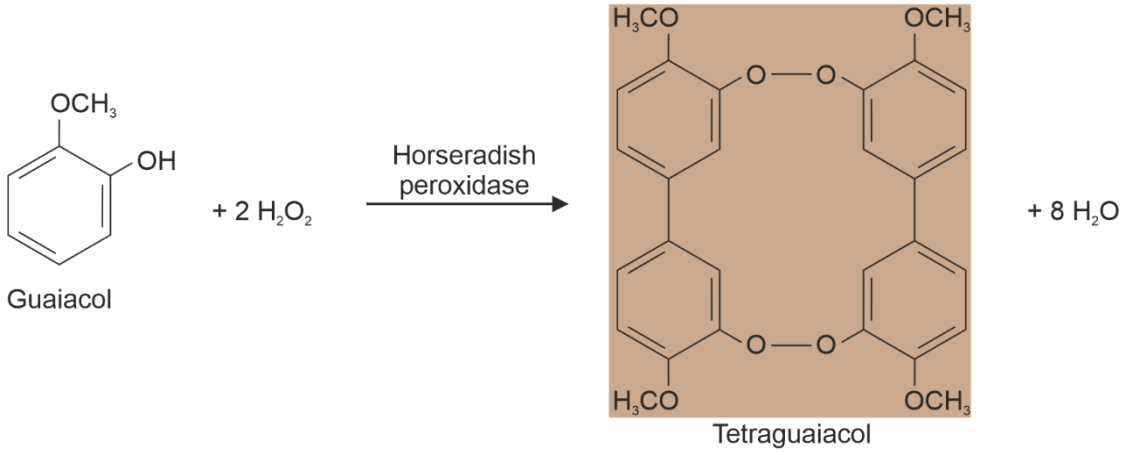

Figure 13. Schematic representation of the reaction mechanism in the guaiacol assay.

125 µL phosphate buffer (100 mM), 125 µL enzyme or composite (enzyme concentration was kept at 1 mg/L), 350 µL H_2O_2 (9 mM) was completed to total volume of 1.2 mL with guaiacol substrate at various concentrations. The absorbance was monitored at 470 nm for 6 minutes with a Genesys 10S spectrophotometer. The reaction rates (v) (calculated from the absorbance vs reaction time diagrams) were plotted as a function of substrate concentration (S) and the Michaelis-Menten function was used to fit the data:[170]

$$v = \frac{v_{max} S}{K_M + S} \tag{17}$$

, where v_{max} is the maximum reaction rate, and K_M is the Michaelis constant.

4.5.4. CAT assay

A simple spectrophotometric assay based on the reaction between H_2O_2 and ammonium molybdate was performed to estimate the catalase activity.[171] The reaction of H_2O_2 and ammonium molybdate forms a yellow-colored complex with an absorption maximum at 350 nm. The reaction mixture contained 3 mM H_2O_2, while the enzyme and dLDHaHtSc or CMA1-3 concentration was altered. After 3 minutes, the reaction between the enzymes/nanozymes was stopped by adding the required amount of ammonium molybdate solution. The ammonium molybdate concentration was set to 25.4 mM in the reaction mixture. The remaining H_2O_2 (%) can be calculated based on the difference of the absorbance values between the initial and the final states. The EC_{50} values were calculated based on the fitted H_2O_2 (%) values plotted against the enzyme/nanozyme concentration.

4.6. Measurement techniques

4.6.1. Structural characterization

A Bruker D8 Advanced diffractometer with CuKα (λ = 0.1542 nm) as a radiation source was used for recording the XRD patterns of the dLDH and CMA particles. The measurement was operated at ambient temperature in a 2θ = 5 – 80°range applying a step size of 0.02°.

For LDH, LDH/TA/a, LDH/TA/c, LDH/GSH/a and LDH/GSH/c a Rigaku XRD-Miniflex II instrument operating also with CuKα (λ = 0.1542 nm) wavelength and 40 kW accelerating voltage at 30 mA. The diffractograms were recorded in a 2θ = 3 – 80°range applying 2°/min scan speed. XRD patterns were identified by JCPDS database.

Bragg's law[172] was applied to calculate the basal distance (d):

$$n \times \lambda = 2 \times d \times \sin\theta \tag{18}$$

, where n is the diffraction order and θ is the angle of incidence.

The c crystal parameter for CMA samples with hexagonal crystal structure was calculated with the following equation:

$$\frac{1}{d_{hkl}^2} = \left[\frac{4}{3} \times (h^2 + k^2 + h \times k) + l^2 \times \left(\frac{a}{c}\right)^2\right] \times \frac{1}{a^2} \tag{19}$$

, where *a* and *c* are the crystal parameters, while *h,k* and *l* defines the orientation of the distinguished plane.

Small angle X-ray scattering (SAXS) measurements were carried out for dLDH and for the subsystems of the dLDHaHtSC samples at the EMBL BioSAXS synchrotron beamline P12.[173] The samples were measured at five different particle concentrations, namely 0.2 mg/mL, 0.4 mg/mL, 0.8 mg/mL, 1.0 mg/mL and 1.2 mg/mL. The scattering curve of the powder LDH sample was recorded with a bench-top SAXS device, operated with a position-sensitive detector (PSD 50M, M. Braun AG) containing 1024 channels of 55 μm in width. The CuKα radiation (λ = 0.15406 nm) was generated by a Philips PW1830 X-ray generator operating at 40 kV and 30 mA. The scattering vector (h) was defined as:[174, 175]

$$h = 4 \times \pi \times \sin\theta \times \lambda^{-1} \quad (20)$$

, where θ is the half of the scattering angle.
To analyze the results, the equation of Porod law was applied:

$$I(h) = I_0 \times h^{-S} \quad (21)$$

, where *I* is the scattered intensity and *S* is the slope, which describes the shape of the scattering curve at certain angles.

The infrared spectra for LDH, LDH/TA/a, LDH/TA/c, LDH/GSH/a and LDH/GSH/c were recorded using a Nicolett™ Summit FT-IR spectrophotometer (Nicolet Instrument Company) in attenuated total reflectance (ATR) detection mode. The instrument is equipped with a ZnSe-based ATR accessory. The spectra were recorded in the 4000 – 400 cm^{-1} range with a resolution of 4 cm^{-1} collecting and averaging 16 total scans. The IR spectra of the samples were taken after reaction with the DPPH radical were measured under the same conditions, after centrifugation and drying. The same settings were also used for the samples treated with NaOH.

The Raman spectra were recorded with a Bruker Senterra II Raman microscope. For LDH/TA/a and LDH/TA/c, the spectra were taken with a light source operated at 532 nm wavelength and 12.5 mW laser power, while for LDH/GSH/a and LDH/GSH/c, the wavelength was set to 785 nm and the laser power was 100 mW. The final data were obtained by averaging 32 spectra at an exposition time of 4 s. The Raman spectra for the samples collected after the reaction with the DPPH radical were measured under the same conditions

after the centrifugation and drying step. The same settings were used for NaOH treated samples as well.

The CMA1-3 samples were measured with the same instrument, by using 532 nm wavelength and 12.5 mW laser power. To obtain the final data, 16 spectra were averaged with an exposition time of 10 s.

UV-Vis and NIR spectra were measured for GSH and TA containing samples with a SHIMADZU UV-3600i Plus UV-vis-NIR spectrophotometer. The instrument is equipped with PMT, InGaAs and PbS detectors. The spectra were collected in the 50000 – 6000 cm^{-1} range with 4 cm^{-1} resolution.

X-ray photoelectron spectroscopy (XPS) measurements for CMA1-3 samples were performed on a SPECS instrument equipped with a PHOIBOS 150 MCD 9 hemispherical analyzer. The electron energy analyzer was operated in fixed analyzer transmission (FAT) mode with 40 eV pass energy for acquiring survey scans and 20 eV for high resolution scans. The excitation source was an Al Kα (hν = 1486.6 eV) radiation operated at 150 W power. The sample charging was compensated with an electron flood-gun (adventitious carbon 1s peak was monitored and set at 284.8 eV). Spectrum evaluation was carried on with a CasaXPS commercial software package.[176]

The specific surface area of the dLDH samples was calculated from measurements with a NOVA3000 (Quantachrome, USA) gas adsorption system using N_2 adsorbate. The gel-phase samples (to avoid unwanted aggregation) were outgassed under vacuum for 16 h at 25°C before the measurements. The surface areas were calculated using the Brunauer-Emett-Teller method in the relative pressure range of 0.05 – 0.65.

4.6.2. Morphological characterization

Atomic force microscopy (AFM) images were taken to characterize the dLDH particles before, during and after restacking. The images were recorded by a Multimode Nanoscope Illa AFM instrument. The device was operated in tapping mode at ambient temperature in air using Si tip cantilever (Veeco Nanoprobe Tips RTESPA model). To deposit the dispersions, a freshly cleaved mica substrate was used (Ted Pella, Highest Grade VI).

Transmission electron microscopy (TEM) images were collected with a FEI Tecnai™ G^2 20X Twin type electron microscope. A copper-carbon mesh grid was used as a substrate

for the particle dispersions and 200 kV accelerating voltage was used for the imaging in the bright field mode.

Scanning electron microscope (SEM) images for TA and GSH containing samples were recorded by a Hitachi S-4700 SEM device operating with 10 kV accelerating voltage. The samples were immobilized on a silicon wafer, and a thin gold layer was deposited on the surface to improve the conductivity of the surface.

4.6.3. Fluorescence lifetime measurements

Time-correlated single photon counting (TCSPC) based fluorescent lifetime microscopy (FLIM) measurements were performed for MA and CMA1-3 samples to confirm copper incorporation. The instrument is equipped with a PicoQuant upgrade kit installed into a (LSM) Nikon C2+ laser scanning confocal unit. The excitation wavelength of the picosecond laser diode was 560 nm with a repetition of 20 MHz. The sample was scanned with a high numerical aperture objective (Nikon CFI Plan Apo Lambda 60x Oil, NA:1.4), and the emitted fluorescence light was spectrally filtered with bandpass filter (ET600/50m, Chroma). The instrument is equipped with a PMA Hybrid 40 detector unit having <120 ps response time and >40% detection efficiency. The dimension of the scanned area was 30 × 30 μm^2 (256 × 256 pixels), and >10^5 photons were collected for precise lifetime calculations. The dispersions were mounted on a cavity microscope slide and covered with a standard (170 μm thick) microscope coverslip. The data were collected >5 μm above the coverslip, where the sample was homogeneous. For all post processing evaluation SymPhoTime 64 software (PicoQuant) was used.

4.6.4. Thermogravimeter coupled mass spectrometry measurements

The antioxidant content in TA and GSH containing samples were determined by a Pfeiffer QMS 200 type mass spectrometer coupled with a Setaram LABSYS type thermogravimetric instrument (TG-MS). The measurements were carried out under N_2 atmosphere, and the heating rate was set to 10 °C/minute in 30 – 1000 °C temperature range.

4.7. Cellular measurements

4.7.1. Cell line

HeLa cells (ATCC-CCL-2) were grown in DMEM containing 10 % FBS, 1X Kanamycin sulfate, 1X Antibiotic-Antimycotic solution and 1X GlutaMaxTM supplement. Cells were grown in a humidified incubator at 37 °C in 95 % relative humidity and 5 % CO_2.

4.7.2. Apoptosis/necrosis cell viability assay

Apoptosis/necrosis detection assay kit (Abcam) were taking place to determine cell death. First, HeLa cells were plated onto cover glass in a 6-well plate and treated with the appropriate amount of dLDHaHtSC (20 mg/L) and CMA3 (5 mg/L) samples for 30 minutes. After the treatment with the active components, the cells were washed twice with the assay buffer followed by incubation in a reaction mixture containing 100-time diluted Apopxin Green, 200-time diluted 7-AAD, and 200-time diluted Cytocalcein 450 in assay buffer for 30 minutes at 37 °C in a humidified incubator. Apopxin Green can detect apoptotic, 7-AAD the necrotic, while Cytocalcein Violet the healthy cells. After the cells were washed twice with fresh assay buffer, they were measured with a Zeiss LSM 880 confocal microscope at excitation/emission wavelength of 490/525 nm for Apopxin Green, 550/650 nm for 7-AAD, and 405/450 nm for Cytocalcein Violet 450.

4.7.3. CellTiter-Glo® 3D cell viability assay

The CellTiter-Glo® 3D cell viability assay is based on the quantification of the adenosine triphosphate (ATP) level in cell cultures, which could serve as a marker of the normal, metabolically active cells. The amount of ATP detected is in line with the number of viable cells present in the culture. The assay is based on the sign caused by the luciferase enzyme that can generate a stable “glow-type” luminescent signal.

The kit was removed from -20 °C and placed to +4 °C overnight. The assay buffer was equilibrated at room temperature for 30 minutes before the experiments. HeLa cells were plated onto a white, flat-bottomed microplate at 1 x 10a cell/well density. After the cells reached 80–90 % confluency, the cells were washed with warm sterile DPBS to remove culturing media. After the supernatant was removed, the cells were treated with the adjusted concentration of the CMA nanozymes in warm Hepes for 1 hour at 37 °C in a humidified atmosphere. The supernatant was removed, and the cells were washed with warm Hepes.

100 μL/well CellTiter-Glo® 3D reagent was added to the well and the microplates were transferred to a BMG Fluostar Optima Microplate Reader at room temperature. The reaction mixture was being shaken for 5 min and the measurements started after 25 min activation time. Data were normalized to protein mass concentration measured by Bradford protein assay. 4 μL from the 10-times diluted samples was mixed with 196 μL Bradford reagents in a flat bottom and transparent microplate. The microplate was transferred to a BMG Fluostar Optima microplate reader at room temperature. The measurement was started after 5 min mild shaking and the absorbance was measured at 595 nm wavelength.

4.7.4. Intracellular oxidative stress detection assay

Intracellular ROS concentration measurements based on former experiments.[127] First, cells were incubated with the appropriate amount of the active material (20 mg/L dLDHaHtSC and 5 mg/L CMA3) for 30 minutes (from which 20 minutes was loading with the oxidative stress generator H2DCFDA). After preincubation, cells were plated onto cover glasses and mounted on and Olympus IC71 fluorescent microscope equipped with an MT-20 illumination system. Cells were initially perfused with HEPES buffer only (pH 7.5, 2 minutes), which was followed by the perfusion of 50 μM menadione in the same HEPES buffer. The excitation wavelength was 495 nm, while the emission wavelength was 525 nm. The fluorescent signals were collected for the appropriate time with 5 s intervals. Filter set for BCECF-AM was described elsewhere.[177]

4.7.5. Evaluating intracellular ROS and superoxide levels

During ROS/superoxide level detection assay an oxidative stress detection reagent (Green, EX/Em 490/525 nm) and a superoxide detection reagent (Orange, Ex/Em 550/620 nm) was applied to detect ROS and superoxide molecules. The HeLa cells were grown on a glass bottom 96 well black microplate in 1x 10^4 cell/well density. The treatments were performed at 37 °C under a humidified atmosphere. Cells were treated with CMA samples of an appropriate concentration for 1 hour, then the cells were washed with warm Hepes. Thereafter the cells were treated with 50 μM menadione for 15 min and then with the fluorescent dyes for 30 min. The intracellular fluorescence levels were detected by a BMG Optima Fluostar Microplate Reader at sufficient excitation/emission wavelengths.

4.7.6. ROS induced DNA double strand break visualization

The HeLa cells grown on cover glasses were incubated with 20 mg/L dLDHaHtSC for 30 minutes. The cells were first washed with 1X PBS, then were treated with 50 μM H_2O_2 in HeLa feeding media for 40 minutes. Thereafter the cells were fixed in 4% paraformaldehyde in PBS for 15 minutes and then washed in 1X PBS for 3 × 5 minutes. Antigen retrieval was performed by 0.01% Triton-X-100 for 15 minutes which was followed another washing step (1X PBS, 3 × 5 minutes). Cells were blocked with 10% BSA-PBS for 2 h at 37 °C, then the primary antibody against γH2AX histone (diluted in 1:400 with 10% BSA-PBS) was administered, and then it was incubated at 4 °C overnight. After a washing step (1X PBS for 3 × 5 minutes) secondary antibody (Alexa Fluor 488 Goat anti-Rabbit) was used in 1:800 dilution with 10% BSA-PBS and incubated for 3 h at room temperature under light protection. Nuclear staining and mounting were carried out at the same time with ProLong™ Gold Antifade mounting medium DAPI and microscope slides (Fisher Scientific). Fiji ImageJ2 (Version: 2.3.0/153f) software was used for statistical analysis, while number and intensity values of γH2AX were calculated by Foci Picker3D plug-in.

4.7.7. Direct stochastic optical reconstruction microscopy (dSTORM) measurements to detect cell penetration

The dSTORM images were collected with a Nanoimager S (Oxford Nanoimaging ONI Ltd) instrument. The HeLa cells were treated, fixed, permeabilized and the nonspecific binding sites were blocked as described above for γH2AX immunofluorescence labelling. The anti-CAT, anti-SOD1 antibodies were used with anti-HRP monoclonal antibody in dual labelling setups to determine double positive enzyme particles. The primary antibodies were diluted in 1:200 ratio with 10% BSA-PBS and applied along with the samples after an incubation of 4 °C carried out overnight. Then the samples were washed (3 × 10 minutes) with 1X PBS. 1:400 dilution with 10% BSA-PBS of Goat anti-Rabbit Alexa Fluor 568 and Donkey anti-Mouse Alexa Fluor 647 secondary antibodies were used, followed by another washing step with sterile 1X PBS (3 × 10 minutes). Thereafter, the cover glasses were placed on cavity slides (Sigma) filled with blinking buffer (100 U glucose oxidase, 2000 U CAT, 55.56 mM glucose, 100 mM cysteamine hydrochloride in 1 mL sterile PBS) and sealed with two-component adhesive (Picodent).

4.7.8. Statistical analysis of cellular measurements

GraphPad Prism software was used for statistical analysis. All data are expressed as ± standard error of the mean. Parametric and nonparametric tests were used based on the normality of data distribution. The P value below 0.05 was considered statistically significant (determined by GraphPad Prism software).

5. Results and Discussion

5.1. Recovery of the lamellar structure of dLDH particles in the presence of monovalent electrolytes

The main subject of this chapter is the study of the restacking mechanism of dLDH particles. First, the restacking mechanism was investigated by DLS and turbidity measurements, while it was further confirmed by AFM and XRD results. The addition of electrolyte solution led to the reconstruction of the lamellar LDH structure, which was followed by randomly oriented aggregation. After demonstrating the recovery procedure of dLDH particles, the salt-induced aggregation mechanism of the lamellar form was also investigated.

5.1.1. Structural characterization of dLDH particles

As described in the *Chapter 4.2.1.*, a general procedure was used to synthesize the dLDH dispersion. To confirm the delaminated structure of the dLDH particles, first, XRD measurements were carried out. The XRD pattern collected for the dLDH dispersion is shown in Figure 14 (A).

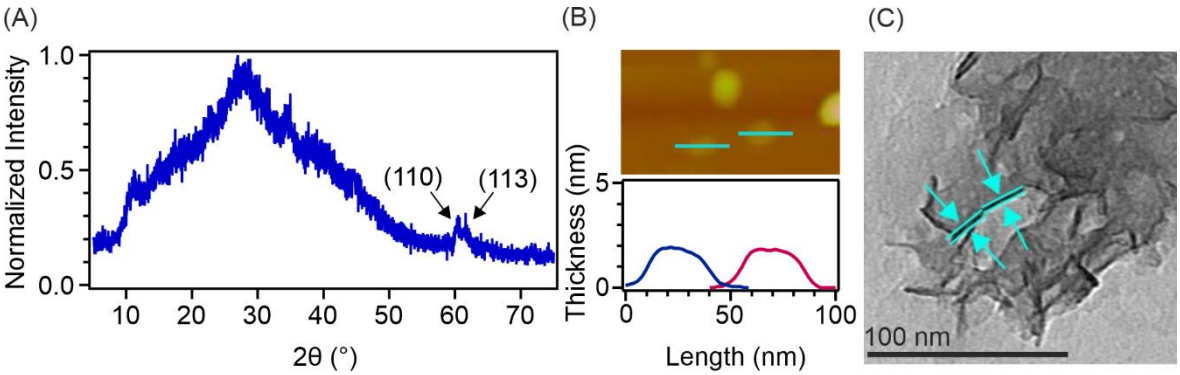

Figure 14. X-ray diffractogram (A) AFM (B) and TEM (C) image of dLDH particles. The graph below the AFM image shows the thickness of the labelled particles. The light blue arrows in the TEM image represent the thickness of the particles.[178]

It can be concluded that no characteristic reflection appeared on the diffractogram, indicating the presence of LDH nanosheets in the dispersion. Moreover, the presence of two characteristic reflections around 61° 2θ value confirmed the formation of unilamellar dLDH particles.[69] The thickness of the dLDH nanosheets determined from AFM images was (1.75 ± 0.25) nm (Figure 14 (B)) thus the particles were composed of only 2-3 double hydroxide layers.[179] The TEM image (Figure 14 (C)) further confirmed the presence of dLDH

nanosheets, as the thickness determined from the particles oriented perpendicular to the viewer was (1.75 ± 0.33) nm. This value showed excellent agreement with the thickness determined from the AFM results.

The 2D nanosheet structure of the dLDH particles was also revealed by SAXS measurements, where solid LDH particles were measured using a benchtop SAXS device, while dLDH dispersions (at 3 different concentrations) were analyzed at the EMBL BioSAXS synchrotron beamline (Hamburg, Germany). The results clearly show the difference between dLDH nanosheets and lamellar LDH particles. For an ideal two-phase structure with a smooth surface of an individual lamella, the scattering intensity has an asymptotic behavior (Figure 15 (A)), however, any discrepancy (e.g., electron density fluctuation, stacked structure) can cause a positive deviation from the asymptotic feature (Figure 15 (B)).[174, 175, 180] Quantification of the results with the Porod's law (Eq. 21.), a slope equal to 4 at $h > 0.5$ nm^{-1} scattering angles unambiguously indicated the flat surface (i.e., single nanosheet with a smooth surface), while the divergence from the power law h^{-3} referred to the stacked, lamellar structure.

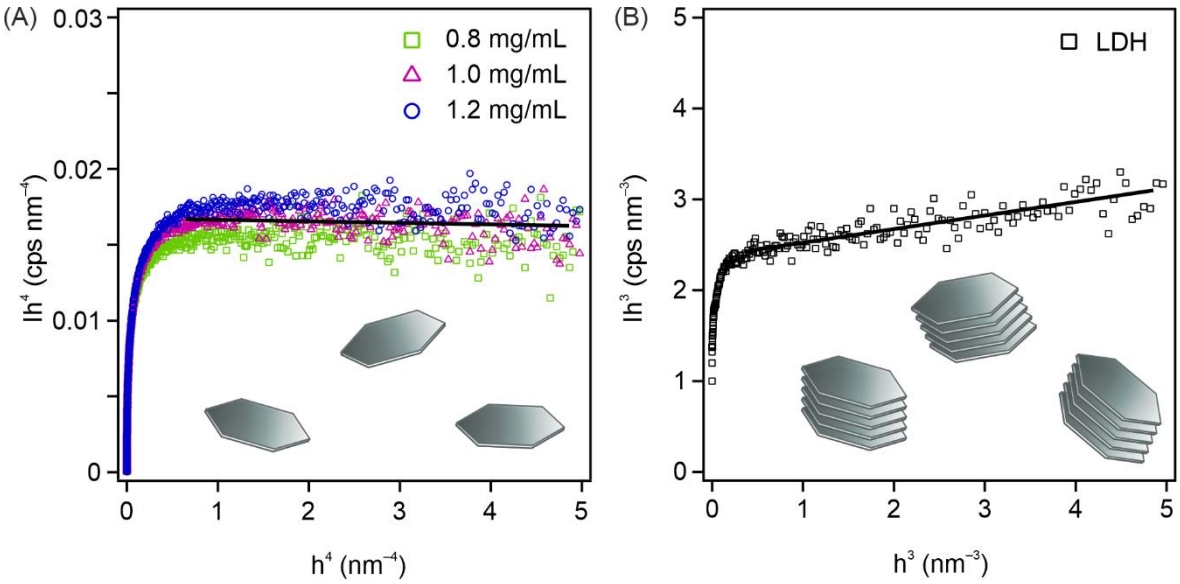

Figure 15. Scattering intensity (I(h)) versus scattering vector (h) for dLDH dispersions (A) and LDH particles (B).[181]

5.1.2. Salt-induced restacking and aggregation mechanism of dLDH particles

In order to understand the restacking and aggregation mechanisms of the dLDH particles, salt-induced DLS measurements were carried out. The particle concentration was kept constant (10 mg/L), while the salt concentration was systematically varied. Time-resolved DLS measurements tracked the change in hydrodynamic radii over time at different

NaCl doses (Figure 16 (A)). No change in size was observed at low NaCl concentration, i.e., the dispersion was stable. However, with increasing electrolyte concentrations in the reaction mixture, the hydrodynamic radii started to increase after a certain time. Accordingly, the time-resolved plots could be divided into two parts. In the first regime, no change occurred in particle size, but in the second regime the hydrodynamic radii increased steeply. The time that divided the aggregation process into two well distinct regimes was referred to as the critical coagulation time (CCT). The change in particle size in the second regime was in good agreement with the DLVO theory (see *Chapter 2.3.*).[146]

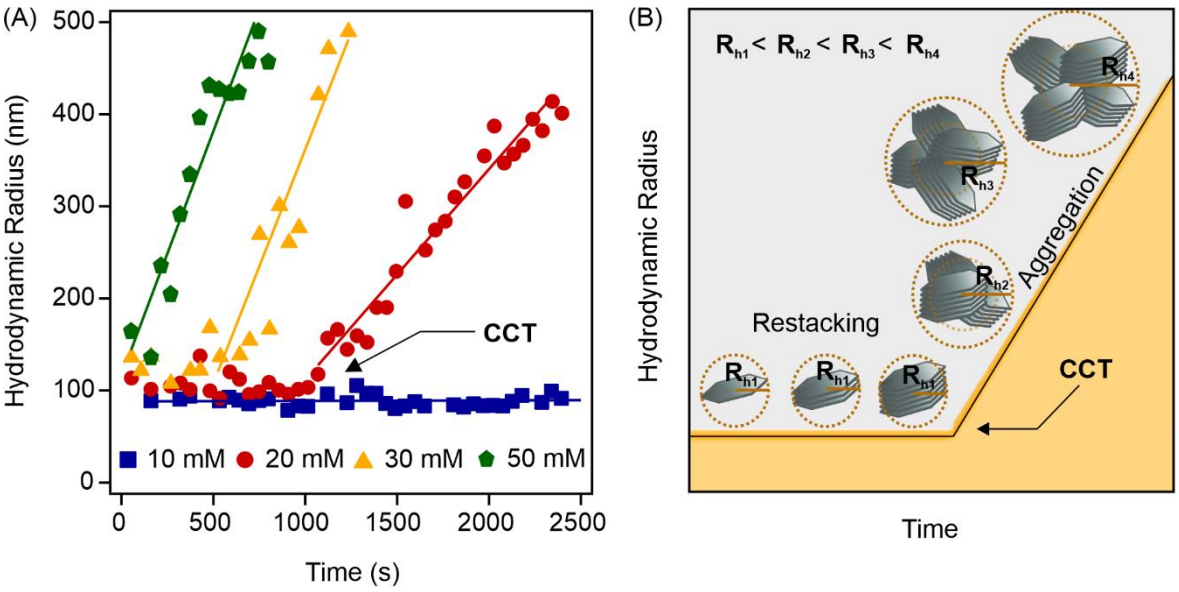

Figure 16. Hydrodynamic radius as a function of time, measured by DLS (A) and the schematic representation of the restacking and aggregation mechanisms in time (B). The yellow dashed-line circles represent the spheres that can be drawn around the restacked and aggregated dLDH particles.[178]

Considering that aggregation must start immediately with the addition of electrolyte to the reaction mixture, the constant radius data in the first regime can be explained as follows. The hydrodynamic radius for plate-like particles can be defined as the largest dimension of the scattering object. As represented in Figure 16 (B), the hydrodynamic radius of dLDH particles is equal to the radius of a sphere that can be drawn around the solvated particles. Therefore, no significant change was detected in the case of the restacking of the nanosheets since the contribution of the thickness to the radius is minor. The main driving force for the formation of the original stacked LDH structure is the attachment of solvent water molecules to the metal hydroxide layers, resulting in hydrogen bonds between the nanosheets.[182] After restacking, i.e., after CCT, the particles start to randomly aggregate and form house-of-card clusters, leading to a significant increase in the hydrodynamic radii.[183]

With increasing NaCl concentration, the initial lag phase became shorter, while after 50 mM NaCl concentration it completely disappeared, as the addition of electrolyte caused rapid (shorter than the time scale of one DLS run) restacking and aggregation.

The same phenomenon was observed in turbidity measurements. The change in relative turbidity could be divided into two regimes separated by a well-defined breakpoint, denoted also as CCT (Figure 17 (A)). Such a technique can also be used to study colloidal stability as it is very sensitive to changes in both particle size and concentration, even for non-spherical particles. Since the initial dLDH dispersion is relatively transparent for turbidity measurements, restacking led to a stronger scattering effect, hence a significant increase in relative turbidity. After rebuilding the original lamellar structure beyond the CCT, the steep increase in turbidity slowed down and the change became less significant. This second regime was again assigned to the formation of house-of-cards aggregates and hence, the tendencies in turbidity and hydrodynamic radius were qualitatively very similar.

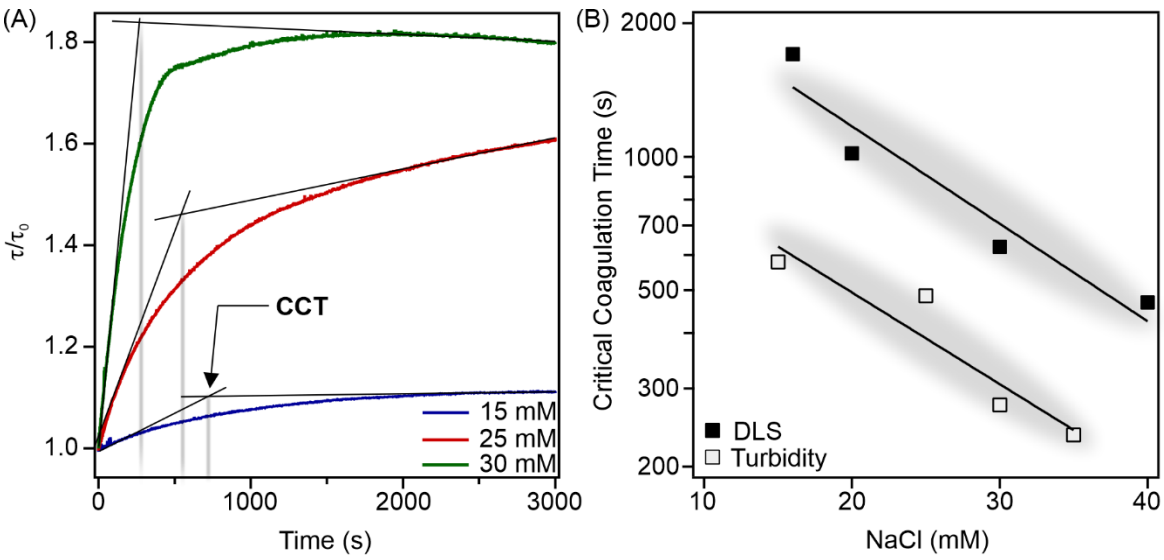

Figure 17. Relative turbidity as a function of time (A) and CCT values calculated based on DLS and turbidity measurements as a function of NaCl concentration (B).[178]

The formation of lamellar and randomly oriented aggregates is similar to chemical precipitation occurs in highly supersaturated solutions. The crystal growth process ends with a nucleation step, in which a small number of ions, atoms or molecules (denoted as reactants) became arranged, providing building blocks for the subsequent crystal growth. This explanation implies that dLDHs are reactants that first form the lamellar structured subunits (LDHs), whose further random aggregation resulted in the final product, as in the polynuclear crystal growth mechanism. It is therefore assumed that the two regimes can be

defined as oriented and random aggregation phases, as the turbidity CCT values became smaller with increasing electrolyte concentrations in the reaction mixture.

To illustrate the relation between data from DLS and turbidity measurements, the change in CCT values as a function of the concentration showed a similar tendency (Figure 17 (B)). There is a difference in the absolute CCT values due to the fact that turbidity is less sensitive than the DLS method and therefore a 200-times higher dLDH concentration was used in these measurements. It can be assumed that aggregation may occur at this high particle concentration, however, the XRD measurements shown in Figure 14 (A) were carried out under similar conditions. As mentioned earlier, shorter first regimes were observed for both methods by increasing the salt concentration and thus, CCTs decreased significantly by increasing the ionic strength. Despite the difference in the absolute CCT values, the trend remained the same for both methods, and the exponents of the fitted exponential functions overlap within the experimental error (–0.051 ± 0.004 and –0.048 ± 0.003 for DLS and turbidity measurements, respectively). This further strengthens the argument that the dLDH particles aggregated with similar mechanisms in DLS and turbidity methods and hence, both methods were useful to study such a phenomenon.

5.1.3. Confirmation of the restacking mechanism by AFM and XRD measurements

To further evaluate the restacking mechanism followed by random aggregation processes, AFM and XRD measurements were carried out. The AFM images of the dLDH particles mixed with salt solution were recorded at different time intervals and the corresponding height profiles are shown in Figure 18 (A). The addition of the salt solution caused first the restacking of the lamellar structure, while after a certain time to the aggregation of the LDH particles. The thickness systematically increased with the time and after 3 minutes, it was (6.02 ± 0.75) nm indicating the formation of the lamellar structure. The lateral size of the particles did not change significantly in the restacking regime, further strengthening the DLS results and confirming why the hydrodynamic radii did not change during the formation of the lamellar structure. After 20 minutes, when the particles reached the aggregation phase (i.e., after CCT), large clusters were detected on the AFM micrograph.

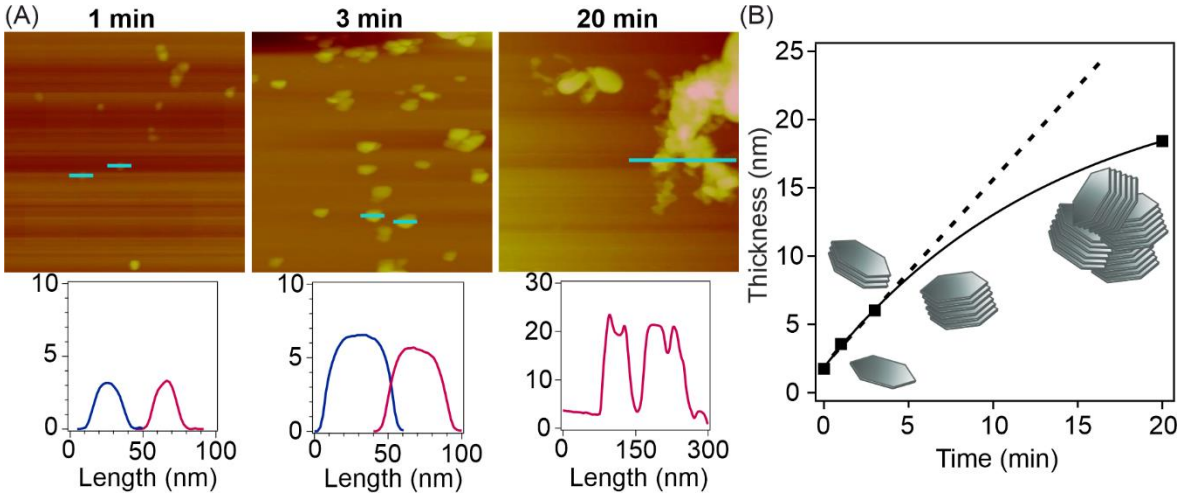

Figure 18. AFM images and height profiles of dLDH particles mixed with NaCl solution recorded in different time intervals indicated above the images (A). Layer thickness as a function of time after adjusting the NaCl concentration to 30 mM (B). The dotted line represents the linear trend for the first three thickness values, while the solid line corresponds to the fitted function.[178]

The tendency in layer thickness over time is shown in Figure 18 (B). The thickness increased linearly within a short period, while the curve reached a plateau after a certain time. The tendency in layer thickness also confirmed the hypothesis that nanosheet restacking occurred in the first regime, while larger aggregates formed after CCT. After a time interval of 20 minutes, the average thickness was (18.42 ±5.21) nm. The formation of the saturation plateau further confirms our theory about the formation of house-of-cards aggregates, namely, unlike the growing layer thickness, the lateral dimension of the formed aggregates was significantly larger, than that of the individual particles.

XRD measurements were also performed at 30 mM and 50 mM salt concentrations (Figure 19). There was no significant difference between the diffractograms of the dLDH particles and those recorded 3 minutes after the 30 mM NaCl concentration was adjusted, as the few layers that were restacked did not show the appearance of the characteristic reflections of the LDHs. After 10 and 20 minutes, the reflections of the LDH-like structure appeared and their intensity increased with time, while at 50 mM concentration, well-defined reflections appeared immediately after mixing the particle dispersion with the NaCl solution. The specific surface areas calculated from the N_2 adsorption isotherms are shown in the corresponding diffractograms. The values agreed well with the ones for the specific surface area data found in the literature.[184] Besides, these data are in good agreement with the number of the layers stacked on top of each other, because after restacking/aggregation, the specific surface area of the LDH particles decreased significantly. The TEM image recorded on the aggregated LDHs 20 min after maintaining the 30 mM NaCl concentration is shown

in Figure S1. The morphology of the restacked, and aggregated LDH particles formed flower-like motifs, similar to the organic solvent-treated LDH particles reported earlier.[184]

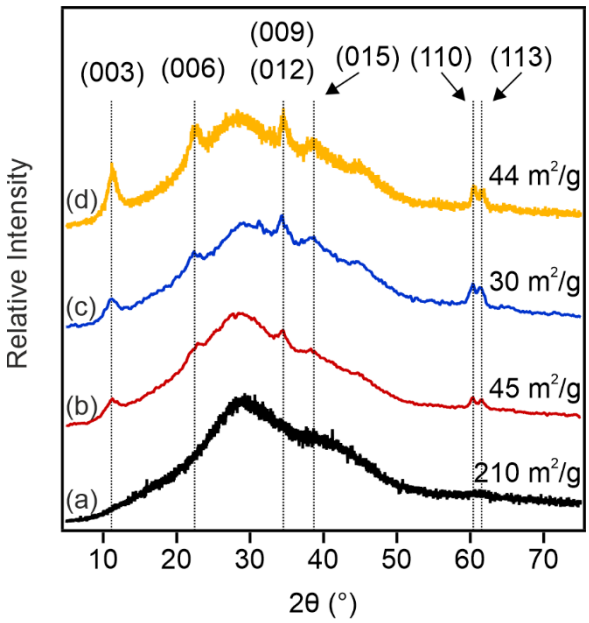

Figure 19. XRD diffractograms recorded at 3 min (a), 10 min (b) and 20 min (d) after setting the salt concentration to 30 mM and immediately after setting the 50 mM NaCl concentration. The specific surface area values are also indicated.[178]

In summary, results from both experimental techniques established the presence of a two-step restacking/aggregation mechanism for dLDH in the presence of monovalent salt. Data from AFM, XRD and the specific surface area measurements showed a good correlation with the tendencies obtained from the DLS and turbidity measurements. The development of the lamellar LDH structure was followed by the formation of randomly oriented aggregates, where the two regimes are separated by a well-defined boundary (CCT).

5.1.4. Determination of colloidal stability from DLS and turbidity measurements

Colloidal stability and charging properties were also studied by DLS and turbidity measurements. The zeta potential values were determined in a wide range of NaCl concentrations (inset of Figure 20). The charge of the particles decreased with increasing electrolyte concentration and remained positive in the concentration range studied. The experimental data were fitted with the Gouy-Chapman model (Eq. 7), which describes the change in potentials of the electrical double layer at different ionic strengths. Note that the deviation at lower salt concentrations is due to the limitation of the Gouy-Chapman model, namely that it is suitable for the range of high electrolyte concentrations.[142] The model provides a consistent approximation to the charge density at the slip plane at higher ionic

strengths, which in the case of the dLDH particles was +18 mC/m^2. This value was in good agreement with other data found in the literature for LDH particles.[183, 185]

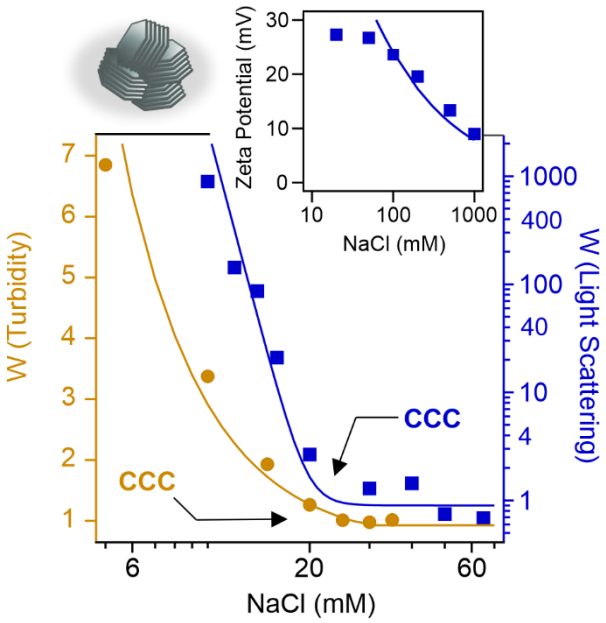

Figure 20. Stability ratios, determined in time-resolved DLS (blue squares) and turbidity (yellow spheres) measurements as a function of NaCl concentration. The inset shows the zeta potential values obtained under the same experimental conditions. The zeta potential values were fitted by the Eq. 7, while the stability data were fitted by the Eq. 10.[178]

Finally, the salt-induced aggregation rates were determined and the stability ratios were calculated and plotted against NaCl concentration (Figure 20). The tendencies in data obtained from the two methods showed similarity. First, the dispersions were stable at low electrolyte concentrations, then slow aggregation occurred when the salt concentration increased, which was followed by rapid particle aggregation after the CCC. The change in hydrodynamic radius is shown in Figure 16 (A), while the change in relative turbidity values is presented in Figure S2. The CCCs determined from turbidity (16 mM) and DLS (20 mM) measurements were in good agreement. Such CCC values are in line with former CCCs determined for LDH particle dispersions. The results clearly indicate the presence of DLVO-type forces.[183, 185]

5.2. Functionalization of dLDH particles with antioxidant enzymes

After exploring the structural and colloidal properties of the dLDH dispersions, three antioxidant enzymes (HRP, SOD, CAT) were immobilized within an LDH-based composite using polyelectrolytes (Alg, TMC) in the sequential adsorption method monitored by ELS measurements. After anchoring the enzymes on the particle surface, chemical test reactions

and subsequent cellular measurements were carried out to evaluate the ROS decomposition ability of the nanocomposite.

5.2.1. Immobilization of polyelectrolytes and antioxidant enzymes

First, the dLDH particles were functionalized with oppositely charged Alg polyelectrolytes to adjust their surface charge. The adsorption was monitored using zeta potential measurement, which is plotted as a function of the polyelectrolyte doses in Figure 21.

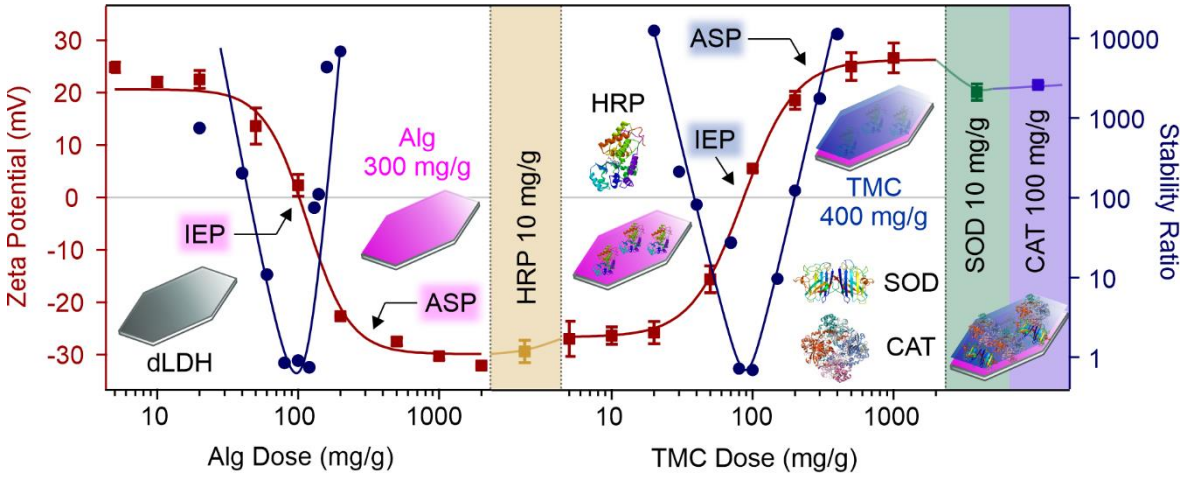

Figure 21. Change in zeta potential (squares, left axis) and stability ratio (circles, right axis) due to the adsorption of polyelectrolytes and enzymes on the dLDH surface. Note that the mg/g values mean mg polyelectrolyte/1 g of dLDH. The lines serve to guide the eyes. During these measurements, the dLDH concentration was maintained at 10 mg/L, while 1 mM NaCl was set as the background electrolyte.[181]

At low Alg doses (below 20 mg/g), the charge of the dLDH particles did not change significantly and remained positive indicated with zeta potential values of approximately +20 mV. With increasing Alg dose, charge neutralization occurred and the system reached the IEP at about 100 mg/g. Beyond this dose, the dLDH platelets became negatively charged with further increasing Alg concentration exhibiting the so-called overcharging or charge reversal effect.[155] The system reached the ASP at 200 mg/g Alg dose, indicating that the nanoplates were completely covered with polyelectrolytes and above this polyelectrolyte concentration, the excess amount of Alg remained in the solution. The zeta potential of dLDH particles functionalized with 200 mg/g or more Alg was ~ -30 mV. Similar behavior has already been observed for other LDH/polyelectrolyte systems.[160, 186]

The stability ratio values were determined by DLS measurements performed in the same Alg dose range as the zeta potential experiments. The results were in good qualitative

agreement with the prediction of the DLVO theory. Accordingly, at low polyelectrolyte doses, where the particles retained their high positive surface charge, the dispersion was stable due to the strong EDL forces. By increasing the polyelectrolyte concentration and reaching the IEP, the dispersion became unstable due to the charge neutralization effect of the polyelectrolytes. With the decrease of the repulsive electrostatic interactions, the attractive van der Waals forces between the neutralized particles became predominant, resulting in fast aggregation. By further increasing the polyelectrolyte concentration, beyond the ASP, the repulsive forces reappeared and the dispersions showed great colloidal stability. Consequently, the change of the stability ratio could be described with a U-shaped curve which is characteristic for particle/polyelectrolyte systems.[160, 186] The change in the hydrodynamic radius values is shown in Figure S3 for some samples. Based on the zeta potential and stability ratio measurements, 300 mg/g Alg dose (dLDH/Alg) was selected for the further measurements.

A similar trend was observed for the TMC coating, however, with opposite charge balance (Figure 21 and Figure S3). Initially, no change in zeta potential occurred, the dispersion was stable. Near the IEP where the particles were neutralized, rapid particle aggregation took place, while higher TMC doses resulted in highly charged particles with strong EDL forces giving rise to stable dispersions. Based on these results, 400 mg/g TMC dose (dLDH/Alg/TMC) was selected for further measurements.

The antioxidant enzymes were immobilized together with polyelectrolytes on the dLDH support. HRP as a positively charged peroxidase enzyme[128] was adsorbed on the negatively charged dLDH/Alg surface, while the negatively charged SOD and CAT were immobilized on the dLDH/Alg/HRP/TMC surface. The final composite contained 10 mg/g, 10 mg/g and 100 mg/g of HRP, SOD and CAT, respectively. As shown in Figure 21, the enzyme immobilization had no effect on the surface charge, so the repulsive electrical double layer forces remained dominant, and the composite exhibited high colloidal stability. In conclusion, the final composite (denoted as dLDHaHtSC) contained the polyelectrolytes and enzymes in the following order: 300 mg/g Alg, 10 mg/g HRP, 400 mg/g TMC, 10 mg/g SOD and 100 mg/g CAT.

5.2.2. Colloidal stability of polyelectrolyte coated dLDH particles

Colloidal stability plays a major role in biomedical applications, as undesired aggregation of particles can lead to serious consequences (e.g., formation of blood clots).

Polyelectrolyte adsorption can improve the aggregation properties and, in some cases, the cell penetration ability of the particles. Therefore, the understanding of salt-induced aggregation is an important task for nanocomposites potentially used in biomedical fields.

The charging properties were first investigated by changing the electrolyte concentration in the reaction mixtures (inset of Figure 22). Due to the screening effect of the counter-ions present in the solution, the absolute value of the zeta potential decreased for both dLDH/Alg and dLDH/Alg/TMC. The points were fitted using the Gouy-Chapman model (Eq. 7), from which surface charge densities of –25 mC/m^2 and +8 mC/m^2 were calculated for dLDH/Alg and dLDH/Alg/TMC, respectively. The parameters determined by DLS and ELS measurements are summarized in Table 2.

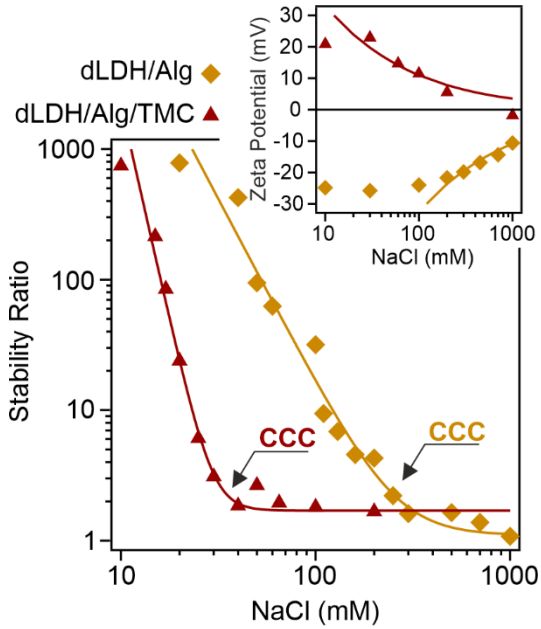

Figure 22. Salt-induced aggregation of dLDH/Alg (yellow diamonds) and dLDH/Alg/TMC (red triangles) particles. The inset shows the salt dependent zeta potential values. The zeta potential values were fitted by Eq. 7, while the stability data were fitted by Eq. 10.[181]

The results of the salt-induced aggregation (Figure 22) showed similar tendencies to the previously described dLDH dispersions. At low NaCl concentration, the dispersion was stable, no change in the hydrodynamic radius was observed, while increasing the electrolyte concentration led to the formation of particle aggregates (Figure S4). The CCC separated the slow and fast aggregation regimes. The CCCs calculated for dLDH/Alg and dLDH/Alg/TMC were 265 mM and 33 mM, respectively. In both cases, the value was higher than that of the dLDH particles without polyelectrolyte coating on their surface. Based on the charge density values, the high colloidal stability of dLDH/Alg can be attributed to the remarkable repulsive EDL forces. However, there is an opposite trend for dLDH/Alg/TMC.

The surface charge density was lower than for the bare dLDH particles, the CCC value increased after the polyelectrolyte adsorption. This deviation from the DLVO prediction could be explained by the steric effect between the overlapping polyelectrolyte layers adsorbed on the particle surface.[157] This overlapping phenomenon resulted in an increase in osmotic pressure upon approach of dLDH/Alg/TMC particles giving rise to the development of a repulsive force of non-DLVO origin.

Table 2. Colloid parameters determined by DLS and ELS measurements.

Sample	R_h (nm)[a]	PDI[b]	σ (mC/m^2)[c]	CCC (mM)[d]
dLDH	89.0 ± 6.0	0.266	18	20
dLDH/Alg	149.0 ± 8.9	0.215	-25	265
dLDH/Alg/TMC	134.4 ± 5.0	0.236	8	33

[a]Average hydrodynamic radius value, calculated from the hydrodynamic radii measured at 10 mM NaCl concentration. [b]Polydispersity index, averaging the values measured by the DLS at 10 mM NaCl concentration. [c]Surface charge density values calculated by Eq 6. [d]CCC values calculated with the Eq 9.

5.2.3. Investigation of the structural and morphological characteristics of dLDHaHtSC

To confirm the structural changes upon immobilization of polyelectrolytes and enzymes on the particle surface, synchrotron SAXS measurements were performed in dispersions (Figure 23 (A) and Figure S5).[173] By fitting the slopes (S) on the scattering curves in the small angle regime ($h < 0.1$ nm^{-1}) the morphological and surface properties could be revealed. For dLDH dispersions without surface modification, the power law decay of the scattering curve at small angles (S = 2) is typical for delaminated structures with smooth surfaces (Figure 23 (B)).[175, 187] By increasing the number of polyelectrolyte and enzyme layers on the surface by the sequential adsorption method, the value of the exponent increased to S = 2.3. This change indicated an increase in electron density fluctuations at the interface, which means that the surface of the nanosheets became more diffuse after functionalization with polyelectrolytes and enzymes. The formation of the diffuse structure indicated that the macromolecules did not adsorb on the surface in a homogenous layer, but rather in a random assembly (illustrated in Figure 23 (B)). The TEM images did not show any morphological changes compared to the bare dLDH particles (Figure S6), the shape and size of the particles were typical for LDH nanosheets.

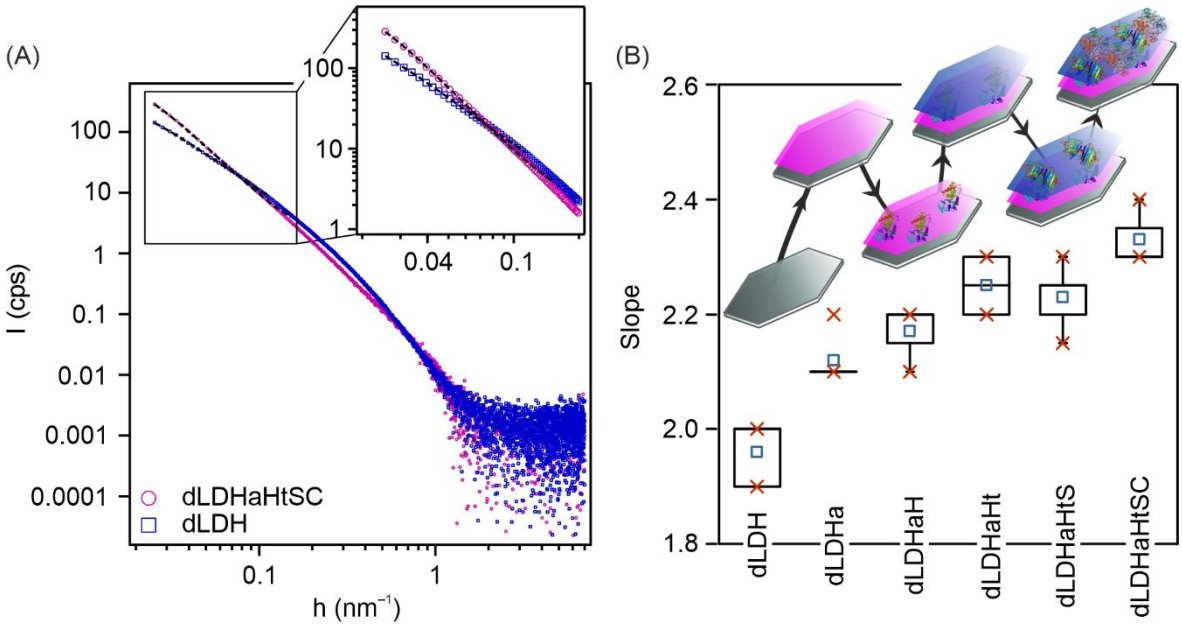

Figure 23. Double logarithmic representation of the scattering curves for dLDH and dLDHaHtSC dispersions (A) and the box diagram representation of the slopes of the fitted lines in the small angle range for the subsystems of dLDHaHtSC (B). The center lines indicate the median, the mean is represented by the empty squares in the middle of the boxes, while the "x" marks at the top and bottom of the boxes indicate the 75% and 25%, while the whiskers show the minimum and maximum values. The inset in (B) is the schematic representation of the formation of the diffuse layer.[181]

5.2.4. Enzymatic activity of dLDHaHtSC revealed in chemical test reactions

To estimate the enzyme-like activity of the dLDHaHtSC composite, three types of chemical test reactions were performed. First, HRP activity was investigated in the guaiacol assay.[169] During the test reaction, the peroxidase enzyme decomposes H_2O_2 to H_2O and O_2, and the in-situ generated O_2 can oxidize the guaiacol molecules, which produces brown-colored tetra-guaiacol in the reaction mixture. The formation of tetra-guaiacol was monitored with a UV-VIS spectrophotometer. The reaction rates were calculated from the absorbance change measured for the native HRP and for dLHDaHtSC. The maximum reaction rate (v_{max}) and the Michaelis constant (K_M, which defines the substrate concentration at which the reaction velocity is half of the v_{max}) were determined by fitting the points with the Michaelis-Menten model[170] (Figure 24 (A)).

Both K_M and v_{max} values – applied as activity markers – decreased upon immobilization of HRP on the particle surface. The decrease in the K_M value implies that the enzyme had a higher affinity for the substrate after immobilization, which is unusual compared to the literature data published so far.[125, 127] This can be explained as the adsorption of the substrate on the particle surface, as guaiacol molecules are attracted to the positively

charged particle surface and, as a result, are more accessible for the immobilized enzymes than for the native ones.

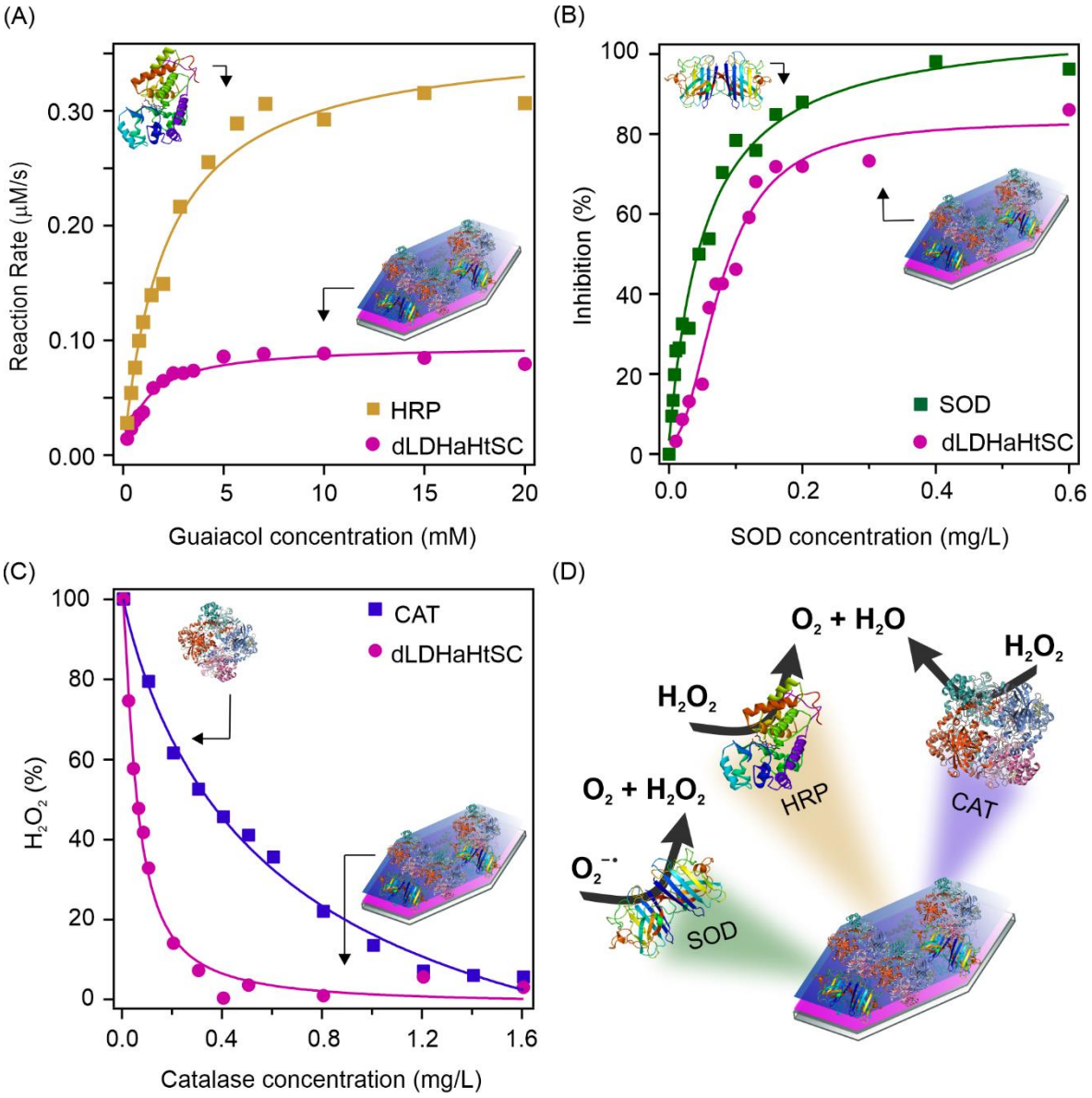

Figure 24. HRP (A), SOD (B) and catalase (C) assay for the determination of enzymatic activities. The native enzymes are labelled with squares, while the pink spheres represent the data for dLDHaHtSC composite. The dashed lines are fitted curves to calculate the key parameters describing the enzymatic activity. The schematic representation of the reactions catalyzed by the enzymes (D).[181]

The SOD activity of the composites was estimated with the Fridovich assay.[168] During the test reaction, a color change can be observed due to the reaction between NBT and the superoxide radicals, produced in the xanthine oxidase catalyzed oxidation of xanthine to uric acid. The SOD enzyme decomposes superoxide radicals and thus, inhibits the reduction of NBT and prevents the color change. The inhibition values as a function of SOD concentration and the fitted curves are marked in Figure 24 (B). The IC_{50} values, the

enzyme concentration required for the decomposition of 50% of the superoxide radicals, were calculated based on the fits. No significant change in the IC_{50} and maximal inhibition (I_{max}) values was observed after immobilization of SOD enzyme; therefore, the adsorption had negligible influence on the activity of the enzyme. This observation is consistent with previous reports of immobilized SOD enzymes.[126, 127]

In the catalase assay, the formation of a colored complex between ammonium molybdate and H_2O_2 provides the opportunity to detect the activity of the bare CAT and the dLDHaHtSC composite.[171] The complex could not be formed in the presence of the enzyme/dLDHaHtSC, resulting in a decrease in absorbance. The remaining H_2O_2 percentage in the reaction mixture was plotted against the catalase concentration in Figure 24 (C), and the EC_{50} values (the enzyme concentration that can decompose half the amount of H_2O_2 present in the solution) were calculated based on the fitted curves. Surprisingly, the immobilized CAT showed a significantly higher H_2O_2 decomposition ability, and EC_{50} value decreased remarkably compared to the native enzyme. This finding is in contrast to the previous reports for immobilized CAT.[188, 189] It is likely due to the higher affinity of the H_2O_2 molecules to the particle surface, which provides a higher affinity for the enzyme.

To summarize the results of the enzymatic activity tests, it was shown that the enzymes kept their activity upon immobilization on the surface and in some cases even increased their activity by immobilization. HRP revealed higher affinity to the substrate molecule, CAT also showed a higher H_2O_2 decomposition ability, while the activity of SOD did not significantly change upon immobilization on dLDH particles. The parameters describing the enzymatic activity were summarized in Table 3.

Table 3. Enzymatic activity parameters determined for native and immobilized enzymes.

Sample	v_{max} (μM/s)[a]	K_M (mM)[b]	IC_{50} (mg/L)[c]	I_{max} (%)[d]	EC_{50} (mg/L)[e]
HRP	0.370 ± 0.010	2.12 ± 0.24	—	—	—
SOD	—	—	0.053 ± 0.007	94.2 ± 5.1	—
CAT	—	—	—	—	0.660 ± 0.230
dLDHaHtSC	0.096 ± 0.004	1.13 ± 0.15	0.079 ± 0.007	77.1 ± 7.8	0.056 ± 0.005

[a]v_{max} and [b]K_M values calculated from the Michaelis-Menten plots. [c]IC_{50} values determined from the inhibition curves. [d]I_{max} values are the plateau of the inhibition curves. [e]EC50 values determined from the H_2O_2% vs CAT concentration curves.

5.2.5. Intracellular activity of dLDHaHtSC

To evaluate the intracellular activity of dLDHaHtSC, measurements on HeLa cells were performed. First, the cytocompatibility of the composite was tested with a simple

apoptosis/necrosis detection assay, then their cell penetration ability was examined using dSTORM method. Besides, intracellular ROS scavenging activity and DNA double strand break prohibition were tested.

5.2.5.1. Evaluation of the possible cytotoxic effect of dLDHaHtSC particles

First, a commercially available apoptosis/necrosis detection kit was used to determine the cytocompatibility of the dLDHaHtSC particles.[190] The HeLa cells were pre-treated with dLDHaHtSC (20 mg/L, 37 °C), and fluorescent dyes to label the healthy and injured cells. In the kit, healthy cells are labelled with CytoCalcein Violet 450, apoptotic cells are characterized by the DNA binding 7-AAD, while necrosis is detected by Apopxin Green, a phosphatidyl serin binding dye that is translocated to the outer membrane during apoptosis. Confocal microscopy images (Figure 25 (A)) revealed no cytotoxic effect on HeLa cells, the dLDHaHtSC treated cells (similar to the control measurements) appeared in blue color, indicating the presence of healthy cells. The bar graph in Figure 25 (B) represents the normalized fluorescence intensity of apoptotic and necrotic/late apoptotic cells in relation to the intensity of the living cells. Based on the data obtained, the number of apoptotic and necrotic/late apoptotic cells was negligible compared to the healthy cells. It can be concluded that dLDHaHtSC did not show any cytotoxic effect on HeLa cells in the applied concentration regime.

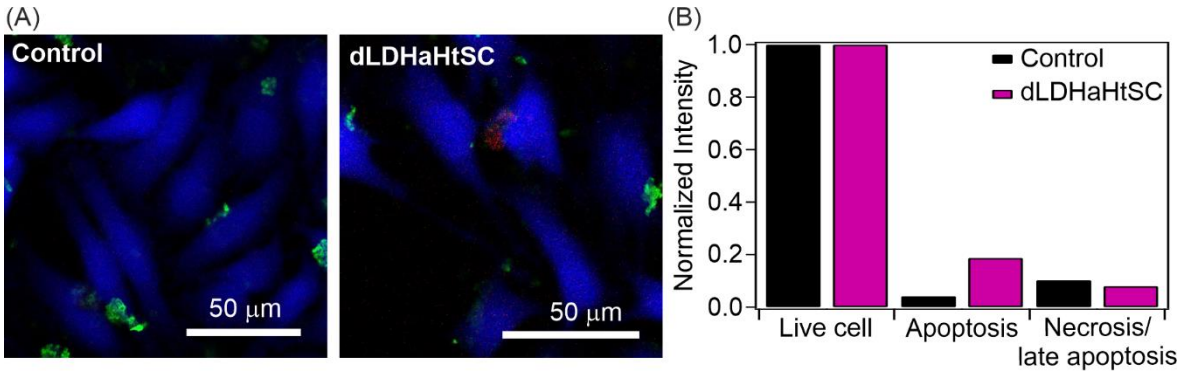

Figure 25. Confocal microscopy images (A) and normalized fluorescence intensity values (B) derived from cell viability assay.[181]

5.2.5.2. Enzyme adsorption and cell penetration ability

In the next step, dSTORM measurements were performed to (I) determine the size of the dLDHaHtSC particles and (II) assess the cell penetration ability of the enzyme-mimicking composite (Figure 26). Due to the small number of commercially available

antibodies, dual labelling was applied for the detection of dLDHaHtSC particles through HRP/SOD and HRP/CAT pairs. To assess the spatial distribution of dLDHaHtSC, the particles were first fixed on a glass substrate. The colocalizing clusters of fluorophores formed by the labelled enzymes immobilized on the particle surface were approximately 150 – 180 nm in lateral dimension. This size was in good agreement with the formerly determined hydrodynamic radii of the particles (Table 2).

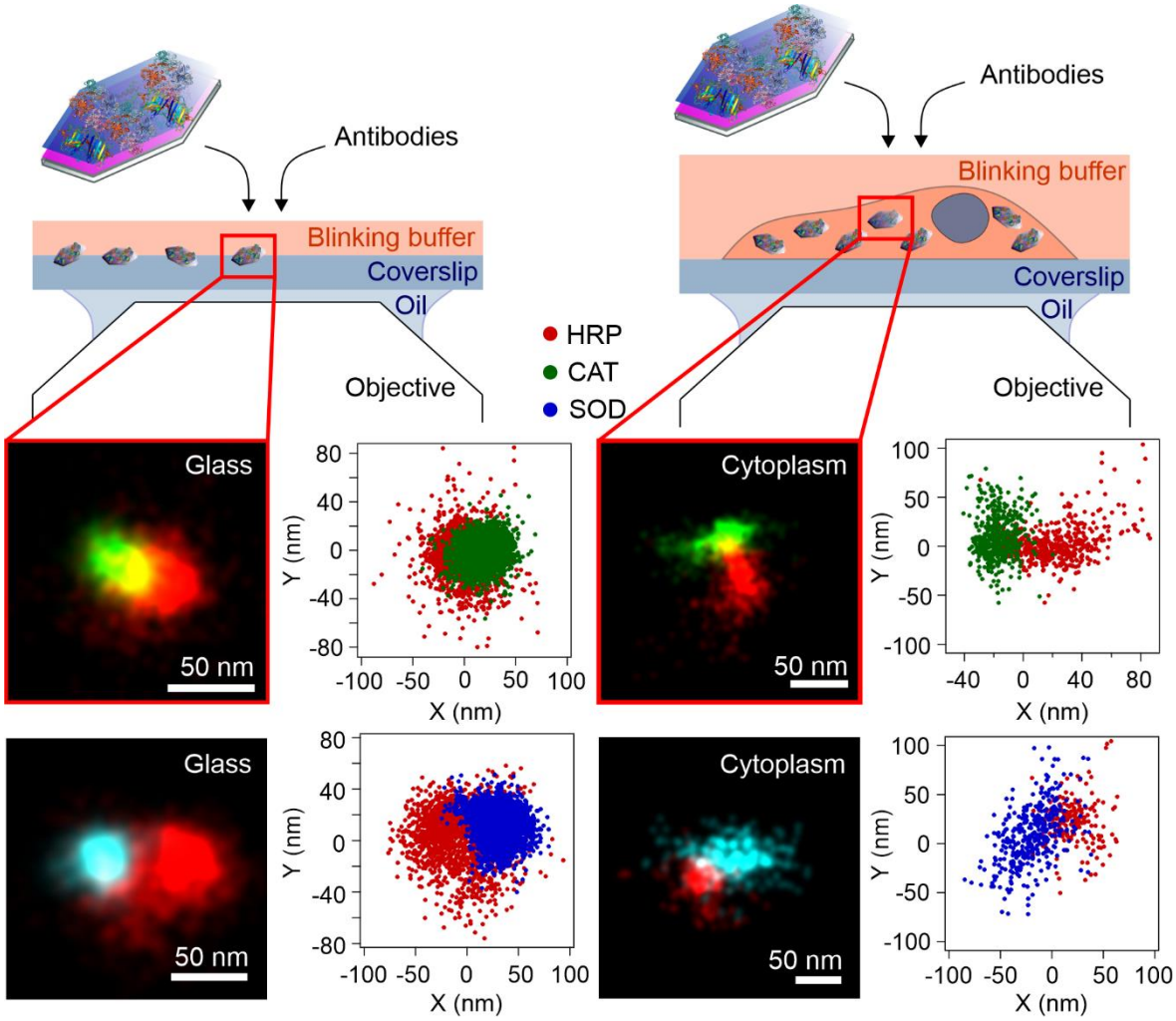

Figure 26. dSTORM images of the fluorescently labelled particles immobilized on glass (left) and in the intracellular matrix (right). The blinking events of the fluorophores were captured on an X-Y nanometer scale.[181]

After the visualization of the enzyme-coated particles, the next step was to investigate the cell penetration ability of the particles. The HeLa cells were treated with the dLDHaHtSC nanoparticle dispersion at a concentration of 20 mg/L (30 minutes, 37 °C). Imaging was then performed in the perinuclear/cytoplasmic region in total internal reflection fluorescence (TIRF) mode (Figure 26). The resulting clusters formed in the intracellular matrix were identical to those captured on the glass surface. These results indicate that dLDHaHtSC

nanoparticles can penetrate trough the cell membrane without triggering any detectable damage. Moreover, the cellular uptake did not cause any alteration of the particles.

5.2.5.3. Intracellular ROS scavenging and DNA double strand break inhibition

The results of chemical test reactions indicated promising antioxidant activity, nevertheless, the main question raised whether the composite is able to restore the normal antioxidant ROS balance in the cellular environment. Similar to the former cellular measurements, HeLa cells were treated with 20 mg/L dLDHaHtSC and also with the ROS indicator 2',7'-dichlorodihydro-fluorescein diacetate (H_2DCFDA). Intracellular ROS production was induced by incubating the cells with menadione, a commercially available ROS generating molecule,[191] and the fluorescence intensity was measured as a function of time (Figure 27).

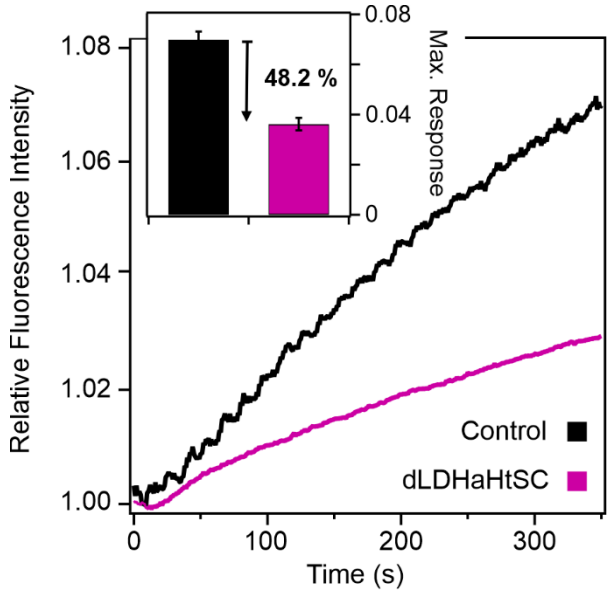

Figure 27. Intracellular ROS scavenging activity as determined by the change in relative fluorescence intensity over time for dLDHaHtSC treated (pink) and untreated (black) cells. The inset shows the maximum response for treated and untreated cells.[181]

In control cells (not treated with dLDHaHtSC), oxidation of H_2DCFDA occurred rapidly, resulting in a steep increase in fluorescence intensity after triggering ROS production with menadione. In contrast, the maximum fluorescence intensity decreased significantly (by 48.2 %) when the cells were pre-treated with the dLDHaHtSC composite. This decrease suggested the ability of the dLDHaHtSC particles to scavenge ROS remarkably.

As a proof-of-concept measurement, the inhibitory activity of the particles against oxidative stress induced DNA damage was tested. Such a harmful process can be readily detected by labelling the γH2AX histone protein, formed when H2AX is phosphorylated at serine 139.[192, 193] Therefore, the formation and determination of γH2AX foci is a potential method for the detection and quantification of ROS induced DNA damage. Foci refers to a large nuclear domain composed of DNA double strand break (DSB) signaling and repair factors.[194] Figure 28 shows the control (-/-), the H_2O_2 treated (+/-) and the (H_2O_2 and dLDHaHtSC) treated (+/+) cells and foci intensities/numbers.

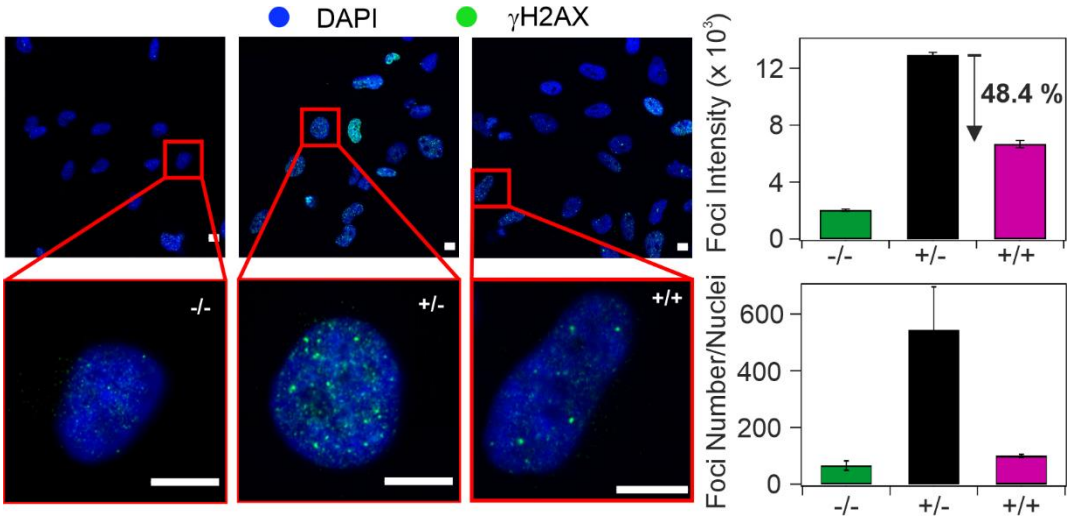

Figure 28. Detection of DNA double strand breaks by labelling γH2AX histone protein in dLDHaHtSC treated and untreated cells. The scale bars represent 10 μm. The (-) and (+) signs in the bar graphs represent the absence and presence of H_2O_2 and dLDHaHtSC: -/- none, +/- (H_2O_2) and +/+ (H_2O_2 and dLDHaHtSC).[181]

Control cells did not show significant fluorescence intensity from the formation of γH2AX. However, after the cells were treated with 50 μM H_2O_2 for 40 minutes, a significant increase in foci intensity and in the foci number/nuclei due to the formation of DSBs was observed. In contrast, dLDHaHtSC pre-treated (+/+) cells showed steep decrease in intensity and number of foci compared to (+/-) treated cells. Foci intensity decreased by 48.4%, while the foci number decreased to the control level, which indicated that dLDHaHtSC was not just capable of decreasing DSB formation, but also of restoring the normal intracellular ROS-antioxidant balance under oxidative stress conditions. Therefore, it was concluded that dLDHaHtSC was able to protect cells from ROS induced oxidative stress, thus from oxidative molecular damage, like DSB.

5.3. LDH-based antioxidant composites by immobilizing molecular antioxidants

The aim of this chapter was to co-immobilize two antioxidant molecules in/on LDH by adsorption and coprecipitation method. While TA was adsorbed on the outer surface of the LDH particles in both methods, GSH intercalated among the layers during coprecipitation and attached on the surface during adsorption. The structure of the particles was analyzed using a wide range of instrumentation, while their activity was revealed in the DPPH radical scavenging assay.

5.3.1. Immobilization of TA and GSH on/in LDH particles

The structure and morphology of the LDH/AO composites (adsorption method: LDH/TA/a, LDH/GSH/a and coprecipitation method: LDH/TA/c, LDH/GSH/c) were investigated in XRD and SEM measurements, respectively (Figure 29).

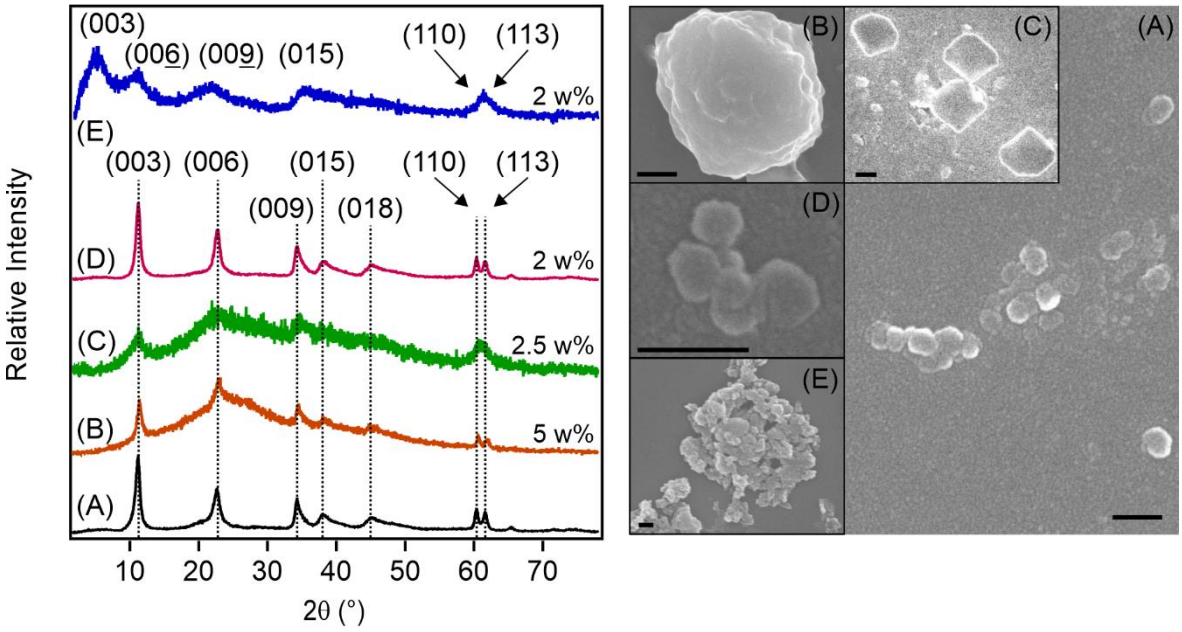

Figure 29. X-ray diffractograms (left) and SEM images (right) of LDH (A), LDH/TA/a (B), LDH/TA/c (C), LDH/GSH/a (D) and LDH/GSH/c (E). The Miller indices are labelled on the diffractograms, while the w% refers to the antioxidant content. The scale bars on the SEM images represents 200 nm.[164]

The diffractogram of the LDH host material showed the characteristic reflections of LDHs and these were labelled with *00l*, *01l* and *11l* Miller indices, which were analogous to that of other nitrate containing LDH particles.[195] The basal spacing calculated from Bragg's law (Eq. 18.) was d_{003} = 0.890 nm, in good agreement with the distance caused by the interlayer hydrated nitrate ions. For LDH/TA/a, LDH/TA/c and LDH/GSH/a, no significant change in the position of the (003), (006) and (009) Miller indices was observed indicating

that intercalation of antioxidant molecules did not occur in these cases. In contrast, a large shift was observed in the (003) Miller index for LDH/GSH/c, resulting d_{003} = 1.54 nm interlayer space. This large expansion of the basal spacing (compared to d_{003} = 0.890 nm for LDH particles) is in line with the intercalation of GSH molecules among the LDH layers. The higher noise-to-signal ratio for LDH/TA/a and LDH/TA/c samples were a sign of lower crystallinity of the sample, however, the characteristic reflections of LDH were still seen in the diffractograms indicating the formation of an ordered LDH structure. It was also found that a TA concentration higher than 0.01 M could not be applied during LDH synthesis, as it could inhibit the nucleation of LDH particles. This phenomenon is disadvantageous for the formation of an ordered lamellar LDH structure. Instead, an amorphous material was formed (Figure S7).

TG-MS measurements were performed to determine the amount of organic molecules in all cases confirming the immobilization of the antioxidants in/on the LDH particles. The organic contents, expressed in mass percentages, are indicated in the corresponding diffractograms (Figure 29 left). Due to the different molecular masses and the number of functional groups of TA, a significant variation in mass percentage was observed between the samples. The highest antioxidant content was found for LDH/TA/a, with 5 wt%.

The morphology of the composites were studied by SEM (Figure 29 right). The average diameter of the LDH particles was (111 ± 17) nm, while (115 ± 15) nm and (609 ± 227) nm was determined for LDH/GSH/a and LDH/TA/c, respectively. The bare LDH particles and these two composites showed a similar, plate-like morphology, whereas LDH/GSH/c and LDH/TA/a formed large aggregates. For the latter two samples, SEM was not suitable to identify any well-defined dimension. The aggregates of these particles formed a sphere-like shape which is in contrast to the other composites.

5.3.2. Structural investigation of LDH/AO composites

To further confirm the immobilization of the antioxidants in/on the LDH substrate support and to determine the change in their structure and conformation, IR, Raman and UV-VIS-NIR spectroscopy measurements were introduced.

5.3.2.1. Vibrational spectroscopy study of LDH/TA

Only one intense band at 1356 cm^{-1} related to the stretching vibration of the NO_3^- groups was identified in the bare LDH and in all LDH/TA spectra (Figure 30).[94] For a proper

interpretation, IR measurements of the native and the NaOH treated TA were also recorded (Figure 30 (B) and (C), respectively). The IR bands and assignments related to the TA containing samples are shown in Table S1.

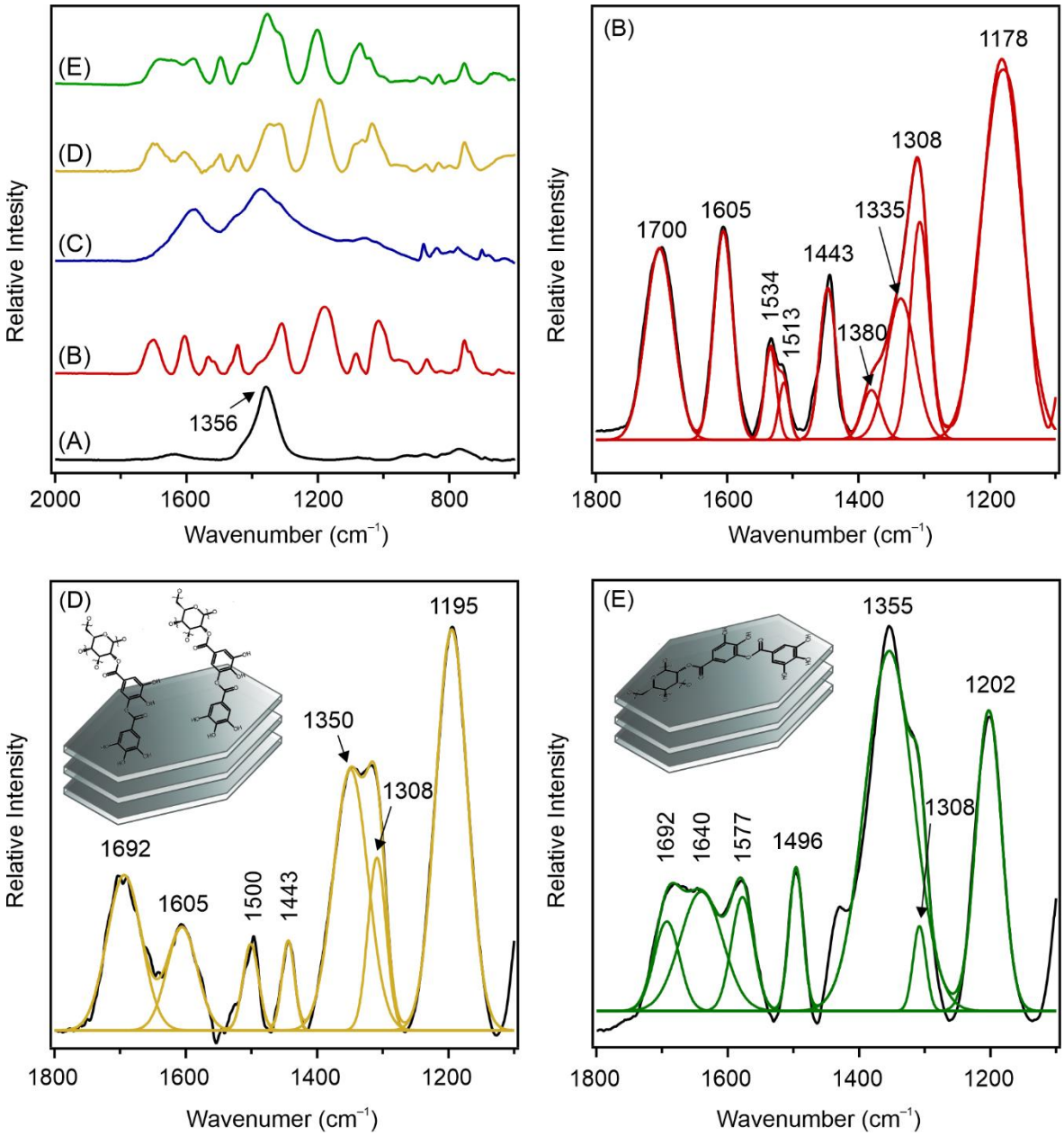

Figure 30. Measured and deconvoluted IR spectra of LDH (A), TA (B), TA/NaOH (C), LDH/TA/a (D) and LDH/TA/c (E).[164]

A significant change was observed between the spectra of untreated and NaOH treated TA, indicating that TA underwent a major structural change as a result of the alkaline treatment. The spectrum of the original TA showed strong bands at 1700 cm^{-1} and 1178 cm^{-1}, which were related to the stretching vibration of the carbonyl (C=O) and C–H groups, respectively. [196] Three bands were corresponded to the bending vibrations of phenolic groups

at 1308 cm^{-1}, 1335 cm^{-1} and 1380 cm^{-1},[196] while the broad band at 1443 cm^{-1} was identified as the bending mode vibration of the surface hydroxyl groups of TA.[197, 198] The bands located at 1605 cm^{-1}, 1534 cm^{-1} and 1513 cm^{-1} were assigned to the stretching mode vibrations of the C=C bonds in the aromatic ring.[197, 198]

From TG-MS measurements, it was revealed that the synthesis method quantitatively affected the antioxidant content of the samples, whereas the IR measurements shed light on the qualitative effects during the preparation of the LDH/TA composite. The IR data demonstrated that TA was deposited in its original form on the LDH surface, therefore, LDH protected the antioxidant molecule from the alkaline treatment induced structural damage.

In addition, the significant difference in band positions can be attributed to the different orientation of TA on the LDH surface upon variation of the synthetic procedure.[199] For LDH/TA/c, shifts in the bands related to the hydroxyl groups (1443 cm^{-1} → 1496 cm^{-1}) and C=C bonds (1513 cm^{-1} → 1640 cm^{-1}, 1577 cm^{-1}) of the aromatic rings were observed. Since these bands are polarized in the direction of the molecular backbone, they can be applied as an indicator for the orientation of TA on the LDH surface. These large shifts that occurred due to coprecipitation method suggested that TA was orientated parallel to the surface.[199] Therefore, the vibrations of the aromatic ring and hydroxyl groups are more hindered, because they have formed electrostatic interactions and hydrogen bonds with the particle surface. However, the bands related to LDH/TA/a did not show significant change compared to the literature values,[196] indicating, that the TA orientation upon adsorption was perpendicular to the surface. In this case, the vibrations of the functional groups and molecular backbone of TA were not affected by the LDH surface and thus, the position of the bands was similar to the native antioxidant.

Based on the results detailed above, the assembly mode of TA can be adjusted by the synthesis method. The different orientations of TA on the LDH surface may be derived from the different pH in the synthesis routes. In the adsorption method, the pH was not set, therefore most of the hydroxyl groups of TA remained protonated, resulting in a low negative charge density of TA. Due to this structural property, the repulsion between the particle surface and the hydrophobic aromatic rings of TA was more dominant and hence, TA orientated as far away from the surface as possible and positioned perpendicularly to the surface. Contrary, at pH 10 (which was set during coprecipitation method), most of the hydroxyl groups of TA were in deprotonated form, so the net negative surface charge of TA was higher than in its original (protonated) form.[200] Therefore, the electrostatic interaction

between the particles and TA became more favorable, the antioxidant compound oriented parallel to the surface.

Raman measurements further confirmed the difference in the adsorption mode of TA on the LDH surface (Figure 31).[201] The detailed band assignments are shown in Table S2. The Raman band in the TA spectrum at 1612 cm^{-1} is related to the stretching vibration of the C=C bond positioned in the aromatic ring. For LDH/TA/c, a large shift in the location of this band was observed, which also possessed that TA attached to the LDH surface with its aromatic rings parallel to the surface, hindering the vibration derived from the aromatic backbone. However, when TA was adsorbed in perpendicular way (LDH/TA/a), the aromatic ring vibration was not obstructed, as it was also mentioned during discussion of IR results.

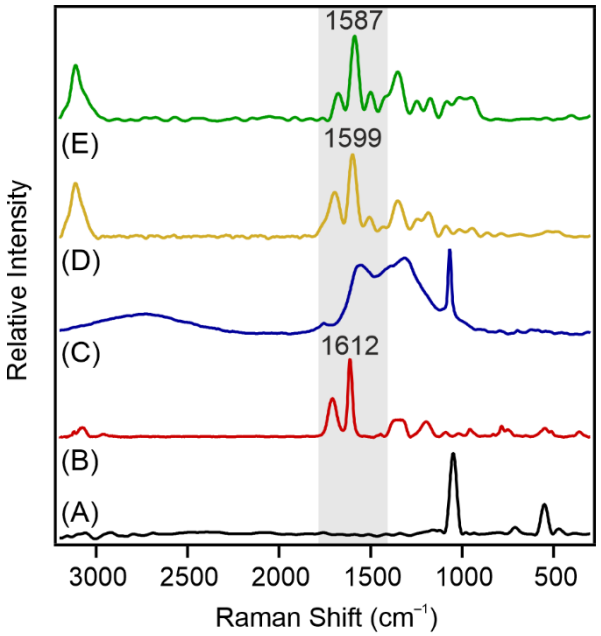

Figure 31. Raman spectra of LDH (A), TA (B), TA/NaOH (C), LDH/TA/a (D) and LDH/TA/c (E). The grey shadow represents the shift of the 1612 cm^{-1} band, which is related to the stretching vibration of the C=C bond in the aromatic ring.[164]

5.3.2.2. Vibrational spectroscopy study of LDH/GSH

IR and Raman measurements carried out for GSH containing samples also revealed that the synthetic routes have a significant impact on the GSH incorporation in/on LDH particles. The IR spectra of the GSH containing samples are shown in Figure 32, while all peaks and their detailed assignments can be found in Table S3. The peak related to the interlayer NO_3^- ions was detected in LDH/GSH/a as in the TA containing samples, indicating that GSH adsorption on the outer surface did not affect the interlayer gallery of LDH particles.

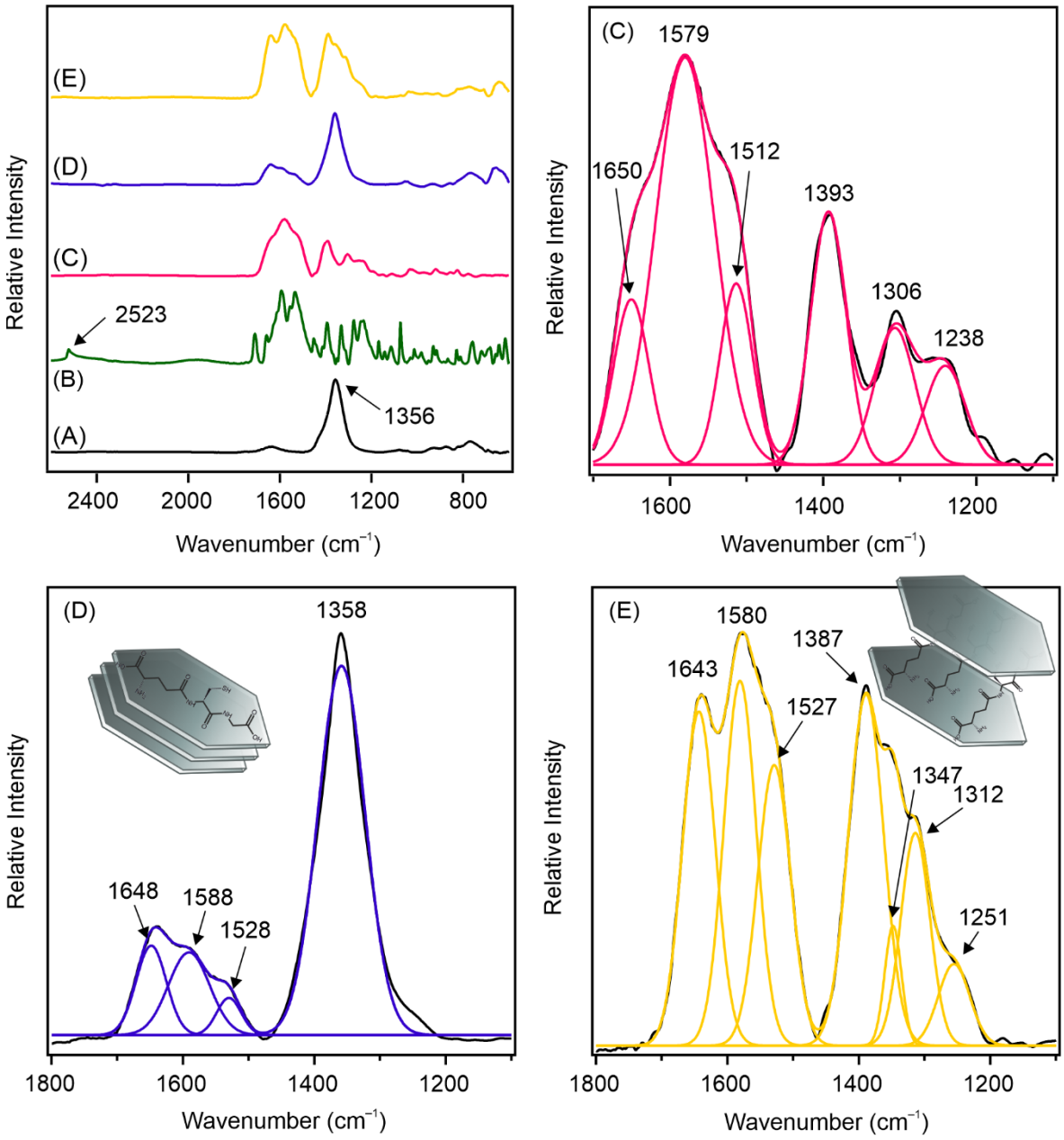

Figure 32. Recorded and deconvoluted IR spectra of LDH (A), GSH (B), GSH/NaOH (C), LDH/GSH/a (D) and LDH/GSH/c (E).[164]

The alkaline treatment induced the formation of the sodium salt of GSH, however, no structural decomposition was observed. The IR spectra of free GSH and LDH/GSH/a showed that no chemical (e.g., deprotonation) or structural (e.g., break of chemical bonds) change of GSH occurred during adsorption on the outer surface of the LDH particles. Beside the peak of the above mentioned interlamellar NO_3^- anions, the spectrum of the composite included the characteristic peaks of GSH (Amide I: 1658 cm^{-1} and Amide II: 1533 cm^{-1}) without any significant shifts. In contrast to TA, GSH intercalated in its sodium salt, formed in alkaline condition, among the layers. In addition to the appearance of the characteristic peaks of the sodium salt of GSH (Amide III: 1306 cm^{-1} and Amide IV: 1238 cm^{-1}), the shift

in the position of these peaks and the significant decrease of the peak intensity related to the interlayer NO_3^- also reinforced the intercalation of the antioxidant.[19] This is in line with the XRD measurements, where the increased basal spacing confirmed the intercalation of the GSH molecule among the layers. Note that the appearance of the peak related to the stretching vibration of the -SH group (2523 cm^{-1}) referred to the deprotonation of the thiol groups in both the adsorption and coprecipitation methods.

Raman measurements indicated similar immobilization features as discussed in IR measurements (Figure S8). The results also confirmed the intercalation of the anionic form of GSH in LDH/GSH/c, while the absence of the band related to the -SH group (~2500 cm^{-1}) revealed that the thiol group was deprotonated during both adsorption and coprecipitation methods.[202]

Further investigations revealed other interesting features. Such as the Raman spectra of LDH/GSH/a and LDH/GSH/c contained significant differences in the spectral range of 700 – 200 cm^{-1} (Figure 33).

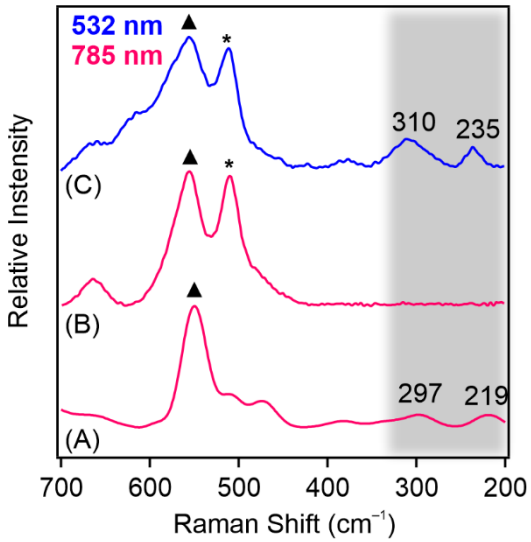

Figure 33. Raman spectra of LDH/GSH/a (A) and LDH/GSH/c (785 nm (B) and 532 nm (C)).[164]

Namely, a broad band at 510 cm^{-1} (marked with a black star in Figure 33) was identified in the spectrum of LDH/GSH/c, which was related to the stretching vibration mode of the disulfide bond (S–S).[203] This band could not be recognized in the spectrum of LDH/GSH/a, however, the peak assigned to the C–S group (labelled with a black triangle) remained unchanged. These results raised the question whether the GSSG completely replaced the original form of the antioxidant. To address this question, a laser source of 532 nm instead of 785 nm was used, which was able to excite the thiolate groups located on the

outer surface of the LDH particles. The peaks at 310 cm^{-1} and 235 cm^{-1} appeared in the LDH/GSH/c spectrum at the excitation wavelength of 532 nm, confirmed the presence of the thiolate groups, so that the antioxidant was attached in two forms in/on the LDH particles, in the original GSH and in the dimerized GSSG forms.[204, 205] Based on the XRD results, the expansion of the basal spacing indicated, that GSH is intercalated in the interlayer gallery, while GSSG (due to its larger size) was adsorbed on the outer particle surface. The detailed assignments of Raman bands are shown in Table S4.

5.3.2.3. UV-VIS-NIR spectroscopy study of LDH/TA and LDH/GSH

The structure of the antioxidant loaded samples was also investigated by UV-VIS-NIR spectroscopy. The spectra, divided into three regions (UV-VIS: 200 – 500 nm, NIR: 1350 – 1700 nm and 1050 – 1350 nm), are shown in Figure 34. The intense peak in the range of 1350 – 1700 nm is related to the overtone of the stretching mode vibration of hydroxyl groups.[206-208] The large shift observed for antioxidant loaded samples resulted from the change in polarity of the samples after the AO attachment.[209] It was more significant for TA containing samples, which was related to the interaction between the TA and the surface –OH groups of the LDH particles. In the 1050 – 1350 nm region, two characteristic peaks were observed for LDH particles, which were assigned to the first overtone of the hydroxyl symmetric stretching mode vibration and the combination bands of the "free water".[210] The variation of peak intensities in this range was strongly connected to the amount of water adsorbed on the surface. Therefore, the intensity of these peaks decreased significantly in those samples, where adsorption was more dominant, compared to the bare LDH and LDH/GSH/c systems. However, the most intense change was detected in the UV-VIS region (200 – 500 nm), where no significant peak was detected for LDH particles, but the AO loaded samples showed a remarkable deviation from the spectrum of the host material, which needs further explanation. First, a new peak appeared around 270 nm for the GSH loaded samples, which was related to the GSH molecules.[211] Moreover, an additional peak appeared at 213 nm in the LDH/GSH/c spectrum, which can be assigned as the absorption maximum of the GSSG molecule.[212] This observation further confirmed the finding of Raman measurements that the LDH/GSH/c composites contain GSH and also its disulfide form (GSSG) on the LDH surface. Note that these peaks are slightly shifted compared to those found in the literature. [211, 212] For LDH/TA/a and LDH/TA/c, the peaks at 267 nm and

294 nm, respectively, were assigned to the absorption maximum of TA, but they are slightly shifted compared to the literature value of 278 nm.[213]

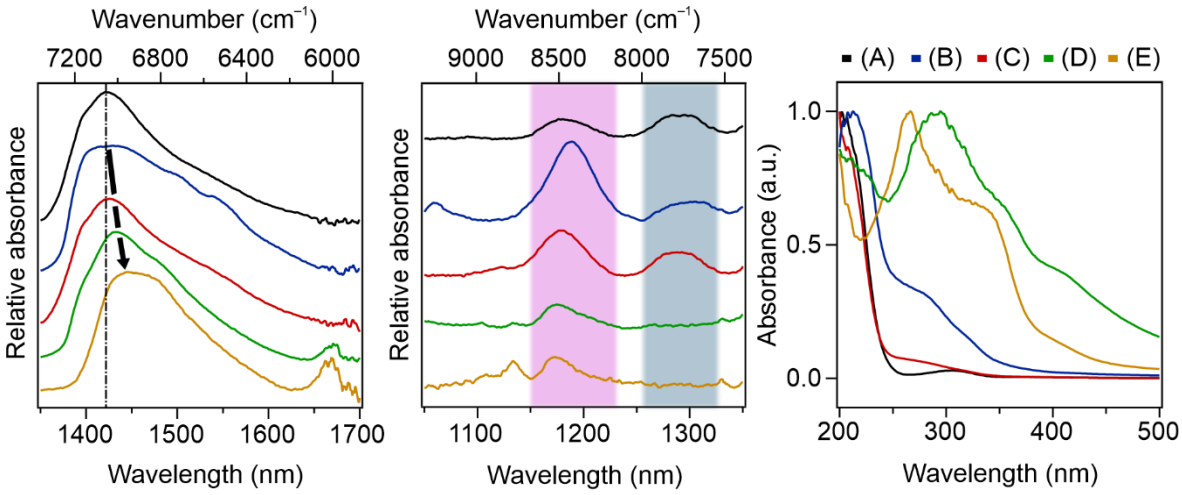

Figure 34. UV-VIS-NIR spectra of LDH (A), LDH/GSH/c (B), LDH/GSH/a (C), LDH/TA/c (D) and LDH/TA/a (E). The arrow represents the shift of the peak in the 1350 – 1700 nm region, while the pink and grey shadows show the change in peak intensity in the 1050 – 1350 nm range.[164]

To summarize, the UV-VIS-NIR measurements further confirmed the presence of organic molecules in the composites, however, did not provide clear evidence for the position of the antioxidants on the LDH particles. Based on these results, it was assumed that GSSG was adsorbed in a significant amount on the outer surface of the LDH particles, however, this issue should be further studied in detail.

5.3.3. Antioxidant activity of LDH/AO composites

To determine the antioxidant activity, the native antioxidants and the composites were tested in the DPPH assay, in which a stable radical is reduced by the antioxidants present in the reaction mixture, while the color changes from purple to yellow.

First, the TA and TA loaded samples were tested in the radical scavenging assay (Figure 35 left). The results clearly showed that the TA immobilized by adsorption (LDH/TA/a) kept its activity, which even increased slightly. In contrast, the radical scavenging ability of the LDH/TA/c decreased significantly, the amount of radical remaining in the reaction mixture did not reach 50 %, and indeed it did not decrease below 80 %. These results pointed to the relation between the TA orientation on the LDH surface and the radical scavenging activity. Namely, in a perpendicular orientation, the phenolic hydroxyl groups of the TA bind the radicals, therefore it showed higher antioxidant activity. Contrary, when the TA molecules were orientated parallel to the surface, the active phenolic groups were

available in a reduced number for the radicals, therefore the reaction between them could not take place. The increased activity for LDH/TA/a compared to the native TA is explained with the presence of the LDH particles in the solution. Namely, the radicals can be readily adsorbed on the particle surface and therefore, more of them reach antioxidant molecules than in solution. By investigating the durability of the antioxidant activity, it was found, that no change occurred in the scavenging activity of TA and LDH/TA/a after 1 month. The EC_{50} values are summarized in Table 4.

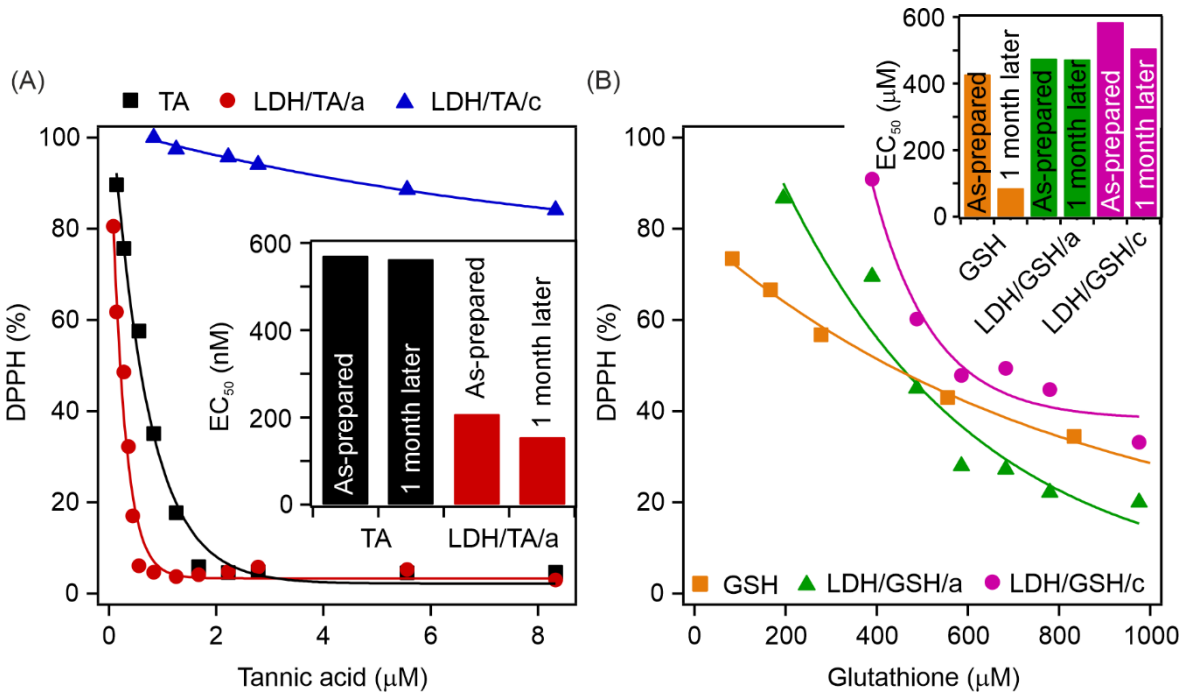

Figure 35. Results of the DPPH assay performed for TA (A) and GSH (B) loaded samples. The insets show the EC_{50} values of the as-prepared and 1 month old samples.[164]

No significant change was observed for GSH containing samples after immobilization, i.e., the radical scavenging activity of LDH/GSH/a and LDH/GSH/c was similar to that of GSH (Figure 35 right). This finding was in good agreement with previous studies in which the antioxidants maintained their activity upon immobilization on a host material. Results of the durability tests indicated that the activity of free GSH increased steeply after 1 month, while no change was detected for the LDH/GSH/a and LDH/GSH/c samples. It has already been shown that GSH suffers structural deformation in this time frame,[214] therefore, the products of such a decomposition could be also involved in the scavenge of DPPH. The smaller and more hydrophobic molecules have more accessible thiol groups and can therefore act as more efficient antioxidants than GSH. Nevertheless, the exact amount or ratio of the decomposed and original form of GSH is difficult to define and thus, its larger scale application is complicated.[215] In contrast, LDH/GSH/a and LDH/GSH/c kept

their activity after 1 month. The host material contributed to preserving GSH without structural changes, namely LDH provided structural stability to the antioxidant molecule.

Table 4. EC_{50} values of the molecular antioxidants in bare and immobilized forms.

Sample	EC_{50} (μM)[a]	EC_{50} (μM) 1 month later[b]
TA	0.571	563
LDH/TA/a	0.208	155
LDH/TA/c	N.A.	N.A.
GSH	428	86
LDH/GSH/a	475	473
LDH/GSH/c	585	506

[a]EC_{50} values determined from the DPPH(%) vs AO concentration plots. [b]EC_{50} values determined after 1 month storage of AO solutions and LDH/AO composites. The average error calculated for the DPPH assay is within 5%.

5.3.4. Examination of the recyclability feature of LDH/TA/a

The IR and Raman measurements were repeated after the radical scavenging test (Figure S9 and Figure S10, respectively) to reveal the possible structural changes after the reaction with the DPPH radical. The spectra showed no significant change in the structure of the antioxidants, indicating that the structure of antioxidants did not change upon the reaction. Based on these results, the most active component (LDH/TA/a) was selected to perform the recyclability test (Figure 36).

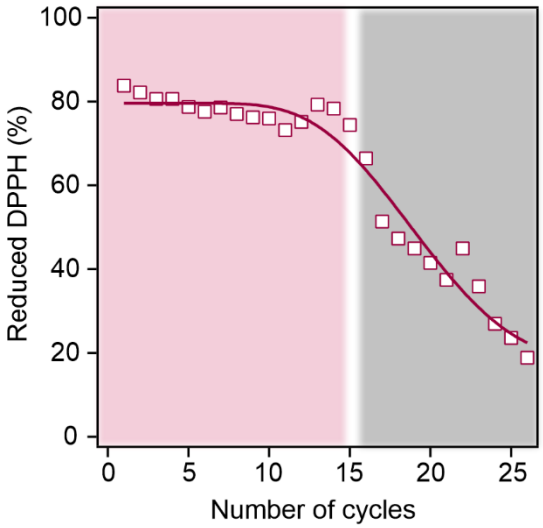

Figure 36. Reduced amount of DPPH as a function of the number of cycles in the recycling test of LDH/TA/a.[164]

The reduced DPPH (%) (calculated by the Eq. 15.) was plotted against the number of cycles and the tendency in the data clearly showed that no change in activity was detected

until the 15th cycle. The decrease after this cycle meant that the composite started to lose its activity, which decreased below 20 % finally. However, these data emphasized on the superior reusability of LDH/TA/a, which is an important parameter in many applications.

5.4. Copper(II) incorporated LDH nanozymes against intracellular ROS production

The aim of this study was to produce Cu(II)-containing LDH nanozymes by partially replacing Mg(II) ions with Cu(II) ions in the LDH layers. The structural properties of the nanozymes were comprehensively investigated, while their radical scavenging feature was determined first in chemical tests, then in intracellular assays.

5.4.1. Structural and morphological characterization

The incorporation of copper(II) ions was confirmed with various techniques. The LDH structure was revealed by XRD measurements. The diffractograms of Mg_3Al (MA), $Mg_{2.8}Cu_{0.2}Al$ (CMA1), $Mg_{2.6}Cu_{0.4}Al$ (CMA2), and $Mg_{2.4}Cu_{0.6}Al$ (CMA3) LDHs are shown in Figure 37 (A).

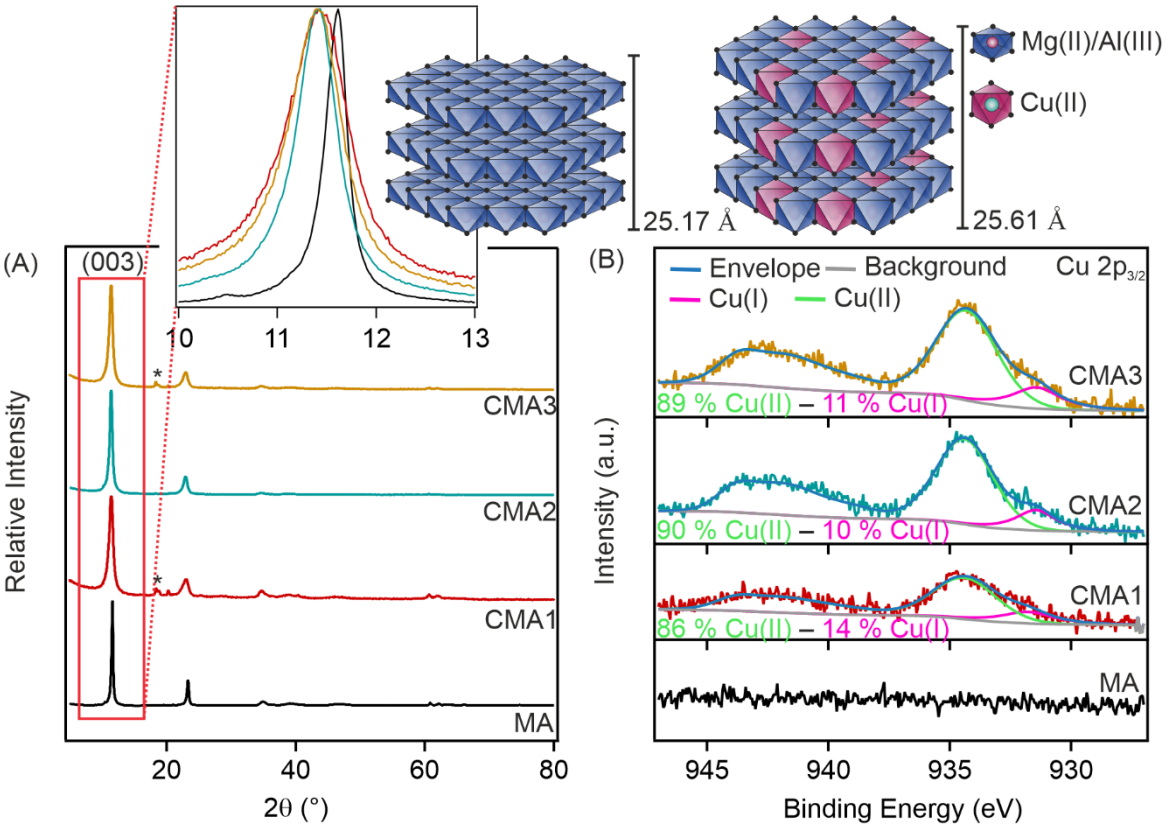

Figure 37. XRD pattern (A) and XPS spectra (B) of MA, CMA1-3 samples (A). The inset in the XRD graph shows the 003 reflection, while the scheme on the top of the figure represents the partial replacement of Mg(II) ions by Cu(II) ions, causing an increase in the *c* value.

The diffractograms of MA and CMA1-3 samples were characteristic for the LDH structure,[195] however, a slight shift was observed in the first (003) reflection. Calculation of the crystal parameters (Table 5.) revealed that the basal spacing (*d*) and the *c* value increased slightly.

Table 5. Crystal parameters, size and charge data of MA and CMA samples.

Sample	2θ(003) (°)[a]	d(003) (Å)[b]	c (Å)[c]	D_h (nm)[d]	PDI[e]	ζ (mV)[f]
MA	11.6	8.39	25.17	77.1 ± 5.2	0.214	32.1 ± 2.2
CMA1	11.4	8.54	25.61	84.8 ±0.1	0.241	31.0 ± 0.8
CMA2	11.4	8.54	25.61	82.9 ±0.2	0.229	28.4 ± 1.1
CMA3	11.4	8.54	25.61	89.4 ±0.7	0.237	32.3 ± 0.4

[a]2θ value corresponds to the (003) Miller index. [b]The basal spacing was calculated by the Eq. 18. [c]The *c* crystal parameter was calculated by the Eq. 19. [d]Hydrodynamic diameters were measured at 1mM NaCl concentration. [e]PDI is the polydispersity index determined by DLS measurement in stable colloids. [f]ζ is the zeta potential measured at 1 mM NaCl concentration.

This deviation from the structure of the original MA sample could be due to the partial replacement of Mg(II) ions by Cu(II) ions. In addition, the Jahn-Teller effect, and the higher electronegativity of the Cu(II) ions could also cause distortion of the LDH structure.[216] The appearance of the reflection marked with an asterisk (*) in the diffractograms indicated the presence of a small amount of $Mg(OH)_2$, which could be formed from the released Mg(II) ions that were replaced by Cu(II) ions. The schematic representation of the cation substitution is shown above the graphs in Figure 37, with the *c* parameter values indicated beside the schemes.

The particle sizes determined in DLS measurements are listed in Table 5. The hydrodynamic diameters were below 100 nm in all cases, while the PDI was ~ 0.2, indicating a relatively narrow particle size distribution (Figure S11). The zeta potential values were approximately +30 mV for all samples, the Cu(II) incorporation did not significantly affect the particle charge.

The surface composition of the MA and CMA1-3 samples was further explored by XPS measurements. All sample surfaces contained Mg, Al, C, O and Cl, however, Cu was only slightly visible on the survey scans, which suggested that a low amount of copper(II) ions was incorporated into the LDH layers (Figure S12). Note that adventitious carbon (adsorbed on all sample surfaces) was used as an internal standard for charge referencing. Its main peak was set at 284.8 eV and used as a correction for all respective high resolution (HR) spectra. The presence of copper was confirmed with the HR scans (Figure 37 (B)) and the Cu satellites were perfectly fitted with 4 peaks corresponding to the $Cu(OH)_2$

compound.[217] The fitted binding energies are listed in Table S5. In addition to the total of 4 peaks, an additional peak was necessary to fit the low energy (931.75 eV) region, corresponding to Cu(I), which showed good agreement with the previously published copper containing LDHs.[218] It should be noted that the amount of Cu(I) is negligible compared to Cu(II). Based on the binding energies, only one chemical state could be identified for both Mg and Al on the sample surface (Figure S13). The peaks at 49.4 eV for Mg-OH and at 74.0 for Al-OH were identified, referring to Mg(II) and Al(III), respectively.[219] In addition, a large shift in binding energy in the Al 2p case was observed, indicating a change in the chemical environment that occurred due to copper incorporation (Table S6.). Based on the elemental composition of the surface (Table 6.) it can be stated that the amount of the inserted Cu(II) cations increased following a trend in line with the initial Cu(II) concentration.

Table 6. Surface elemental composition of MA and CMA1-3 samples determined by XPS.

Sample	*Mg* / at%	*Al* / at%	*Cu* / at%	Surface stochiometric ratio
MA	79.1	20.9	-	$Mg_{3.16}Al_{0.84}$
CMA1	73.9	24.3	1.8	$Mg_{2.96}Al_{0.97}Cu_{0.07}$
CMA2	73.9	23.7	2.3	$Mg_{2.96}Al_{0.95}Cu_{0.09}$
CMA3	71.8	24.7	3.5	$Mg_{2.87}Al_{0.99}Cu_{0.14}$

FLIM measurements also confirmed the change in LDH structure after copper incorporation (Figure 38 (A)). A double exponential model using the n-exponential reconvolution method was optimal to fit the control sample (MA), resulting in a long (6.15 ns) and a short (0.59 ns) component (inset in Figure 38 (B)). Contrary to this, copper containing samples should be fitted by a tri-exponential model. The two components (long and short lifetimes) were similar to those of the MA sample, however the third component became a very short (< 1 ns) one. Accordingly, the CMA1-3 distributions were refitted by fixing the two longer components, resulting in a third component of 0.1 ns for all three CMA samples, which corresponds to the response time of the FLIM system. This result implies that the real lifetime is even shorter, but it cannot be determined with the instrumentation used in the present study. The fluorescence property of the LDH particles was assigned to the surface defects,[220, 221] but the changes in the metal ion ratio in the LDH layers can also affect the fluorescence signal.[222] Therefore, the change in the number and position of the surface defects and the change in metal ion ratio after copper(II) incorporation can affect the fluorescence properties of the LDH nanoparticles and thus, the fluorescence lifetime of the CMA1-3 samples.

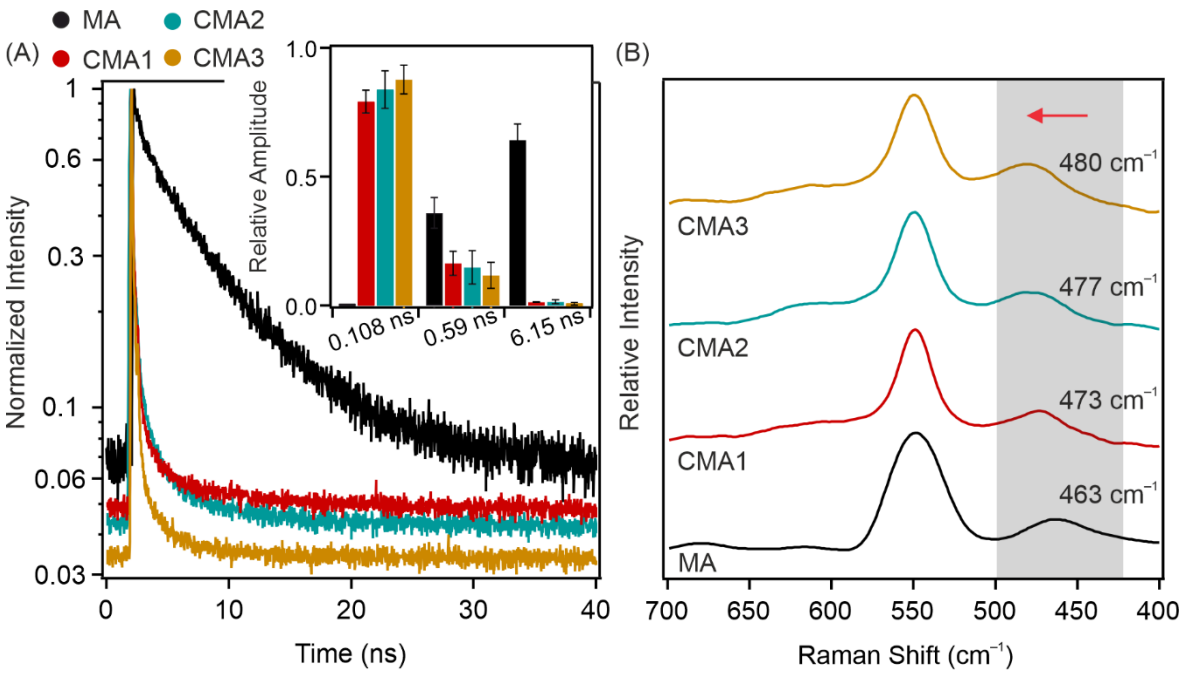

Figure 38. Normalized fluorescence intensity versus time (A) and Raman spectra in the range of 700 – 400 cm^{-1} range (B). The inset in figure (A) represents the relative amplitude value for different fluorescence lifetimes.

Raman measurement results also confirmed the change in LDH structure upon the incorporation of copper. The Raman bands at 549 cm^{-1} and 463 cm^{-1} were assigned to the symmetric stretching vibrations of Al-O and Mg-O, respectively.[223] A significant shift in the Mg-O band was observed, which could be derived from the partial replacement of Mg(II) ions by Cu(II) ions.[224] The Raman results therefore further strengthen the theory that the layer composition was affected by the incorporation of copper(II) ions.

5.4.2. Enzyme-like activity of CMA1-3 samples

The enzyme mimicking activity of CMA1-3 samples was investigated using the CAT and SOD assays. Regarding the results of the CAT assay, by increasing the nanozyme concentration, the remaining H_2O_2 in the reaction mixture decreased, indicating that the CMA samples were able to decompose H_2O_2 (Figure 39 (A)). The EC_{50} values were calculated from the lines fitted on the experimentally obtained data, which revealed that the CAT activity is not related with the copper content of the particles. All samples were able to decrease the remaining H_2O_2 (%) to ~20 %, which was similar to the native enzyme. However, the EC_{50} values of the CMA samples (Table 7) are significantly higher than that of the CAT enzyme (Table 3).

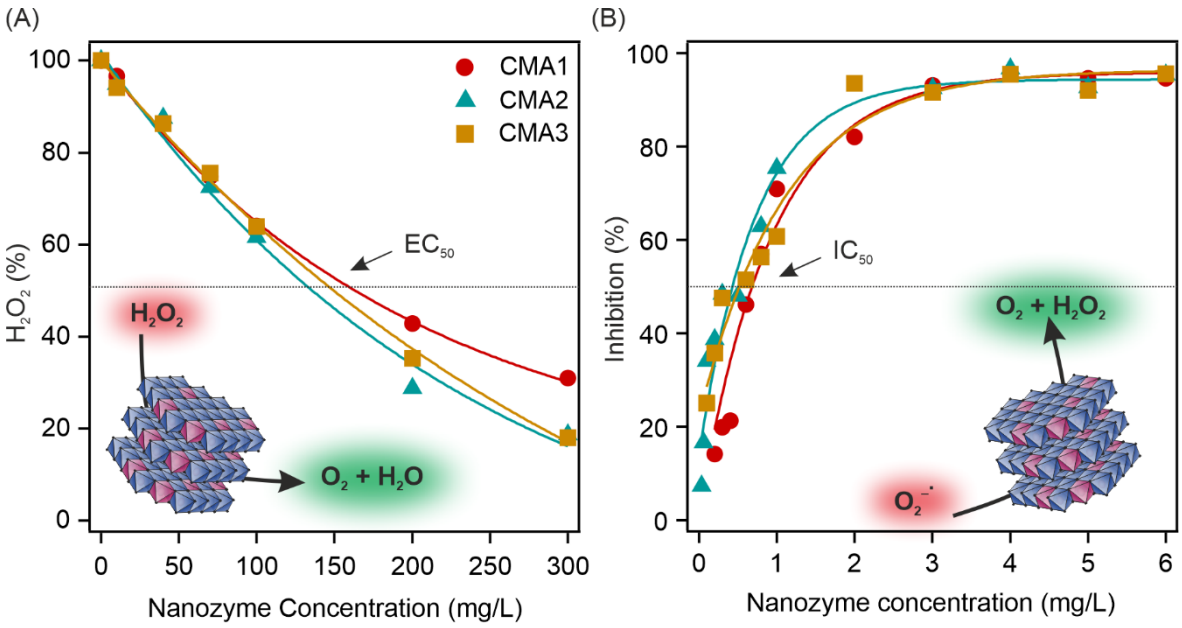

Figure 39. CAT (A) and SOD (B) activity of the CMA1-3 samples. The insets show the schematic representation of the reaction that occurred between the ROS molecules and the nanozyme.

In the SOD test, the superoxide radicals react with NBT followed by color change in the reaction mixture. Nanozymes with SOD activity can inhibit this reaction by decomposing the radicals and therefore, prevent the color change. When plotting the inhibition values against the nanozyme concentration (Figure 39 (B)), the IC_{50} values were calculated from the fitted line. Similar to the CAT assay, no significant change occurred by increasing the incorporated copper amount, the IC_{50} values did not differ significantly from each other, however they decreased compared to the SOD enzyme. In contrast to IC_{50}, I_{max} values remained similar to SOD; 3 mg/L nanozyme concentration the maximum efficiency is comparable to that of the native enzyme. It should be noted that MA did not show any activity in either the CAT or SOD assay.

Table 7. EC_{50} and IC_{50} values calculated based on the CAT and SOD assay.

Sample	EC_{50} (mg/L)[a]	IC_{50} (mg/L)[b]	I_{max} (%)[c]
MA	N/A[d]	N/A[d]	N/A[d]
CMA1	165	0.68	94.5 ± 1.2
CMA2	136	0.43	94.3 ± 2.1
CMA3	149	0.52	93.6 ±2.2

[a]EC_{50} values were calculated based on the plots in Figure 39 (A), while [b]IC_{50} values were determined from Figure 37 (B). The average error of the enzyme tests is within 10 %. [c]The plateau of the inhibition curves in the SOD assay. [d]N/A means, that the particle was inactive.

The findings of these measurements shed light on the fact that the Cu(II)-containing nanozymes can decompose ROS molecules without functionalization with any scavenger

molecules. Moreover, the nanozymes showed excellent enzyme mimicking characteristics compared to the examples found in the literature.[135, 225, 226]

5.4.3. Intracellular ROS scavenging activity of CMA samples

Proof-of-concept studies were performed to illustrate the intracellular ROS and $O_2^{-\bullet}$ scavenging activity of all three (CMA1-3) samples. First, the CMA samples were investigated in the 0.5 – 2.5 mg/L concentration range, where no significant change in overall intracellular ROS concentration was detected, while $O_2^{\bullet-}$ concentration slightly decreased (Figure S14). To further increase the activity, the tests were repeated by increasing nanozyme concentration. Significant changes in the normalized fluorescence intensities were detected in the concentration range of 5-20 mg/L (Figure 40 (A) and (B)). Although the CMA samples showed no significant difference in ROS scavenging ability, the 5 mg/L CMA3 sample exhibited the greatest $O_2^{\bullet-}$ dismutation feature, thus this sample and concentration was applied in the further measurements.

To assess the cytocompatibility of the samples, a CellTiter-Glo® assay was performed (Figure 40 (C) and Figure S15). This test is based on the ATP production ability of cells. Under normal physiological conditions, the cells produce ATP, which can be determined by fluorescent labelling. All treated cells were able to produce ATP and thus, the nanozyme treatment did not affect their viability, i.e., the nanozymes showed no cytotoxic effect over a wide concentration range. This further strengthened the selection of the 5 mg/L CMA3 sample.

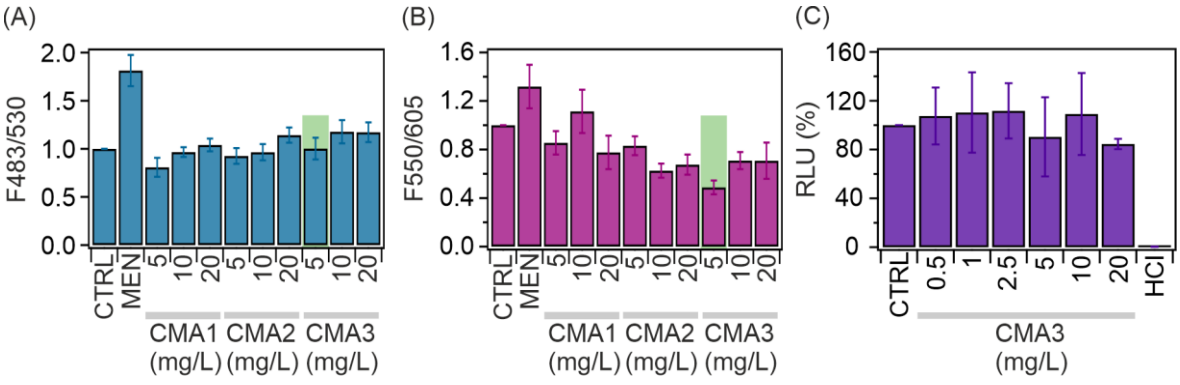

Figure 40. Intracellular ROS (A) and superoxide (B) scavenging activity of CMA samples in the 5 – 20 mg/L concentration range. Cell viability assay for CMA3 sample in the 0.5 – 20 mg/L concentration range (C) The green shadow represents the 5 mg/L CMA3 sample, selected for further measurements.

5.4.3.1. Cytocompatibility assay of CMA3 samples

To further evaluate the cytocompatibility of the CMA3 sample, microscopic visualization was performed using an apoptosis/necrosis assay (Figure 41). The detection kit functioned as previously described (*Chapter 5.2.5.1.*), and live, apoptotic and necrotic cells were accordingly labelled with different fluorescent dyes.

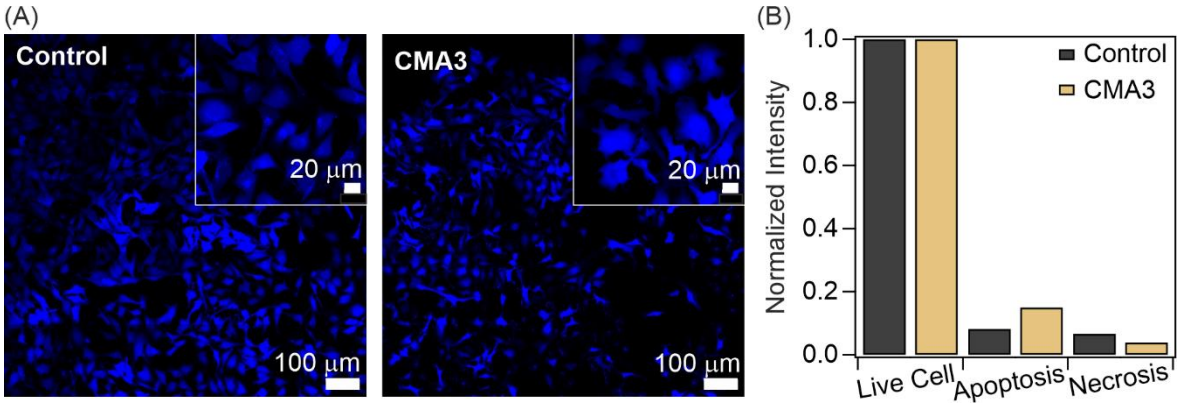

Figure 41. Results of apoptosis/necrosis assay determined for 5 mg/L CMA3 sample. The microscopic images show the blue labelled healthy cells for the control and the CMA3 treated cells (A). The bar graph shows the normalized intensity of living, apoptotic, and necrotic cells (B).

For the CMA3-treated samples as well as for the control test, all cells were colored blue (Figure 41) indicating the detection of a negligible amount of necrotic and apoptotic. This experiment was quantitatively evaluated by measuring the fluorescence intensity values (Figure 41 right). The normalized intensities show that apoptotic and necrotic cells revealed similar intensity in CMA3 treated cells as in control cells. These results show that the CMA3 sample at 5 mg/L concentration did not show any cytotoxic effect on HeLa cells.

5.4.3.2. Intracellular ROS scavenging assay for CMA3 sample

After evaluating the cell viability, the ROS test was also carried out in time dependent manner (Figure 42 (A)). The schematics of the reaction in the cells are shown in Figure 42 (B). The copper containing nanozyme was able to degrade the menadione induced ROS, which could be measured by monitoring the fluorescence intensity in the cells. The H_2DCFDA dye reacts with the ROS molecules and results in an increase in the fluorescence signal.

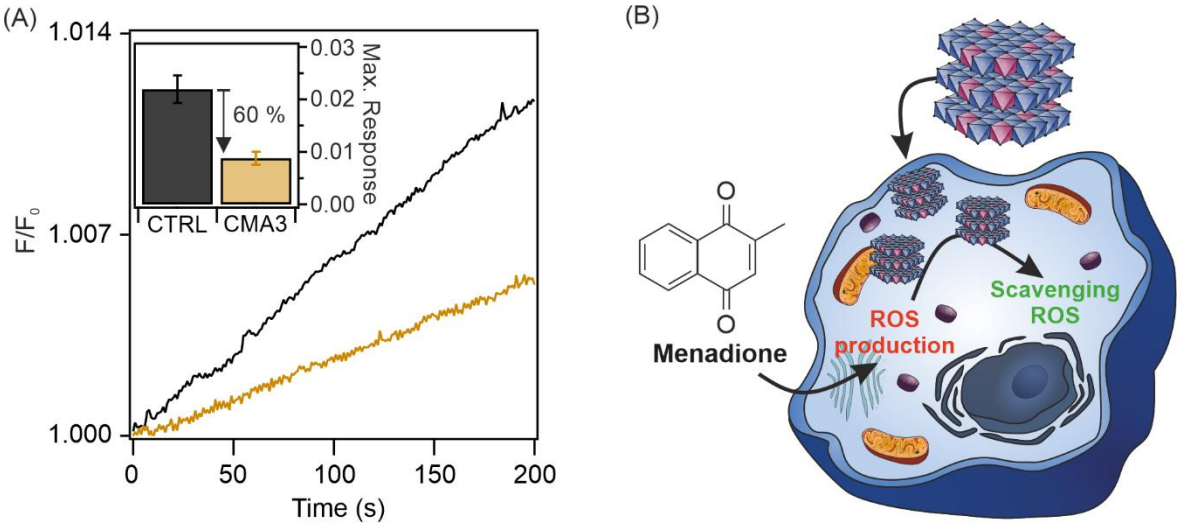

Figure 42. Normalized fluorescence intensity as a function of time for control (menadione-treated) and for CMA3-treated cells (A). The schematic representation of the ROS scavenging activity of the CMA3 sample (B). The inset in figure (A) shows the maximal response for the control and CMA3 treated cells.

In untreated cells, the fluorescence intensity increased rapidly after triggering ROS production with menadione, whereas this response was lower in cells treated with 5 mg/L CMA3. This means that CMA3 could capture the ROS molecules and thus inhibit their reaction with the fluorescent dye. The maximum response, as determined by the time dependent measurements, was reduced by 60 % compared to the control measurements. In conclusion, the CMA3 sample was found to be able to scavenge ROS molecules in intracellular conditions, therefore it could be potentially used in antioxidant treatments.

6. Summary

The increased concentration of ROS molecules can have serious consequences both in industrial fields as well as in living organisms. Molecular and enzymatic antioxidants are important for maintaining ROS levels, however, their sensitivity for the environmental conditions is an important challenge to address. Immobilization is a promising tool to overcome this disadvantageous property and it can also loan other useful properties to antioxidants. Various types of nanoparticles can serve as host material for antioxidant immobilization, including LDHs. Their remarkable anion exchange capacity and layered structure offers the opportunity to intercalate or adsorb the antioxidants on the inner/outer surfaces of the particles. The delaminated form can also serve as host material. The higher specific surface area possesses the ability of enhanced adsorption, while the restacking of the original lamellar structure, can induce the intercalation of the desired biomolecules among the layers. Polyelectrolytes are potential candidates to enhance both biomolecule immobilization and to enhance colloidal stability of the obtained dispersions. Since these nanosystems are usually applied in aqueous dispersions, latter issue aspect is of a great importance for the development of processable dispersions of antioxidant nanomaterials.

In the first part of the doctoral work, the colloidal behavior of dLDH nanosheets was investigated. It was revealed that the addition of salt solution divided the aggregation mechanism into two regimes. At low electrolyte concentrations, no change in particle size was observed, however, by increasing the ionic strength, the hydrodynamic radius increased steeply after a threshold time, leading to the formation of particle aggregates. With increasing salt concentration, the slope of the particle radius increased steeply, while the first constant size regime became shorter. Despite the fact that the second regime behaved according to the expected trend, no explanation was found for the first part. Since DLS can measure the largest dimension of the scattering object, it was proposed, that the restacking of the original lamellar LDH structure occurred, which only affected the particle thickness, but it had no effect on the lateral dimension of the particles. Thus, after the nanosheets recovered the LDH structure, they start to form randomly aggregated particles, resulting in steep increase in hydrodynamic particle size. The two regimes were separated with the CCT, which decreased by increasing the ionic strength. This phenomenon was also confirmed by turbidity, AFM and XRD studies. The colloidal stability was also demonstrated by DLS and turbidity measurements, resulting in good agreement of CCC values.

In the second part of the work, the dLDH particles were used as host material for the immobilization of three antioxidant enzymes (HRP, SOD and CAT), separated by two polyelectrolytes (Alg and TMC), which were used to adjust the particle charge and thus, to improve the enzyme adsorption. In general, at low polyelectrolyte concentration, no change in particle charge occurred, but as their concentration increased the absolute value of the zeta potentials started to decrease, and after charge neutralization, the particles became highly charged. The stability ratios determined in the same polyelectrolyte range were in line with the DLVO theory. The enzyme immobilization had no effect on the particle charge, so the dispersion remained stable. Polyelectrolyte and enzyme adsorption led to the formation of a rough surface compared to the bare nanosheets. The composite showed remarkable enzymatic activity in antioxidant test reactions. All three enzymes kept their function, furthermore, HRP and CAT immobilization gave rise to somewhat higher activity due to advantageous substrate-particle interactions. The cell penetration of the composite was demonstrated, while the intracellular antioxidant effect was also confirmed. The cytocompatibility test showed that the composite had no cytotoxic effect on HeLa cells. Furthermore, the composite had remarkable ROS scavenging potential and was also able to inhibit the oxidative stress induced DNA double strand break formation, while it was able to restore the intracellular ROS concentration to the control level.

In the third part, LDH particles were used as host material for molecular antioxidants. Two antioxidant molecules, TA and GSH, were successfully anchored in/on the LDH structure by applying two different synthesis methods. TA, due to its large size, adsorbed on the outer surface of LDH particles in both adsorption and coprecipitation methods. In contrast, GSH intercalated between the LDH layers in the coprecipitation method, while it was adsorbed on LDH particles in the adsorption method. The antioxidant immobilization was confirmed by various spectroscopic studies. Vibrational spectroscopic studies shed light on the different orientation of TA on the particle surface, which was in relation with the synthesis method. During adsorption, TA was anchored in a perpendicular way on the surface, while it was oriented parallel to the surface during coprecipitation. It was also found that LDH protected the antioxidants during the alkaline treatment, i.e., both TA and GSH kept their original structure. Radical scavenging assay exhibited the influence of the synthesis method on the radical scavenging activity. TA lost its radical scavenging ability after being immobilized by the coprecipitation method, while it remained active after adsorption method. This was in line with its orientation on the particle surface. After coprecipitation, TA was located parallel to the surface, therefore its phenolic hydroxyl groups

were hindered and could not reveal their radical scavenging activity. In contrast, after adsorption in a perpendicular orientation, the hydroxyl groups were more capable of reacting the free radicals in the reaction mixture, therefore it possessed a higher efficiency. The activity of GSH did not change significantly after immobilization, suggesting that anchoring in/on LDH particles did not affect the radical scavenging features. TA maintained its function after 1 month, both in solution and in heterogenized form. In contrast, bare GSH showed significantly higher effect after 1 month (originated from the decomposed form), while the immobilized form kept its original phenomena. It was concluded that LDH was able to protect GSH from self-degradation by providing it with structural stability. In the final step, the reusability of the most active sample was also investigated. The LDH/TA/a was used in 15 cycles without any loss of activity.

In the last part, an antioxidant nanozyme was presented by structural modification of LDH nanoparticle. In order to endow LDH nanoparticles with enzyme-like characteristics, Mg(II) ions were partially replaced by Cu(II) ions. By increasing the copper concentration in the synthesis process, three samples with different stoichiometric ratios were produced. The incorporation of Cu(II) was first assumed by the increased basal spacing, while the surface composition of the particles established that the surface copper(II) content increased in line with the initial stoichiometric ratio of copper(II) applied during the synthesis. The nanozymes showed remarkable CAT and SOD-like activity in chemical tests, moreover, the amount of the inserted Cu(II) centers did not affect their performance, i.e., they showed similar enzyme mimicking feature. The results of cytocompatibility study showed that the nanozymes had no cytotoxic effect on HeLa cells. In the ROS/superoxide scavenging assay, all samples showed significant activity and the CMA3 sample was further investigated in time-dependent cellular tests. The CMA3 did not induce cell death, and was able to reduce the ROS concentration in the HeLa cells.

In summary, LDH-based nanosystems of remarkable antioxidant activity have been developed. In addition, results of the aggregation mechanism of dLDH particles are useful in environmental remediation processes that rely on the intercalation of harmful anions through the restacking mechanism. The antioxidant systems obtained by enzyme immobilization are potential candidates in biomedical applications (e.g., inflammatory bowel disease), while the structural stability offered by the LDH particles and the reusability are important parameters in several industrial processes, where immobilized molecular antioxidants are desired. The developed nanozyme system represents alternatives to

biomolecules and can potentially be used in biomedical applications where the elimination of ROS is a crucial aspect (e.g., antioxidant coated implants, wound healing).

7. Tartalmi Összefoglaló

A megnövekedett ROS koncentráció számos komoly következménnyel járhat mind ipari, mind élettani folyamatokban. A molekuláris és enzimatikus antioxidánsok alkalmazhatóak lehetnek a ROS koncentráció szabályozására, azonban használatuk előtt a környezeti tényezőkre való érzékenységük fontos megoldandó probléma. Különböző hordozókon való rögzítésük megoldást jelenthet erre a negatív tulajdonságukra, továbbá más pozitív tulajdonságokat is biztosíthat számukra. Számos nanorészecske használható hordozóként, például az LDH-k. Réteges szerkezetük lehetőséget ad az antioxidánsok beépítésére a rétegek közé, valamint adszorpciójukra a felületen. A delaminált formájuk szintén alkalmazható lehet szubsztrátként, nagy fajlagos felületük nagyobb felületet biztosít, míg visszarétegződésre való hajlamuk a rétegközi beépítést segíti elő. Szekvenciális adszorpcióval multienzimatikus nanorendszerek is előállíthatóak, amelyekben a polielektrolitok elválasztó szerepet tölthetnek be az enzimek között, továbbá a nanorészecske diszperzió kolloidstabilitását is javíthatják. Mivel az antioxidáns tartalmú nanokompozitokat többnyire vizes diszperzióban alkalmazzák, a diszperziók kolloidstabilitásának vizsgálata és hangolása polielektrolitokkal számos területen fontos.

A munka első részében a delaminált LDH részecskék kolloid tulajdonságait vizsgáltuk. Megállapítottuk, hogy elektrolit jelenlétében a részecskék aggregációjának mechanizmusa két részre osztható. Alacsony ionerősségnél nincs megfigyelhető változás a részecskék méretében, azonban növelve a sókoncentrációt, a folyamat két jól elkülöníthető szakaszra bontható. A második szakasz jó egyezést mutatott a DLVO elmélettel, a hidrodinamikai sugár időben nőtt, a részecskék aggregálódtak. A sókoncentráció növelésével a részecskék aggregálódásának sebessége nőtt, míg az első szakasz rövidült. Annak ellenére, hogy a második szakasz a várt tendenciát mutatta, az első szakaszra nem volt magyarázat az irodalomban. Mivel a DLS csak a részecskék legnagyobb dimenzióját méri, így feltételeztük, hogy a nanolapok első lépésben kialakítják az eredeti réteges szerkezetet, mely nem befolyásolja a részecskék átmérőjét, tehát nem detektálható változás DLS mérések során. A nanolapok visszarétegződése után aggregátumok képződnek, amely jelentős növekedést okoz a hidrodinamikai sugarakban. A két szakaszt a CCT választja el egymástól, mely az ionerősség növelésével arányosan csökken. Ezt a jelenséget a turbiditás, AFM és XRD

mérések is alátámasztottuk. A mechanizmus felderítése után a kolloidstabilitást DLS és turbiditás mérésekkel vizsgáltuk, amelyekből megállapítható, hogy a CCC értékek jó egyezést mutattak. Összefoglalva megállapítható, hogy az aggregáció mechanizmusa két lépésre osztható: első lépésben visszaalakul az eredeti LDH szerkezet, majd ezt kártyavárszerű aggregátumok kialakulása követi.

Második lépésben a korábban vizsgált delaminált LDH-kat használtuk hordozóként három antioxidáns enzim (HRP, SOD és CAT) rögzítésére, amelyeket két polielektrolit réteggel választottunk el egymástól (Alg és TMC). A polielektrolitok segítségével hangoltuk a részecskék töltését, ezzel elősegítve az enzimek adszorpcióját. A polielektrolitok hasonló tendenciát mutattak az adszorpció során, kezdetben - kis koncentrációnál - nem befolyásolták a részecskék töltését, míg növelve koncentrációjukat, a zeta potenciálok abszolút értéke előbb csökkent, majd a részecskék semlegessé válását követően jelentős töltéssel bírtak. A stabilitás arányokat ugyanabban a tartományban meghatározva jó egyezést mutattak a DLVO elmélettel. Az enzimek rögzítése nem befolyásolta a részecskék töltését, így a diszperziók stabilak maradtak.

A SAXS mérések alátámasztották a polielektrolitok és az enzimek adszorpcióját, ugyanis a növekvő elektronsűrűség fluktuáció a sima felülettel szemben érdesebb felület kialakulására utalt. A kompozit jelentős enzimatikus aktivitást mutatott a kémiai tesztekben. Mindhárom enzim megtartotta aktivitást, sőt a HRP nagyobb affinitást mutatott a szubsztrát iránt, míg a CAT is magasabb aktivitással bírt rögzítés után. A dSTORM mérések szintén alátámasztották az enzimek rögzülését, továbbá kimutatták, hogy a részecskék képesek bejutni az intracelluláris térbe. A kompozit antioxidáns hatását intracelluláris körülmények között is igazoltuk. Kimutattuk, hogy a kompozitnak nincs citotoxikus hatása a HeLa sejtekre, továbbá a kompozit jelentős ROS semlegesítő hatással bír. Végül megállapítottuk, hogy a kompozit képes csökkenteni az oxidatív stressz által generált DNS kettős szál törések képződését. Amellett, hogy a kompozit gyökfogó hatással bírt, visszaállította a normál antioxidáns/ROS arányt a sejtekben.

A munka harmadik részében LDH részecskéket használtunk templátként, molekuláris antioxidánsok rögzítésére. Két molekuláris antioxidánst, TA-t és GSH-t rögzítettünk sikeresen LDH-n mind a rétegek között, mind a felületen. A TA, nagy méretének köszönhetően, az adszorpció, illetve az együttes lecsapás esetén is az LDH részecske felületén rögzült. Ezzel szemben, a GSH együttes lecsapás esetén az LDH rétegei közé, míg adszorpció során az LDH részecskék felületén rögzült. Az antioxidánsok immobilizálását különböző spektroszkópiás módszerekkel bizonyítottuk. Rezgési spektroszkópiás

módszerek rámutattak a TA különböző orientációban történő rögzülésére, amelyet a szintézis módja határozott meg. Adszorpció során a TA merőlegesen, míg együttes lecsapáskor párhuzamosan rögzült a részecske felületén. Továbbá bebizonyosodott, hogy az LDH részecske a bázikus körülményekkel szemben is védő hatást fejtett ki az antioxidánsokra, ugyanis a szintézis során nem következett be változás szerkezetükben. A Raman mérések továbbá bizonyították, hogy a GSH mellett, annak oxidált formája, a GSSG is rögzült az LDH felületén. Az UV-VIS-NIR eredmények szintén alátámasztották a szerves molekulák jelenlétét, míg gyökfogó aktivitásukat DPPH teszttel bizonyítottuk.

A TA aktivitása jelentősen lecsökkent az együttes lecsapással történő rögzüléskor, míg adszorpció esetén magasabb aktivitás volt mérhető a szabad antioxidánshoz képest. Ez összhangban volt a felületen való rögzülés módjával. Együttes lecsapáskor a TA párhuzamos elhelyezkedése miatt a hidroxil csoportjai nehezebben hozzáférhetőek a gyökök számára, ami jelentősen csökkentette aktivitását. Ezzel szemben az adszorpciós technikával előállított merőleges orientáció esetén a hidroxil csoportok sokkal könnyebben hozzáférhetőek, tehát könnyebben ki tudja fejteni gyökfogó hatását. A GSH aktivitása nem változott jelentősen rögzítés után, így megállapítottuk, hogy a rögzítés nem befolyásolta aktivitását. Azonban különbséget figyeltünk meg az időfüggő mérések esetén. Míg a TA megtartotta aktivitását szabad és rögzített formában is, a GSH egy hónap elteltével magasabb aktivitás mutatott szabad formában. A GSH magasabb aktivitása a bomlástermékeinek megjelenésével magyarázható, így megállapítottuk, hogy az LDH képes volt megőrizni a GSH eredeti szerkezetét, akadályozva bomlását. Utolsó lépésben a legjobbnak minősülő minta, az LDH/TA/a újrafelhasználhatóságát vizsgáltuk, amely során megállapítottuk, hogy a kompozit 15 ciklusig jelentős aktivitással bír.

A doktori munka utolsó lépéseként antioxidáns aktivitású nanozimet állítottunk elő az LDH részecskék szerkezeti módosításával. Annak érdekében, hogy az LDH részecskék enzimatikus aktivitással rendelkezzenek, a Mg(II) ionok egy részét Cu(II) ionokra cseréltük. A rézkoncentráció változtatásával három mintát állítottunk elő, amelyek különböző sztöchiometriai arányban tartalmaztak Cu(II) ionokat. A rézionok sikeres beépítését első lépésben XRD mérésekkel bizonyítottuk. A diffraktogramok alapján kiszámítottuk a *d* és *c* kristályparamétereket, amelyek nagyobb értékeket mutattak a réztartalmú minták esetén. Az XRD eredmények mellett az XPS mérések is igazolták a rézionok jelenlétét. A felület összetétele jó egyezést mutatott a szintézis során alkalmazott rézkoncentrációkkal, ugyanis a nagyobb sztöchiometriai arány magasabb réztartalmat eredményezett. Az XRD és XPS

eredmények mellett FLIM és Raman mérések megerősítették a Cu(II) ionok beépülését a szerkezetbe.

A szerkezeti tulajdonságok vizsgálata után, kémiai tesztekkel és intracelluláris mérésekkel vizsgáltuk a CMA minták enzimatikus aktivitását. A kémiai tesztekben a nanozimek kiemelkedő CAT és SOD aktivitást mutattak, ugyanakkor a Cu(II) mennyisége nem befolyásolta aktivitásukat. Az intracelluláris mérések során első lépésben a sejtekre gyakorolt citotoxicitást vizsgáltuk, amely során megállapítottuk, hogy a nanorészecskék nem mutatnak toxikus hatást a HeLa sejteken. A ROS/SOD teszt során a minták jelentős aktivitás mutattak, amelyek alapján a CMA3 mintát választottuk a további időfüggő mérések elvégzéséhez. Az apoptotikus/nekrotikus sejtek vizualizálására mikroszkópos méréseket végezve bizonyítottuk, hogy a CMA3 minta nem mutat citotoxikus hatást és csökkenteni tudja a menadion által indukált ROS koncentrációját a sejtekben. Ezek alapján megállapítottuk, hogy a Cu(II) tartalmú nanozimek jelentős enzimatikus aktivitással bírnak, amelyet mind kémiai tesztekben, mind intracelluláris környezetben bizonyítottunk.

Összefoglalva, a delaminált LDH részecskék kolloid tulajdonságainak feltérképezése után három LDH-alapú antioxidáns aktivitással rendelkező rendszert fejlesztettünk ki. A kolloidstabilitás vizsgálatával megállapítottuk, hogy a dLDH-k első lépésben visszanyerik eredeti réteges szerkezetüket, amit random aggregátumok kialakulása követett. Az aggregáció mechanizmusa hasonló volt a DLS és turbiditás mérések során és hasznos lehet környezetszennyező folyamatok kezelésére, a környezetre káros anionok LDH rétegei közé történő beépítésével. Antioxidáns enzimek dLDH felületén történő rögzítésével létrehozott nanokompozit jelentős aktivitást mutatott mind a kémiai tesztekben, mind intracelluláris körülmények között, így potenciálisan alkalmazható lehet különböző orvosbiológiai felhasználásokban (pl. gyulladásos bélbetegség). Az enzimek mellett, molekuláris antioxidánsokat is sikeresen rögzítettünk LDH-k felületén és rétegei között. Az LDH-k által biztosított szerkezeti stabilitás és újrafelhasználhatóság lehetővé teszi használatukat különböző ipari folyamatokban, hozzájárulva azok költséghatékonyságához. Az utolsó fejezet egy olyan nanozim fejlesztését mutatta be, amelyet molekuláris/enzimatikus antioxidáns rögzítése nélkül, az LDH-k szerkezetének módosításával hoztunk létre. Ezáltal kiküszöbölhetőek a biomolekulák negatív tulajdonságai, és potenciálisan alkalmazható lehet olyan orvosbiológiai területeken, amelyekben fontos a ROS koncentrációjának csökkentése (pl. antioxidánssal bevont implantátumok, sebkezelés).

8. Acknowledgement

First, I would like to express my deepest gratitude to my supervisor, Dr. István Szilágyi for giving me the opportunity to work in his research group, first as an MSc student and from 2020 as a PhD student. I am very grateful to him for his guidance, patience, and advice during my studies. I owe him special thanks for giving me the opportunity to participate in research programs abroad. Without him, I could not complete this thesis.

I would like to thank the head of the Department of Physical Chemistry and Materials Science, Prof. Dr. Ágota Tóth, for the opportunity to complete my PhD studies at her department.

I am very grateful to Prof. Dr. Zhi Ping Xu for allowing me to spend 3 months in his research group at the University of Queensland. The time spent there has greatly contributed to my professional development.

I am grateful to Dr. József Maléth, Dr. Tamara Madácsy and Dr. Árpád Varga for the cellular measurements performed in the Momentum Epithelial Cell Signalling and Secretion Research Group. I owe special thanks to Prof. Dr Kónya Zoltán, Prof. Dr. Kukovecz Ákos, Dr. Gábor Varga, Dr. Gábor Schuszter and Edina Papp-Balog for the common work. I am grateful to Dr. István Tóth and his group members for their collaboration.

Many thanks to Dr. Dániel Sebők, Dr. Gergely Ferenc Samu and Dr. Márton Szabados for the XRD, XPS and TG-MS measurements.

I am thankful to the secretaries of the department, Ildikó Patakiné Sziveri and Csilla Barra, for their help with the administrative tasks.

I am specially thankful to all my current (Zsuzsi) and former co-supervised high school/BSc students (Lili, Kata, Gréta, Deján, Szilárd).

I am grateful to the former (Zoli, Szabi, Szilárd, Nizar) and current (Bojana, Dóri, Zsófi, Kata, Gréta, Laila and Tibi) members of the Biocolloids Research Group. The daily work with them was much more fun and I will always have fond memories of them.

I would like to thank all my friends (especially Timi, Ákos, Eszter and S. Dóri) who always stood by my side and made sure that I could always count on them.

I am especially grateful to Gábor for his endless love, support, and patience.

Finally, I owe the greatest gratitude to my loving parents and grandparents for their unwavering support and love. Thank you for being by my side during my studies and supporting me in my life so far.

9. References

(1) Valko, M.; Rhodes, C. J.; Moncol, J.; Izakovic, M.; Mazur, M. Free radicals, metals and antioxidants in oxidative stress-induced cancer. *Chem. Biol. Interact.* **2006**, *160* (1), 1-40
(2) Schieber, M.; Chandel, N. S. ROS function in redox signaling and oxidative stress. *Curr. Biol.* **2014**, *24* (10), R453-R462
(3) Sies, H.; Jones, D. P. Reactive oxygen species (ROS) as pleiotropic physiological signalling agents. *Nat. Rev. Mol. Cell Biol.* **2020**, *21* (7), 363-383
(4) Forman, H. J.; Zhang, H. Q. Targeting oxidative stress in disease: promise and limitations of antioxidant therapy. *Nat. Rev. Drug Discov.* **2021**, *20* (9), 689-709
(5) Pisoschi, A. M.; Pop, A. The role of antioxidants in the chemistry of oxidative stress: A review. *Eur. J. Med. Chem.* **2015**, *97*, 55-74
(6) Nimse, S. B.; Pal, D. Free radicals, natural antioxidants, and their reaction mechanisms. *RSC Adv.* **2015**, *5* (35), 27986-28006
(7) Gulcin, I. Antioxidants and antioxidant methods: an updated overview. *Arch. Toxicol.* **2020**, *94* (3), 651-715
(8) Lim, Y. Y.; Lim, T. T.; Tee, J. J. Antioxidant properties of several tropical fruits: A comparative study. *Food Chem.* **2007**, *103* (3), 1003-1008
(9) Hakkinen, S.; Heinonen, M.; Karenlampi, S.; Mykkanen, H.; Ruuskanen, J.; Torronen, R. Screening of selected flavonoids and phenolic acids in 19 berries. *Food Res. Int.* **1999**, *32* (5), 345-353
(10) Kaur, C.; Kapoor, H. C. Anti-oxidant activity and total phenolic content of some Asian vegetables. *Int. J. Food Sci. Technol.* **2002**, *37* (2), 153-161
(11) Moure, A.; Cruz, J. M.; Franco, D.; Domínguez, J. M.; Sineiro, J.; Domínguez, H.; Núñez, M. J.; Parajó, J. C. Natural antioxidants from residual sources. *Food Chem.* **2001**, *72* (2), 145-171
(12) Wojdylo, A.; Oszmianski, J.; Czemerys, R. Antioxidant activity and phenolic compounds in 32 selected herbs. *Food Chem.* **2007**, *105* (3), 940-949
(13) Ramadan, M. F.; Kroh, L. W.; Morsel, J. T. Radical scavenging activity of black cumin (Nigella sativa L.), coriander (Coriandrum sativum L.), and niger (Guizotia abyssinica Cass.) crude seed oils and oil fractions. *J. Agric. Food Chem.* **2003**, *51* (24), 6961-6969
(14) Gao, P.; Liu, R. J.; Jin, Q. Z.; Wang, X. G. Comparative study of chemical compositions and antioxidant capacities of oils obtained from two species of walnut: Juglans regia and Juglans sigillata. *Food Chem.* **2019**, *279*, 279-287
(15) Lü, J. M.; Lin, P. H.; Yao, Q. Z.; Chen, C. Y. Chemical and molecular mechanisms of antioxidants: experimental approaches and model systems. *J. Cell. Mol. Med.* **2010**, *14* (4), 840-860
(16) Pietta, P. G. Flavonoids as antioxidants. *J. Nat. Prod.* **2000**, *63* (7), 1035-1042
(17) Hagerman, A. E.; Riedl, K. M.; Jones, G. A.; Sovik, K. N.; Ritchard, N. T.; Hartzfeld, P. W.; Riechel, T. L. High molecular weight plant polyphenolics (tannins) as biological antioxidants. *J. Agric. Food Chem.* **1998**, *46* (5), 1887-1892
(18) Amarowicz, R. Tannins: the new natural antioxidants? *Eur. J. Lipid Sci. Technol.* **2007**, *109* (6), 549-551
(19) Picquart, M.; Grajcar, L.; Baron, M. H.; Abedinzadeh, Z. Vibrational spectroscopic study of glutathione complexation in aqueous solutions. *Biospectroscopy* **1999**, *5* (6), 328-337
(20) Bugg, T. *Introduction to enzyme and coenzyme chemistry*; Blackwell Publishing Ltd, 2004.
(21) Robinson, P. K. Enzymes: principles and biotechnological applications. In *Understanding biochemistry: Enzymes and membranes*, Essays in Biochemistry, Vol. 59; 2015; pp 1-41.
(22) Garcia-Viloca, M.; Gao, J.; Karplus, M.; Truhlar, D. G. How enzymes work: Analysis by modern rate theory and computer simulations. *Science* **2004**, *303* (5655), 186-195
(23) Copeland, R. A. *Enzymes - A practical introduction to structure, mechanism, and data analysis*; Wiley-VCH Inc, 2000.
(24) Sies, H. Oxidative stress: Oxidants and antioxidants. *Exp. Physiol.* **1997**, *82* (2), 291-295
(25) El-Missiry, M. A. *Antioxidant enzyme*; InTech, 2012.
(26) McCord, J. M.; Fridovic, I. Superoxide dismutase - An enzymic function for erythrocuprein (hemocuprein). *J. Biol. Chem.* **1969**, *244* (22), 6049-6055

(27) Henke, S. L. Superoxide dismutase mimics as future therapeutics. *Expert Opin. Ther. Patents* **1999**, *9* (2), 169-180
(28) Fita, I.; Rossmann, M. G. The active-center of catalase. *J. Mol. Biol.* **1985**, *185* (1), 21-37
(29) Wu, A. J.; Penner-Hahn, J. E.; Pecoraro, V. L. Structural, spectroscopic, and reactivity models for the manganese catalases. *Chem. Rev.* **2004**, *104* (2), 903-938
(30) Bhabak, K. P.; Mugesh, G. Functional mimics of glutathione peroxidase: Bioinspired synthetic antioxidants. *Accounts Chem. Res.* **2010**, *43* (11), 1408-1419
(31) Veitch, N. C. Horseradish peroxidase: a modern view of a classic enzyme. *Phytochemistry* **2004**, *65* (3), 249-259
(32) Wu, H. Z.; Ghirmai, S.; Undeland, I. Stabilization of herring (Clupea harengus) by-products against lipid oxidation by rinsing and incubation with antioxidant solutions. *Food Chem.* **2020**, *316*,
(33) Lourenco, S. C.; Moldao-Martins, M.; Alves, V. D. Antioxidants of natural plant origins: From sources to food industry applications. *Molecules* **2019**, *24* (22), 4132
(34) Souza, V. G. L.; Pires, J. R. A.; Rodrigues, P. F.; Lopes, A. A. S.; Fernandes, F. M. B.; Duarte, M. P.; Coelhoso, I. M.; Fernando, A. L. Bionanocomposites of chitosan/montmorillonite incorporated with Rosmarinus officinalis essential oil: Development and physical characterization. *Food Packaging Shelf Life* **2018**, *16*, 148-156
(35) Nirmala, C.; Bisht, M. S.; Bajwa, H. K.; Santosh, O. Bamboo: A rich source of natural antioxidants and its applications in the food and pharmaceutical industry. *Trends Food Sci. Technol.* **2018**, *77*, 91-99
(36) Brito, J.; Hlushko, H.; Abbott, A.; Aliakseyeu, A.; Hlushko, R.; Sukhishvili, S. A. Integrating antioxidant functionality into polymer materials: Fundamentals, strategies, and applications. *ACS Appl. Mater. Interfaces* **2021**, *13* (35), 41372-41395
(37) Hoang, H. T.; Moon, J. Y.; Lee, Y. C. Natural antioxidants from plant extracts in skincare cosmetics: Recent applications, challenges and perspectives. *Cosmetics* **2021**, *8* (4), 106
(38) Couto, J.; Figueirinha, A.; Batista, M. T.; Paranhos, A.; Nunes, C.; Goncalves, L. M.; Marto, J.; Fitas, M.; Pinto, P.; Ribeiro, H. M.; et al. Fragaria vesca L. extract: A promising cosmetic ingredient with antioxidant properties. *Antioxidants* **2020**, *9* (2), 154
(39) Boo, Y. C. Can plant phenolic compounds protect the skin from airborne particulate matter? *Antioxidants* **2019**, *8* (9), 379
(40) Rigoussen, A.; Verge, P.; Raquez, J. M.; Dubois, P. Natural phenolic antioxidants as a source of biocompatibilizers for immiscible polymer blends. *ACS Sustain. Chem. Eng.* **2018**, *6* (10), 13349-13357
(41) Kirschweng, B.; Tatraaljai, D.; Foldes, E.; Pukanszky, B. Natural antioxidants as stabilizers for polymers. *Polym. Degrad. Stab.* **2017**, *145*, 25-40
(42) Duy, M.; Matrat, M.; Ben Amara, A.; Foucher, F.; Moreau, B.; Yu, Y.; Goussougli, M.; Fournet, R.; Sirjean, B.; Glaude, P. A. Antioxidant effect of 2-4 xylenol on fuel oxidation in liquid and gas phase over a wide temperature range. *Fuel Process. Technol.* **2022**, *236*, 107414
(43) Xi, Z. L.; Jin, B. X.; Jin, L. Z.; Li, M. T.; Li, S. S. Characteristic analysis of complex antioxidant enzyme inhibitors to inhibit spontaneous combustion of coal. *Fuel* **2020**, *267*,
(44) Grishin, D. F. Depressant, antiwear, and antioxidant additives to hydrotreated diesel fuels with low and ultralow sulfur content (Review). *Pet. Chem.* **2017**, *57* (10), 813-825
(45) Kumar, A.; Gupta, V.; Aakriti. *Discovery of neuroprotective antioxidants for the management of ischemic brain stroke*; Elsevier Science Bv, 2018.
(46) Neto, F. C.; Marton, L. T.; de Marqui, S. V.; Lima, T. A.; Barbalho, S. M. Curcuminoids from Curcuma Longa: New adjuvants for the treatment of crohn's disease and ulcerative colitis? *Crit. Rev. Food Sci. Nutr.* **2019**, *59* (13), 2136-2143
(47) Moura, F. A.; de Andrade, K. Q.; dos Santos, J. C. F.; Araujo, O. R. P.; Goulart, M. O. F. Antioxidant therapy for treatment of inflammatory bowel disease: Does it work? *Redox Biol.* **2015**, *6*, 617-639
(48) Barbosa, J. A. P.; Santana, M. A. N.; Leite, T. C. C.; de Oliveira, T. B.; Mota, F. V. B.; Bastos, I.; Correa, A. J. C.; de Amorim, E. L. C.; Vieira, J. R. C.; Silva, T. M. S.; et al. Gastroprotective effect of ethyl acetate extract from Avicennia schaueriana Stapf & Leechman and underlying mechanisms. *Biomed. Pharmacother.* **2019**, *112*,

(49) Molino, S.; Casanova, N. A.; Henares, J. A. R.; Miyakawa, M. E. F. Natural tannin wood extracts as a potential food ingredient in the food industry. *J. Agric. Food Chem.* **2020**, *68* (10), 2836-2848
(50) López, M. D. C.; de Dicastillo, C. L.; Vilariño, J. M. L.; Rodríguez, M. V. G. Improving the capacity of polypropylene to be used in antioxidant active films: Incorporation of plasticizer and natural antioxidants. *J. Agric. Food Chem.* **2013**, *61* (35), 8462-8470
(51) Benbettaieb, N.; Nyagaya, J.; Seuvre, A. M.; Debeaufort, F. Antioxidant activity and release kinetics of caffeic and p-coumaric acids from hydrocolloid-based active films for healthy packaged food. *J. Agric. Food Chem.* **2018**, *66* (26), 6906-6916
(52) Bafana, A.; Dutt, S.; Kumar, S.; Ahuja, P. S. Superoxide dismutase: an industrial perspective. *Crit. Rev. Biotechnol.* **2011**, *31* (1), 65-76
(53) Galante, Y. A.; Formantici, C. Enzyme applications in detergency and in manufacturing industries. *Curr. Org. Chem.* **2003**, *7* (13), 1399-1422
(54) Kirk, O.; Borchert, T. V.; Fuglsang, C. C. Industrial enzyme applications. *Curr. Opin. Biotechnol.* **2002**, *13* (4), 345-351
(55) Rives, V. *Layered double hydroxides: Present and future*; Nova Science Publishers, Inc., 2001.
(56) Evans, D. G.; Slade, R. C. T. Structural aspects of layered double hydroxides. In *Layered Double Hydroxides*, Duan, X., Evans, D. G. Eds.; Structure and Bonding, Vol. 119; 2006; pp 1-87.
(57) Prince, J.; Montoya, A.; Ferrat, G.; Valente, J. S. Proposed General Sol-Gel Method to Prepare Multimetallic Layered Double Hydroxides: Synthesis, Characterization, and Envisaged Application. *Chem. Mater.* **2009**, *21* (24), 5826-5835
(58) Bergaya, F.; Lagaly, G. *Handbook of Clay Science*; Elsevier, 2013.
(59) He, J.; Wei, M.; Li, B.; Kang, Y.; Evans, D. G.; Duan, X. Preparation of layered double hydroxides. In *Layered Double Hydroxides*, Duan, X., Evans, D. G. Eds.; Structure and Bonding, Vol. 119; 2006; pp 89-119.
(60) Novoselov, K. S.; Geim, A. K.; Morozov, S. V.; Jiang, D.; Zhang, Y.; Dubonos, S. V.; Grigorieva, I. V.; Firsov, A. A. Electric field effect in atomically thin carbon films. *Science* **2004**, *306* (5696), 666-669
(61) Nicolosi, V.; Chhowalla, M.; Kanatzidis, M. G.; Strano, M. S.; Coleman, J. N. Liquid exfoliation of layered materials. *Science* **2013**, *340* (6139), 1420-1420
(62) Adachi-Pagano, M.; Forano, C.; Besse, J. P. Delamination of layered double hydroxides by use of surfactants. *Chem. Commun.* **2000**, (1), 91-92
(63) Leroux, F.; Adachi-Pagano, M.; Intissar, M.; Chauviere, S.; Forano, C.; Besse, J. P. Delamination and restacking of layered double hydroxides. *J. Mater. Chem.* **2001**, *11* (1), 105-112
(64) Yu, J. F.; Wang, Q.; O'Hare, D.; Sun, L. Y. Preparation of two dimensional layered double hydroxide nanosheets and their applications. *Chem. Soc. Rev.* **2017**, *46* (19), 5950-5974
(65) Chen, Z. K.; Fan, Q. Q.; Huang, M. H.; Colfen, H. Synthesis of two-dimensional layered double hydroxides: a systematic overview. *Crystengcomm* **2022**, *24* (26), 4639-4655
(66) Yu, J. F.; Liu, J. J.; Clearfield, A.; Sims, J. E.; Speiegle, M. T.; Suib, S. L.; Sun, L. Y. Synthesis of layered double hydroxide single-layer nanosheets in formamide. *Inorg. Chem.* **2016**, *55* (22), 12036-12041
(67) Wu, Q. L.; Olafsen, A.; Vistad, O. B.; Roots, J.; Norby, P. Delamination and restacking of a layered double hydroxide with nitrate as counter anion. *J. Mater. Chem.* **2005**, *15* (44), 4695-4700
(68) Hibino, T.; Jones, W. New approach to the delamination of layered double hydroxides. *J. Mater. Chem.* **2001**, *11* (5), 1321-1323
(69) Zhang, Y. P.; Li, H. P.; Du, N.; Zhang, R. J.; Hou, W. G. Large-scale aqueous synthesis of layered double hydroxide single-layer nanosheets. *Colloids Surf. A* **2016**, *501*, 49-54
(70) Bao, W. L.; Wang, J. Y.; Wang, Q.; O'Hare, D.; Wan, Y. L. Layered double hydroxide nanotransporter for molecule delivery to intact plant cells. *Sci. Rep.* **2016**, *6*, 26738
(71) Hou, W.; Kang, L.; Sun, R.; Liu, Z.-H. Exfoliation of layered double hydroxides by an electrostatic repulsion in aqueous solution. *Colloids Surf. A* **2008**, *312* (2–3), 92-98
(72) Venugopal, B. R.; Shivakumara, C.; Rajamathi, M. Effect of various factors influencing the delamination behavior of surfactant intercalated layered double hydroxides. *J. Colloid Interface Sci.* **2006**, *294* (1), 234-239
(73) Jobbágy, M. a.; Regazzoni, A. E. Delamination and restacking of hybrid layered double hydroxides assessed by in situ XRD. *J. Colloid Interface Sci.* **2004**, *275* (1), 345-348

(74) Murath, S.; Somosi, Z.; Toth, I. Y.; Tombacz, E.; Sipos, P.; Palinko, I. Delaminating and restacking MgAl-layered double hydroxide monitored and characterized by a range of instrumental methods. *J. Mol. Struct.* **2017**, *1140*, 77-82
(75) Mishra, G.; Dash, B.; Pandey, S. Layered double hydroxides: A brief review from fundamentals to application as evolving biomaterials. *Appl. Clay. Sci.* **2018**, *153*, 172-186
(76) Zhang, L. P.; Zhao, J. L.; Zhang, S. W.; Yu, Q. Q.; Cheng, J.; Qiu, X. H. Ultrasound-assisted synthesis of single layer MgAl hydrotalcite for the removal of Cr(VI) in solution and soil. *Appl. Clay. Sci.* **2021**, *204*, 106025
(77) Wang, Q. W.; Lin, Q. H.; Li, Q. Z.; Li, K. Z.; Wu, L. Y.; Li, S. M.; Liu, H. As(III) removal from wastewater and direct stabilization by in-situ formation of Zn-Fe layered double hydroxides. *J. Hazard. Mater.* **2021**, *403*, 123920
(78) Varga, G.; Somosi, Z.; Kukovecz, A.; Konya, Z.; Palinko, I.; Szilagyi, I. A colloid chemistry route for the preparation of hierarchically ordered mesoporous layered double hydroxides using surfactants as sacrificial templates. *J. Colloid Interface Sci.* **2021**, *581*, 928-938
(79) Zhang, X.; Yan, L. G.; Li, J.; Yu, H. Q. Adsorption of heavy metals by L-cysteine intercalated layered double hydroxide: Kinetic, isothermal and mechanistic studies. *J. Colloid Interface Sci.* **2020**, *562*, 149-158
(80) Zhang, P.; Ouyang, S. D.; Li, P.; Huang, Y.; Frost, R. L. Enhanced removal of ionic dyes by hierarchical organic three-dimensional layered double hydroxide prepared via soft-template synthesis with mechanism study. *Chem. Eng. J.* **2019**, *360*, 1137-1149
(81) Wu, J. Y.; Ye, Q. Y.; Wu, P. X.; Xu, S. R.; Liu, Y. J.; Ahmed, Z.; Rehman, S.; Zhu, N. W. Heteroaggregation of nanoplastics with oppositely charged minerals in aquatic environment: Experimental and theoretical calculation study. *Chem. Eng. J.* **2022**, *428*, 9
(82) Chen, Z. Y.; Chen, C. Y.; Luo, X. W.; Liu, J. H.; Huang, Z. J. Flocculation of polystyrene nanoplastics in water using Mg/Al layered double hydroxides via heteroaggregation. *Appl. Clay. Sci.* **2021**, *213*, 106264
(83) Tiwari, E.; Singh, N.; Khandelwal, N.; Monikh, F. A.; Darbha, G. K. Application of Zn/Al layered double hydroxides for the removal of nanoscale plastic debris from aqueous systems. *J. Hazard. Mater.* **2020**, *397*, 122769
(84) Tokudome, Y.; Morimoto, T.; Tarutani, N.; Vaz, P. D.; Nunes, C. D.; Prevot, V.; Stenning, G. B. G.; Takahashi, M. Layered double hydroxide nanoclusters: Aqueous, concentrated, stable, and catalytically active colloids toward green chemistry. *ACS Nano* **2016**, *10* (5), 5550-5559
(85) Sipiczki, M.; Adam, A. A.; Anitics, T.; Csendes, Z.; Peintler, G.; Kukovecz, A.; Konya, Z.; Sipos, P.; Palinko, I. The catalytic epoxidation of 2-cyclohexen-1-one over uncalcined layered double hydroxides using various solvents. *Catal. Today* **2015**, *241*, 231-236
(86) Varga, G.; Kukovecz, A.; Konya, Z.; Korecz, L.; Murath, S.; Csendes, Z.; Peintler, G.; Carlson, S.; Sipos, P.; Palinko, I. Mn(II)-amino acid complexes intercalated in CaAl-layered double hydroxide - Well-characterized, highly efficient, recyclable oxidation catalysts. *J. Catal.* **2016**, *335*, 125-134
(87) Wang, T. J.; Liu, X. Y.; Li, Y.; Li, F. M.; Deng, Z. W.; Chen, Y. Ultrasonication-assisted and gram-scale synthesis of Co-LDH nanosheet aggregates for oxygen evolution reaction. *Nano Res.* **2020**, *13* (1), 79-85
(88) Dionigi, F.; Zeng, Z. H.; Sinev, I.; Merzdorf, T.; Deshpande, S.; Lopez, M. B.; Kunze, S.; Zegkinoglou, I.; Sarodnik, H.; Fan, D. X.; et al. In-situ structure and catalytic mechanism of NiFe and CoFe layered double hydroxides during oxygen evolution. *Nat. Commun.* **2020**, *11* (1), 2522
(89) Zhang, H.; Li, H. Y.; Akram, B.; Wang, X. Fabrication of NiFe layered double hydroxide with well-defined laminar superstructure as highly efficient oxygen evolution electrocatalysts. *Nano Res.* **2019**, *12* (6), 1327-1331
(90) Dong, C. L.; Zhang, X. L.; Xu, J.; Si, R.; Sheng, J.; Luo, J.; Zhang, S. N.; Dong, W. J.; Li, G. B.; Wang, W. C.; et al. Ruthenium-doped cobalt-chromium layered double hydroxides for enhancing oxygen evolution through regulating charge transfer. *Small* **2020**, *16* (5), 1905328
(91) Zhou, Y. M. H.; Shuai, L.; Jiang, X. Y.; Jiao, F. P.; Yu, J. G. Visible-light-driven photocatalytic properties of layered double hydroxide supported-Bi2O3 modified by Pd(II) for methylene blue. *Adv. Powder Technol.* **2015**, *26* (2), 439-447

(92) Pausova, S.; Krysa, J.; Jirkovsky, J.; Forano, C.; Mailhot, G.; Prevot, V. Insight into the photocatalytic activity of ZnCr-CO3 LDH and derived mixed oxides. *Appl. Catal. B-Environ.* **2015**, *170*, 25-33
(93) Teramura, K.; Iguchi, S.; Mizuno, Y.; Shishido, T.; Tanaka, T. Photocatalytic Conversion of CO2 in Water over Layered Double Hydroxides. *Angew. Chem. Int. Edit.* **2012**, *51* (32), 8008-8011
(94) Varga, G.; Kozma, V.; Kolcsar, V. J.; Kukovecz, A.; Konya, Z.; Sipos, P.; Palinko, I.; Szollosi, G. beta-Isocupreidinate-CaAl-layered double hydroxide composites-heterogenized catalysts for asymmetric Michael addition. *Mol. Catal.* **2020**, *482*, 110675
(95) An, Z.; Zhang, W. H.; Shi, H. M.; He, J. An effective heterogeneous L-proline catalyst for the asymmetric aldol reaction using anionic clays as intercalated support. *J. Catal.* **2006**, *241* (2), 319-327
(96) Ning, Y. P.; Sun, Y.; Yang, X.; Li, Y. P.; Han, A. J.; Wang, B. Q.; Liu, J. F. Defect-rich CoFe-layered double hydroxides as superior peroxidase-like nanozymes for the detection of ascorbic acid. *ACS Appl. Mater. Interfaces* **2023**, *15* (22), 26263-26272
(97) Zhang, S.; Chen, J.; Yang, W. S.; Chen, X. Vacancies-rich CoAl monolayer layered double hydroxide as efficient superoxide dismutase-like nanozyme. *Nano Res.* **2022**, *15* (9), 7940-7950
(98) Pavlovic, M.; Szerlauth, A.; Muráth, S.; Varga, G.; Szilagyi, I. Surface modification of two-dimensional layered double hydroxide nanoparticles with biopolymers for biomedical applications. *Adv. Drug Deliv. Rev.* **2022**, *191*, 114590
(99) Hu, T. T.; Gu, Z.; Williams, G. R.; Strimaite, M.; Zha, J. J.; Zhou, Z.; Zhang, X. C.; Tan, C. L.; Liang, R. Z. Layered double hydroxide-based nanomaterials for biomedical applications. *Chem. Soc. Rev.* **2022**, *51* (14), 6126-6176
(100) Zhang, L. X.; Hu, J.; Jia, Y. B.; Liu, R. T.; Cai, T.; Xu, Z. P. Two-dimensional layered double hydroxide nanoadjuvant: recent progress and future direction. *Nanoscale* **2021**, *13* (16), 7533-7549
(101) Chen, Y. X.; Zhu, R.; Ke, Q. F.; Gao, Y. S.; Zhang, C. Q.; Guo, Y. P. MgAl layered double hydroxide/chitosan porous scaffolds loaded with PFT alpha to promote bone regeneration. *Nanoscale* **2017**, *9* (20), 6765-6776
(102) Peng, F.; Wang, D. H.; Zhang, D. D.; Yan, B. C.; Cao, H. L.; Qiao, Y. Q.; Liu, X. Y. PEO/Mg-Zn-Al LDH composite coating on Mg alloy as a Zn/Mg ion-release platform with multifunctions: Enhanced corrosion resistance, osteogenic, and antibacterial activities. *ACS Biomater. Sci. Eng.* **2018**, *4* (12), 4112-4121
(103) Xu, C.; Lu, J. H.; Zhou, L.; Liang, J.; Fang, L.; Cao, F. Multifunctional nanocomposite eye drops of cyclodextrin complex@layered double hydroxides for relay drug delivery to the posterior segment of the eye. *Carbohydr. Polym.* **2021**, *260*,
(104) Vasti, C.; Bedoya, D. A.; Bonnet, L. V.; Ambroggio, E.; Giacomelli, C. E.; Rojas, R. Synthetic and biological identities of layered double hydroxides nanocarriers functionalized with risedronate. *Appl. Clay. Sci.* **2020**, *199*, 105880
(105) Rebitski, E. P.; Souza, G. P.; Santana, S. A. A.; Pergher, S. B. C.; Alcantara, A. C. S. Bionanocomposites based on cationic and anionic layered clays as controlled release devices of amoxicillin. *Appl. Clay. Sci.* **2019**, *173*, 35-45
(106) Li, X. Q.; Gong, P. W.; Li, Y. Z.; Yu, J. F.; Wang, F.; Li, X. A.; Fan, Z. J.; Wang, Z. F. Double-carrier drug delivery system based on polyurethane-polyvinyl alcohol/layered double hydroxide nanocomposite hydrogel. *Mater. Lett.* **2019**, *243*, 1-4
(107) Li, B. X.; He, J.; Evans, D. G.; Duan, X. Inorganic layered double hydroxides as a drug delivery system - intercalation and in vitro release of fenbufen. *Appl. Clay. Sci.* **2004**, *27* (3-4), 199-207
(108) Liu, J. P.; Wu, Y. L.; Fu, C. K.; Li, B.; Li, L.; Zhang, R.; Xu, T. F.; Xu, Z. P. Charge reversion simultaneously enhances tumor accumulation and cell uptake of layered double hydroxide nanohybrids for effective imaging and therapy. *Small* **2020**, *16* (31),
(109) Khorsandi, K.; Hosseinzadeh, R.; Shahidi, F. K. Photodynamic treatment with anionic nanoclays containing curcumin on human triple-negative breast cancer cells: Cellular and biochemical studies. *J. Cell. Biochem.* **2019**, *120* (4), 4998-5009
(110) Chakraborti, M.; Jackson, J. K.; Plackett, D.; Gilchrist, S. E.; Burt, H. M. The application of layered double hydroxide clay (LDH)-poly(lactide-co-glycolic acid) (PLGA) film composites for the controlled release of antibiotics. *J. Mater. Sci. Mater. Med.* **2012**, *23* (7), 1705-1713

(111) Yan, L.; Zhou, M. J.; Zhang, X. J.; Huang, L. B.; Chen, W.; Roy, V. A. L.; Zhang, W. J.; Chen, X. F. A novel type of aqueous dispersible ultrathin-layered double hydroxide nanosheets for in vivo bioimaging and drug delivery. *ACS Appl. Mater. Interfaces* **2017**, *9* (39), 34185-34193
(112) Chen, C. P.; Yee, L. K.; Gong, H.; Zhang, Y.; Xu, R. A facile synthesis of strong near infrared fluorescent layered double hydroxide nanovehicles with an anticancer drug for tumor optical imaging and therapy. *Nanoscale* **2013**, *5* (10), 4314-4320
(113) Murath, S.; Alsharif, N. B.; Saringer, S.; Katana, B.; Somosi, Z.; Szilagyi, I. Antioxidant materials based on 2D nanostructures: A review on recent progresses. *Crystals* **2020**, *10* (3), 148
(114) Murath, S.; Szerlauth, S.; Sebok, D.; Szilagyi, I. Layered double hydroxide nanoparticles to overcome the hydrophobicity of ellagic acid: An antioxidant hybrid material. *Antioxidants* **2020**, *9* (2), 153
(115) Zhang, Q.; Jiao, Q.; Leroux, F.; Tang, P. G.; Li, D. Q.; Feng, Y. J. Antioxidant intercalated hydrocalumite as multifunction nanofiller for Poly(propylene): Synthesis, thermal stability, light stability, and anti-migration property. *Polym. Degrad. Stab.* **2017**, *140*, 9-16
(116) Feng, Y. J.; Jiang, Y.; Huang, Q.; Chen, S. T.; Zhang, F. B.; Tang, P. G.; Li, D. Q. High antioxidative performance of layered double hydroxides/polypropylene composite with intercalation of low-molecular-weight phenolic antioxidant. *Ind. Eng. Chem. Res.* **2014**, *53* (6), 2287-2292
(117) Lonkar, S. P.; Leuteritz, A.; Heinrich, G. Antioxidant intercalated layered double hydroxides: a new multifunctional nanofiller for polymers. *RSC Adv.* **2013**, *3* (5), 1495-1501
(118) Ansy, K. M.; Lee, J. H.; Piao, H.; Choi, G.; Choy, J. H. Stabilization of antioxidant gallate in layered double hydroxide by exfoliation and reassembling reaction. *Solid State Sci.* **2018**, *80*, 65-71
(119) Lima, E.; Flores, J.; Cruz, A. S.; Leyva-Gomez, G.; Krotzsch, E. Controlled release of ferulic acid from a hybrid hydrotalcite and its application as an antioxidant for human fibroblasts. *Microporous and Mesoporous Materials* **2013**, *181*, 1-7
(120) Silion, M.; Hritcu, D.; Lisa, G.; Popa, M. I. New hybrid materials based on layered double hydroxides and antioxidant compounds. Preparation, characterization and release kinetic studies. *J. Porous Mat.* **2012**, *19* (3), 267-276
(121) Baek, M.; Choy, J. H.; Choi, S. J. Montmorillonite intercalated with glutathione for antioxidant delivery: Synthesis, characterization, and bioavailability evaluation. *Int. J. Pharm.* **2012**, *425* (1-2), 29-34
(122) Sakr, O. S.; Borchard, G. Encapsulation of enzymes in layer-by-layer (LbL) structures: Latest advances and applications. *Biomacromolecules* **2013**, *14* (7), 2117-2135
(123) Caruso, F.; Schuler, C. Enzyme multilayers on colloid particles: Assembly, stability, and enzymatic activity. *Langmuir* **2000**, *16* (24), 9595-9603
(124) Caruso, F.; Caruso, R. A.; Mohwald, H. Nanoengineering of inorganic and hybrid hollow spheres by colloidal templating. *Science* **1998**, *282* (5391), 1111-1114
(125) Pavlovic, M.; Rouster, P.; Somosi, Z.; Szilagyi, I. Horseradish peroxidase-nanoclay hybrid particles of high functional and colloidal stability. *J. Colloid Interface Sci.* **2018**, *524*, 114-121
(126) Pavlovic, M.; Rouster, P.; Szilagyi, I. Synthesis and formulation of functional bionanomaterials with superoxide dismutase activity. *Nanoscale* **2017**, *9* (1), 369-379
(127) Pavlovic, M.; Murath, S.; Katona, X.; Alsharif, N. B.; Rouster, P.; Maleth, J.; Szilagyi, I. Nanocomposite-based dual enzyme system for broad-spectrum scavenging of reactive oxygen species. *Sci. Rep.* **2021**, *11* (1), 4321
(128) Lavery, C. B.; MacInnis, M. C.; MacDonald, M. J.; Williams, J. B.; Spencer, C. A.; Burke, A. A.; Irwin, D. J. G.; D'Cunha, G. B. Purification of peroxidase from horseradish (Armoracia rusticana) roots. *J. Agric. Food Chem.* **2010**, *58* (15), 8471-8476
(129) Grosu, E. F.; Froidevaux, R.; Carja, G. Horseradish peroxidase-AuNP/LDH heterostructures: influence on nanogold release and enzyme activity. *Gold Bull.* **2019**, *52* (2), 87-97
(130) Zandieh, M.; Liu, J. W. Nanozymes: Definition, activity, and mechanisms. *Adv. Mater.* **2023**, 2211041
(131) Zhang, R. F.; Yan, X. Y.; Fan, K. L. Nanozymes inspired by natural enzymes. *Accounts Mater. Res.* **2021**, *2* (7), 534-547
(132) Wu, J. J. X.; Wang, X. Y.; Wang, Q.; Lou, Z. P.; Li, S. R.; Zhu, Y. Y.; Qin, L.; Wei, H. Nanomaterials with enzyme-like characteristics (nanozymes): next-generation artificial enzymes (II). *Chem. Soc. Rev.* **2019**, *48* (4), 1004-1076

(133) Zhang, C. Y.; Nan, Z. D. Improvement of Fe0.8Ni0.2S2 peroxidase-like activity through the accelerated conversion from Fe^{3+} to Fe^{2+}. *J. Phys. Chem. C* **2022**, *126* (9), 4355-4364
(134) Sun, Z. C.; Yao, J. J.; Wang, J. D.; Huang, R. J.; Liu, X. L.; Li, F.; Jiang, X. Y.; Chen, W. W. Room-temperature harvesting oxidase-mimicking enzymes with exogenous ROS generation in one step. *Inorg. Chem.* **2022**, *61* (2), 1169-1177
(135) Zeng, J. Y.; Ding, C. P.; Chen, L.; Yang, B.; Li, M.; Wang, X. Y.; Su, F. M.; Liu, C. T.; Huang, Y. J. Multienzyme-mimicking Au@Cu_2O with complete antioxidant capacity for reactive oxygen species scavenging. *ACS Appl. Mater. Interfaces* **2023**, *15* (1), 378-390
(136) Alsharif, N. B.; Samu, G. F.; Saringer, S.; Szerlauth, A.; Takacs, D.; Hornok, V.; Dékány, I.; Szilagyi, I. Antioxidant colloids via heteroaggregation of cerium oxide nanoparticles and latex beads. *Colloids Surf. B* **2022**, *216*, 112531
(137) Yang, X. T.; Cao, X.; Fu, Y.; Lu, J.; Ma, X. T.; Li, R.; Guan, S. Y.; Zhou, S. Y.; Qu, X. Z. Layered double hydroxide-based nanozyme for NO-boost multi-enzyme dynamic therapy with tumor specificity. *J. Mat. Chem. B* **2023**, *11* (7), 1591-1598
(138) Wang, B. Q.; Fang, Y. Y.; Han, X.; Jiang, R. T.; Zhao, L.; Yang, X.; Jin, J.; Han, A. J.; Liu, J. F. Atomization-induced high intrinsic activity of a biocompatible MgAl-LDH supported Ru single-atom nanozyme for efficient radicals scavenging. *Angew. Chem. Int. Edit.* **2023**, e202307133
(139) Su, L.; Yu, X. A.; Miao, Y. Q.; Mao, G. J.; Dong, W. P.; Feng, S. L.; Liu, S. M.; Yang, L. K.; Zhang, K. G.; Zhang, H. Alkaline-promoted regulation of the peroxidase-like activity of Ni/Co LDHs and development bioassays. *Talanta* **2019**, *197*, 181-188
(140) Xu, X. C.; Zou, X. B.; Wu, S. W.; Wang, L. J.; Niu, X. H.; Li, X.; Pan, J. M.; Zhao, H. L.; Lan, M. B. In situ formation of fluorescent polydopamine catalyzed by peroxidase-mimicking FeCo-LDH for pyrophosphate ion and pyrophosphatase activity detection. *Anal. Chim. Acta* **2019**, *1053*, 89-97
(141) Evans, D. F.; Wennerstrom, H. *The colloidal domain*; John Wiley, 1999.
(142) Russel, W. B.; Saville, D. A.; Schowalter, W. R. *Colloidal dispersions*; Cambridge University Press, 1989.
(143) Horikoshi, S.; Serpone, N. Introduction to nanoparticles. In *Microwaves in nanoparticle synthesis: Fundamentals and applications*, Horikoshi, S., Serpone, N. Eds.; Wiley-VCH, 2013; pp 1-24.
(144) Lee, M. S.; Yee, D. W.; Ye, M.; Macfarlane, R. J. Nanoparticle assembly as a materials development tool. *J. Am. Chem. Soc.* **2022**, *144* (8), 3330-3346
(145) Muramatsu, H.; Lam, K.; Bajusz, C.; Laczkó, D.; Karikó, K.; Schreiner, P.; Martin, A.; Lutwyche, P.; Heyes, J.; Pardi, N. Lyophilization provides long-term stability for a lipid nanoparticle-formulated , nucleoside-modified mRNA vaccine. *Mol. Ther.* **2022**, *30* (5), 1941-1951
(146) Derjaguin, B.; Landau, L. D. Theory of the stability of strongly charged lyophobic sols and of the adhesion of strongly charged particles in solutions of electrolytes. *Acta Phys. Chim.* **1941**, *14* (6), 633-662
(147) Verwey, E. J. W.; Overbeek, J. T. G. *Theory of stability of lyophobic colloids*; Elsevier, 1948.
(148) Wall, S. The history of electrokinetic phenomena. *Curr. Opin. Colloid Interface Sci.* **2010**, *15* (3), 119-124
(149) Liang, Y.; Hilal, N.; Langston, P.; Starov, V. Interaction forces between colloidal particles in liquid: Theory and experiment. *Adv. Colloid Interface Sci.* **2007**, *134-35*, 151-166
(150) Delgado, A. V.; Gonzalez-Caballero, F.; Hunter, R. J.; Koopal, L. K.; Lyklema, J. Measurement and interpretation of electrokinetic phenomena. *J. Colloid Interface Sci.* **2007**, *309* (2), 194-224
(151) Elimelech, M.; Gregory, J.; Jia, X.; Williams, R. A. *Particle deposition and aggregation: Measurement, modeling, and simulation*; Butterworth-Heinemann Ltd., 1995.
(152) Israelachvili, J. *Intermolecular and surface forces*; Academic Press, 2011.
(153) Szilagyi, I.; Trefalt, G.; Tiraferri, A.; Maroni, P.; Borkovec, M. Polyelectrolyte adsorption, interparticle forces, and colloidal aggregation. *Soft Matter* **2014**, *10* (15), 2479-2502
(154) Dautzenberg, H.; Jaeger, W.; Kotz, J.; Philipp, B.; Seidel, C.; Stscherbina, D. *Polyelectrolytes: Formation, characterization and application*; Hanser Publishers, 1994.
(155) Borkovec, M.; Papastavrou, G. Interactions between solid surfaces with adsorbed polyelectrolytes of opposite charge. *Curr. Opin. Colloid Interface Sci.* **2008**, *13* (6), 429-437
(156) Szerlauth, A.; Murath, S.; Szilagyi, I. Layered double hydroxide-based antioxidant dispersions with high colloidal and functional stability. *Soft Matter* **2020**, *16* (46), 10518-10527

(157) Fritz, G.; Schadler, V.; Willenbacher, N.; Wagner, N. J. Electrosteric stabilization of colloidal dispersions. *Langmuir* **2002**, *18* (16), 6381-6390
(158) Saringer, S.; Rouster, P.; Szilagyi, I. Regulation of the stability of titania nanosheet dispersions with oppositely and like-charged polyelectrolytes. *Langmuir* **2019**, *35* (14), 4986-4994
(159) Pavlovic, M.; Li, L.; Dits, F.; Gu, Z.; Adok-Sipiczki, M.; Szilagyi, I. Aggregation of layered double hydroxide nanoparticles in the presence of heparin: Towards highly stable delivery systems. *RSC Adv.* **2016**, *6*, 16159-16167
(160) Somosi, Z.; Pavlovic, M.; Palinko, I.; Szilagyi, I. Effect of polyelectrolyte mono- and bilayer formation on the colloidal stability of layered double hydroxide nanoparticles. *Nanomaterials* **2018**, *8* (12), 986
(161) Gu, Z.; Zuo, H. L.; Li, L.; Wu, A. H.; Xu, Z. P. Pre-coating layered double hydroxide nanoparticles with albumin to improve colloidal stability and cellular uptake. *J. Mat. Chem. B* **2015**, *3* (16), 3331-3339
(162) Vasti, C.; Bedoya, D. A.; Rojas, R.; Giacomelli, C. E. Effect of the protein corona on the colloidal stability and reactivity of LDH-based nanocarriers. *J. Mat. Chem. B* **2016**, *4* (11), 2008-2016
(163) Kang, H. L.; Shu, Y.; Li, Z.; Guan, B.; Peng, S. J.; Huang, Y.; Liu, R. G. An effect of alginate on the stability of LDH nanosheets in aqueous solution and preparation of alginate/LDH nanocomposites. *Carbohydr. Polym.* **2014**, *100*, 158-165
(164) Szerlauth, A.; Kónya, Z. D.; Papp, G.; Kónya, Z.; Kukovecz, Á.; Szabados, M.; Varga, G.; Szilágyi, I. Molecular orientation rules the efficiency of immobilized antioxidants. *J. Colloid Interface Sci.* **2023**, *632*, 260-270
(165) Hassan, P. A.; Rana, S.; Verma, G. Making sense of Brownian motion: Colloid characterization by dynamic light scattering. *Langmuir* **2015**, *31* (1), 3-12
(166) Trefalt, G.; Szilagyi, I.; Oncsik, T.; Sadeghpour, A.; Borkovec, M. Probing colloidal particle aggregation by light scattering. *Chimia* **2013**, *67* (11), 772-776
(167) Brand-Williams, W.; Cuvelier, M. E.; Berset, C. Use of a free-radical method to evaluate antioxidant activity. *Food Sci. Technol. Lebensm. Wiss. Technol.* **1995**, *28* (1), 25-30
(168) Beaucham, C.; Fridovich, I. Superoxide dismutase - improved assays and an assay applicable to acrylamide gels. *Anal. Biochem.* **1971**, *44* (1), 276-287
(169) Maehly, A. C.; Chance, B. The assay of catalases and peroxidases. *Methods. Biochem. Anal.* **1954**, *1*, 357-424
(170) Johnson, K. A.; Goody, R. S. The original Michaelis constant: Translation of the 1913 Michaelis-Menten paper. *Biochemistry* **2011**, *50* (39), 8264-8269
(171) Hadwan, M. H.; Abed, H. N. Data supporting the spectrophotometric method for the estimation of catalase activity. *Data Brief* **2016**, *6*, 194-199
(172) Bragg, W. H.; Bragg, W. L. The reflection of X-rays by crystals. *Proc. R. soc. Lond. Ser. A-Contain. Pap. Math. Phys. Character* **1913**, *88* (605), 428-438
(173) Blanchet, C. E.; Spilotros, A.; Schwemmer, F.; Graewert, M. A.; Kikhney, A.; Jeffries, C. M.; Franke, D.; Mark, D.; Zengerle, R.; Cipriani, F.; et al. Versatile sample environments and automation for biological solution X-ray scattering experiments at the P12 beamline (PETRA III, DESY). *J. Appl. Crystallogr.* **2015**, *48*, 431-443
(174) Li, Z. H.; Sun, J. H.; Wu, D.; Sun, Y. H.; Liu, Y.; Sheng, W. J.; Dong, B. Z. Determination of specific surfaces of silica xerogels by SAXS. *Chin. Sci. Bull.* **2000**, *45* (15), 1386-1390
(175) Li, Z. H.; Gong, Y. J.; Wu, D.; Sun, Y. H.; Wang, J.; Liu, Y.; Dong, B. Z. A negative deviation from Porod's law in SAXS of organo-MSU-X. *Microporous and Mesoporous Materials* **2001**, *46* (1), 75-80
(176) Fairley, N.; Fernandez, V.; Richard-Plouet, M.; Guillot-Deudon, C.; Walton, J.; Smith, E.; Flahaut, D.; Greiner, M.; Biesinger, M.; Tougaard, S.; et al. Systematic and collaborative approach to problem solving using X-ray photoelectron spectroscopy. *Appl. Surf. Sci. Adv.* **2021**, *5*, 100112
(177) Molnar, R.; Madacsy, T.; Varga, A.; Nemeth, M.; Katona, X.; Gorog, M.; Molnar, B.; Fanczal, J.; Rakonczay, Z.; Hegyi, P.; et al. Mouse pancreatic ductal organoid culture as a relevant model to study exocrine pancreatic ion secretion. *Lab. Invest.* **2020**, *100* (1), 84-97

(178) Szerlauth, A.; Balog, E.; Takács, D.; Sáringer, S.; Varga, G.; Schuszter, G.; Szilagyi, I. Self-assembly of delaminated layered double hydroxide nanosheets for the recovery of lamellar structure. *Colloid Interface Sci. Commun.* **2022**, *46*, 100564
(179) Li, L.; Gu, Z.; Gu, W. Y.; Xu, Z. P. Direct synthesis of layered double hydroxide nanosheets for efficient siRNA delivery. *RSC Adv.* **2016**, *6* (98), 95518-95526
(180) Janovak, L.; Deak, A.; Tallosy, S. P.; Sebok, D.; Csapo, E.; Bohinc, K.; Abram, A.; Palinko, I.; Dekany, I. Hydroxyapatite-enhanced structural, photocatalytic and antibacterial properties of photoreactive TiO2/HAp/polyacrylate hybrid thin films. *Surf. Coat. Technol.* **2017**, *326*, 316-326
(181) Szerlauth, A.; Varga, Á.; Madácsy, T.; Sebők, D.; Bashiri, S.; Skwarczynski, M.; Toth, I.; Maléth, J.; Szilagyi, I. Confinement of triple-enzyme-involved antioxidant cascade in two-dimensional nanostructure. *ACS Mater. Lett.* **2023**, *5* (2), 565-573
(182) Wang, Q.; O'Hare, D. Large-scale synthesis of highly dispersed layered double hydroxide powders containing delaminated single layer nanosheets. *Chem. Commun.* **2013**, *49* (56), 6301-6303
(183) Pavlovic, M.; Rouster, P.; Oncsik, T.; Szilagyi, I. Tuning colloidal stability of layered double hydroxides: from monovalent ions to polyelectrolytes. *ChemPlusChem* **2017**, *82*, 121-131
(184) Chen, C. P.; Wangriya, A.; Buffet, J. C.; O'Hare, D. Tuneable ultra high specific surface area Mg/Al-CO_3 layered double hydroxides. *Dalton Transactions* **2015**, *44* (37), 16392-16398
(185) Pavlovic, M.; Huber, R.; Adok-Sipiczki, M.; Nardin, C.; Szilagyi, I. Ion specific effects on the stability of layered double hydroxide colloids. *Soft Matter* **2016**, *12*, 4024-4033
(186) Pavlovic, M.; Nafradi, B.; Rouster, P.; Murath, S.; Szilagyi, I. Highly stable enzyme-mimicking nanocomposite of antioxidant activity. *J. Colloid Interface Sci.* **2019**, *543*, 174-182
(187) Wu, Q. L.; Sjastad, A. O.; Vistad, O. B.; Knudsen, K. D.; Roots, J.; Pedersen, J. S.; Norby, P. Characterization of exfoliated layered double hydroxide (LDH, Mg/Al=3) nanosheets at high concentrations in formamide. *J. Mater. Chem.* **2007**, *17* (10), 965-971
(188) Chang, F. P.; Chen, Y. P.; Mou, C. Y. Intracellular implantation of enzymes in hollow silica nanospheres for protein therapy: Cascade system of Superoxide Dismutase and Catalase. *Small* **2014**, *10* (22), 4785-4795
(189) Zhang, S. H.; Jiang, Z. Y.; Zhanga, W. Y.; Wang, X. L.; Shi, J. F. Polymer-inorganic microcapsules fabricated by combining biomimetic adhesion and bioinspired mineralization and their use for catalase immobilization. *Biochem. Eng. J.* **2015**, *93*, 281-288
(190) Pallagi, P.; Gorog, M.; Papp, N.; Madacsy, T.; Varga, A.; Crul, T.; Szabo, V.; Molnar, M.; Dudas, K.; Grassalkovich, A.; et al. Bile acid- and ethanol-mediated activation of Orai1 damages pancreatic ductal secretion in acute pancreatitis. *J. Physiol.-London* **2022**, *600* (7), 1631-1650
(191) Loor, G.; Kondapalli, J.; Schriewer, J. M.; Chandel, N. S.; Vanden Hoek, T. L.; Schumacker, P. T. Menadione triggers cell death through ROS-dependent mechanisms involving PARP activation without requiring apoptosis. *Free Radic. Biol. Med.* **2010**, *49* (12), 1925-1936
(192) Georgoulis, A.; Vorgias, C. E.; Chrousos, G. P.; Rogakou, E. P. Genome instability and gamma H2AX. *Int. J. Mol. Sci.* **2017**, *18* (9), 10
(193) Yuan, J. S.; Adamski, R.; Chen, J. J. Focus on histone variant H2AX: To be or not to be. *FEBS Lett.* **2010**, *584* (17), 3717-3724
(194) Noubissi, F. K.; McBride, A. A.; Leppert, H. G.; Millet, L. J.; Wang, X. F.; Davern, S. M. Detection and quantification of gamma-H2AX using a dissociation enhanced lanthanide fluorescence immunoassay. *Sci. Rep.* **2021**, *11* (1), 8945
(195) Aramendia, M. A.; Borau, V.; Jimenez, U.; Marinas, J. M.; Ruiz, J. R.; Urbano, F. J. Comparative study of Mg/M(III) (M = Al, Ga, In) layered double hydroxides obtained by coprecipitation and the sol-gel method. *J. Solid State Chem.* **2002**, *168* (1), 156-161
(196) Liang, X.; Cao, K. X.; Li, W.; Li, X. Q.; McClements, D. J.; Hu, K. Tannic acid-fortified zein-pectin nanoparticles: Stability, properties, antioxidant activity, and in vitro digestion. *Food Res. Int.* **2021**, *145*, 110425
(197) Aromal, S. A.; Philip, D. Facile one-pot synthesis of gold nanoparticles using tannic acid and its application in catalysis. *Physica E* **2012**, *44* (7-8), 1692-1696
(198) Cumberland, S. L.; Strouse, G. F. Analysis of the nature of oxyanion adsorption on gold nanomaterial surfaces. *Langmuir* **2002**, *18* (1), 269-276

(199) Evans, S. D.; Urankar, E.; Ulman, A.; Ferris, N. Self-assembled monolayers of alkenthils containing a polar aromatic group - Effects of the dipole position on molecular packing, orientation, and surface wetting properties. *J. Am. Chem. Soc.* **1991**, *113* (11), 4121-4131
(200) Ghigo, G.; Berto, S.; Minella, M.; Vione, D.; Alladio, E.; Nurchi, V. M.; Lachowicz, J.; Daniele, P. G. New insights into the protogenic and spectroscopic properties of commercial tannic acid: the role of gallic acid impurities. *New J. Chem.* **2018**, *42* (10), 7703-7712
(201) Mazurek, S.; Fecka, I.; Weglinska, M.; Szostak, R. Quantification of active ingredients in Potentilla tormentilla by Raman and infrared spectroscopy. *Talanta* **2018**, *189*, 308-314
(202) Catalini, S.; Rossi, B.; Foggi, P.; Masciovecchio, C.; Bruni, F. Aqueous solvation of glutathione probed by UV resonance Raman spectroscopy. *J. Mol. Liq.* **2019**, *283*, 537-547
(203) Bazylewski, P.; Divigalpitiya, R.; Fanchini, G. In situ Raman spectroscopy distinguishes between reversible and irreversible thiol modifications in L-cysteine. *RSC Adv.* **2017**, *7* (5), 2964-2970
(204) Larsson, M.; Lindgren, J. Analysis of glutathione and immunoglobulin G inside chromatographic beads using surface-enhanced Raman scattering spectroscopy. *J. Raman Spectrosc.* **2005**, *36* (5), 394-399
(205) Kwon, C. K.; Kim, M. S.; Kim, K. Raman-spectroscopy of cyclohexanethiol adsorbed on a silver surface. *J. Raman Spectrosc.* **1989**, *20* (9), 575-580
(206) Frost, R. L.; Spratt, H. J.; Palmer, S. J. Infrared and near-infrared spectroscopic study of synthetic hydrotalcites with variable divalent/trivalent cationic ratios. *Spectroc. Acta Pt. A Molec. Biomolec. Spectr.* **2009**, *72* (5), 984-988
(207) Mora, M.; López, M. I.; Jiménez-Sanchidrián, C.; Ruiz, J. R. MIR and NIR spectroscopy of sol-gel hydrotalcites with various trivalent cations. *J. Sol-Gel Sci. Technol.* **2010**, *55* (1), 59-65
(208) Frost, R. L.; Erickson, K. L. Near-infrared spectroscopy of stitchtite, iowaite, desautelsite and arsenate exchanged takovite and hydrotalcite. *Spectroc. Acta Pt. A Molec. Biomolec. Spectr.* **2005**, *61* (1-2), 51-56
(209) Mora, M.; López, M. I.; Jiménez-Sanchidrián, C.; Ruiz, J. R. Study of organo-hybrid layered double hydroxides by medium and near infrared spectroscopy. *Spectroc. Acta Pt. A Molec. Biomolec. Spectr.* **2011**, *78* (3), 989-995
(210) Frost, R. L.; Ding, Z.; Kloprogge, J. T. The application of near-infrared spectroscopy to the study of brucite and hydrotalcite structure. *Can. J. Anal. Sci. Spectrosc.* **2000**, *45* (4), 96-102
(211) Zheng, X. F.; Duan, C.; Shen, J. T.; Duan, X. H. Determination of reduced glutathione by spectrophotometry coupled with anti-interference compensation. *Anal. Methods* **2015**, *7* (12), 5006-5011
(212) Kalaiyarasan, G.; Kumar, A. V. N.; Sivakumar, C.; Joseph, J. Electro-generated reactive oxygen species at Au surface as an indicator to explore glutathione redox chemistry and quantification. *Electrochem. Commun.* **2015**, *56*, 29-33
(213) Huang, X.; Chen, J.; Yu, H.; Peng, S. J.; Cai, R.; Yan, Q. Y.; Hng, H. H. Immobilization of plant polyphenol stabilized-Sn nanoparticles onto carbon nanotubes and their application in rechargeable lithium ion batteries. *RSC Adv.* **2013**, *3* (16), 5310-5313
(214) Stevens, R.; Stevens, L.; Price, N. C. The stabilities of various thiol compounds used in protein purifications. *Biochem. Educ.* **1983**, *11* (2), 70-70
(215) Aruga, M.; Awazu, S.; Hanano, M. Kinetic studies on decomposition of glutathione 1. Decomposition in solid-state. *Chem. Pharm. Bull.* **1978**, *26* (7), 2081-2091
(216) Wu, J. S.; Xiao, Y. K.; Wan, J. Y.; Wen, L. R. The growth mechanism of hydrotalcite crystal. *Sci. China Technol. Sci.* **2012**, *55* (4), 872-878
(217) Biesinger, M. C. Advanced analysis of copper X-ray photoelectron spectra. *Surf. Interface Anal.* **2017**, *49* (13), 1325-1334
(218) Li, B.; Tang, J.; Chen, W. Y.; Hao, G. Y.; Kurniawan, N.; Gu, Z.; Xu, Z. P. Novel theranostic nanoplatform for complete mice tumor elimination via MR imaging-guided acid-enhanced photothermo-/chemo-therapy. *Biomaterials* **2018**, *177*, 40-51
(219) Zhang, G.; Wu, L.; Tang, A. T.; Weng, B.; Atrens, A.; Ma, S. D.; Liu, L.; Pan, F. S. Sealing of anodized magnesium alloy AZ31 with MgAl layered double hydroxides layers. *RSC Adv.* **2018**, *8* (5), 2248-2259

(220) Xu, K. L.; Zhang, Z.; Chen, G. M.; Shen, J. Q. Photoluminescence of colloids of pristine MgAl layered double hydroxides. *RSC Adv.* **2014**, *4* (37), 19218-19220
(221) Zhang, Z.; Chen, G. M.; Xu, K. L. Photoluminescence of colloids of pristine ZnAl layered double hydroxides. *Ind. Eng. Chem. Res.* **2013**, *52* (32), 11045-11049
(222) Tian, R.; Yan, D.; Wei, M. Layered double hydroxide materials: Assembly and photofunctionality. In *Photofunctional Layered Materials*, Yan, D., Wei, M. Eds.; Springer International Publishing, 2015; pp 1-68.
(223) Palmer, S. J.; Nguyen, T.; Frost, R. L. Synthesis and Raman spectroscopic characterisation of hydrotalcite with CO_3^{2-} and VO_3^- anions in the interlayer. *J. Raman Spectrosc.* **2007**, *38* (12), 1602-1608
(224) Dou, L. G.; Zhang, H. Facile assembly of nanosheet array-like CuMgAl-layered double hydroxide/rGO nanohybrids for highly efficient reduction of 4-nitrophenol. *J. Mater. Chem. A* **2016**, *4* (48), 18990-19002
(225) Zhang, Y.; Chen, L. X.; Sun, R. M.; Lv, R. J.; Du, T.; Li, Y. H.; Zhang, X. M.; Sheng, R. T.; Qi, Y. F. Multienzymatic antioxidant activity of manganese-based nanoparticles for protection against oxidative cell damage. *ACS Biomater. Sci. Eng.* **2022**, *8* (2), 638-648
(226) Liu, X. Y.; Li, D. X.; Liang, Y.; Lin, Y.; Liu, Z. X.; Niu, H. T.; Xu, Y. H. Establishment of anti-oxidation platform based on few-layer molybdenum disulfide nanosheet-coated titanium dioxide nanobelt nanocomposite. *J. Colloid Interface Sci.* **2021**, *601*, 167-176

10. Supplementary Information

Table S1. IR bands and their assignment for TA containing samples.

Wavenumber (cm^{-1})	Assignment	Sample
1178		TA
1195	ν(C-H)	LDH/TA/a
1202		LDH/TA/c
1308, 1335, 1380		TA
1308	δ(O-H)	LDH/TA/a
1308		LDH/TA/c
1356		LDH
1350	ν(NO_3^-)	LDH/TA/a
1355		LDH/TA/c
1443		TA
1443, 1500	δ(C-O-H)	LDH/TA/a
1496		LDH/TA/c
1513, 1534, 1605		TA
1605	ν(C=C)	LDH/TA/a
1577, 1640		LDH/TA/c
1700		TA
1692	ν(C=O)	LDH/TA/a
1692		LDH/TA/c

Table S2. Raman shifts and their assignments for TA containing samples.

Raman shift (cm^{-1})	**Assignment**	**Sample**
550	ν(M-O-M)	LDH
900 - 1200	ν(C-C), ν(C-O), ν(C-OH),	TA, LDH/TA/a, LDH/TA/c
1050	ν(NO_3^-)	LDH
1347	δ(O-H)	TA
1353		LDH/TA/a
1351		LDH/TA/c
1612	ν(C=C)	TA
1599		LDH/TA/a
1587		LDH/TA/c
1710	ν(C=O)	TA
1695		LDH/TA/a
1675		LDH/TA/c

Table S3. IR peaks and their assignment for GSH containing samples

Wavenumber (cm^{-1})	**Assignment**	**Sample**
1238, 1306	Amide III	GSH/NaOH
1251, 1312		LDH/GSH/c
1356	$\nu(NO_3^-)$	LDH
1358		LDH/GSH/a
1347		LDH/GSH/c
1393	$\nu(COO^-)$	GSH/NaOH
1393		LDH/GSH/a
1387		LDH/GSH/c
1533	Amide II	GSH
1512		GSH/NaOH
1528		LDH/GSH/a
1527		LDH/GSH/c
1592	$\delta(NH_3^+)$	GSH
1588		LDH/GSH/a
1579	$\delta(NH_2)$	GSH/NaOH
1580		LDH/GSH/c
1658	Amide I	GSH
1650		GSH/NaOH
1648		LDH/GSH/a
1643		LDH/GSH/c
2523	$\nu(SH)$	GSH

Table S4. Raman bands and their assignment for GSH containing samples

Raman shift (cm^{-1})	**Assignment**	**Sample**
219, 297	$\nu(S^-)$	LDH/GSH/a
235, 310		LDH/GSH/c
1050	$\nu(NO_3^-)$	LDH
1048		LDH/GSH/a
1047		LDH/GSH/c
1254, 1281, 1309, 1336, 1366	Amide III	GSH
1246, 1302		GSH/NaOH
1249, 1333		LDH/GSH/a
1245, 1322		LDH/GSH/c
1399	Amide S	GSH
1420		GSH/NaOH
1414		LDH/GSH/a
1414		LDH/GSH/c
1536	Amide II	GSH
1532, 1595		GSH/NaOH
1520, 1600		LDH/GSH/a
1528, 1593		LDH/GSH/c
1630, 1659	Amide I	GSH
1659		GSH/NaOH
1661		LDH/GSH/a
1657		LDH/GSH/c
2524	$\nu(SH)$	GSH
2567		GSH/NaOH

Table S5. Binding energies of Cu $2p_{3/2}$ region of XPS spectrum.

Sample	*Cu(I) 2p3/2* / eV	*Cu(II) 2p3/2* / eV
MA	-	- - - -
CMA1	931.75	934.40 939.03 941.93 943.85
CMA2	931.75	934.39 939.02 941.92 943.85
CMA3	931.71	934.31 938.94 941.84 943.76
Reference[217]	932.18	934.67 939.30 942.20 944.12

Table S6. Binding energies of Mg 2p and Al 2p regions of XPS spectrum.

Sample	*Mg(II) 2p* / eV	*A(III) 2p* / eV
MA	49.72	74.30
CMA1	49.67	74.23
CMA2	49.67	74.13
CMA3	49.62	74.06
Reference[219]	49.4	74.0

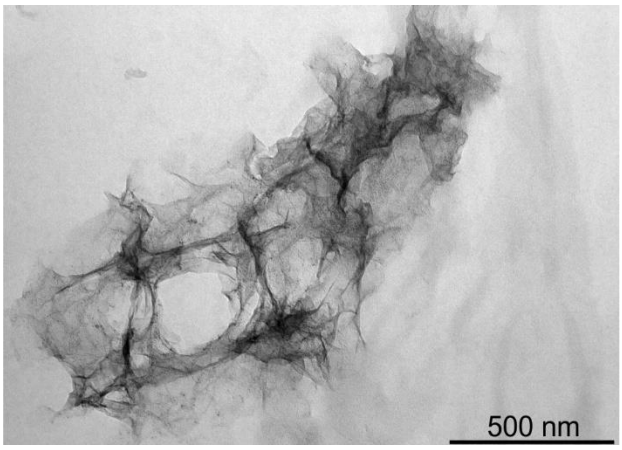

Figure S1. TEM micrograph of aggregated LDH particles 20 minutes after maintaining the 30 mM NaCl concentration.

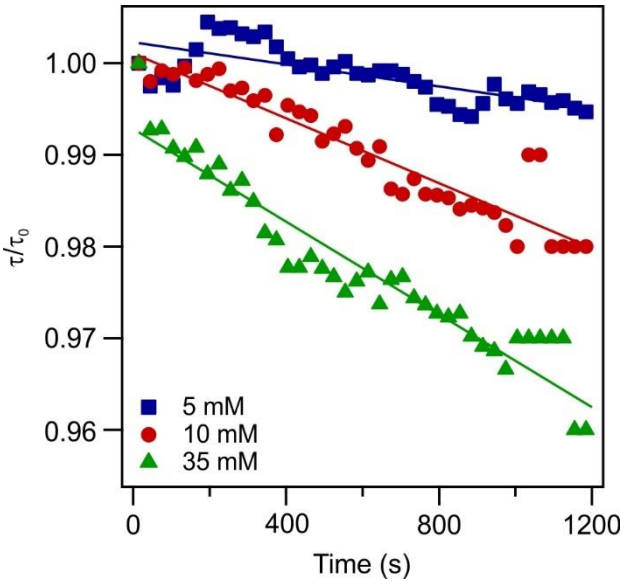

Figure S2. Change in relative turbidity values in time. The particle concentration during this measurement was set to 50 mg/L.

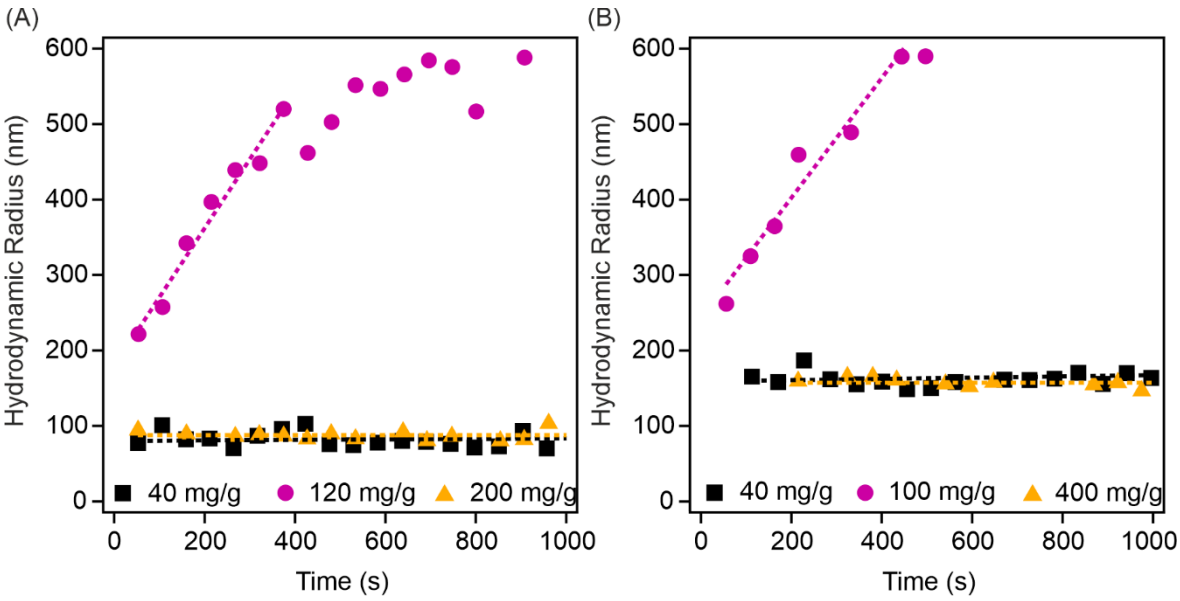

Figure S3. Change in hydrodynamic radius in time at different Alg (A) and TMC (B) doses.

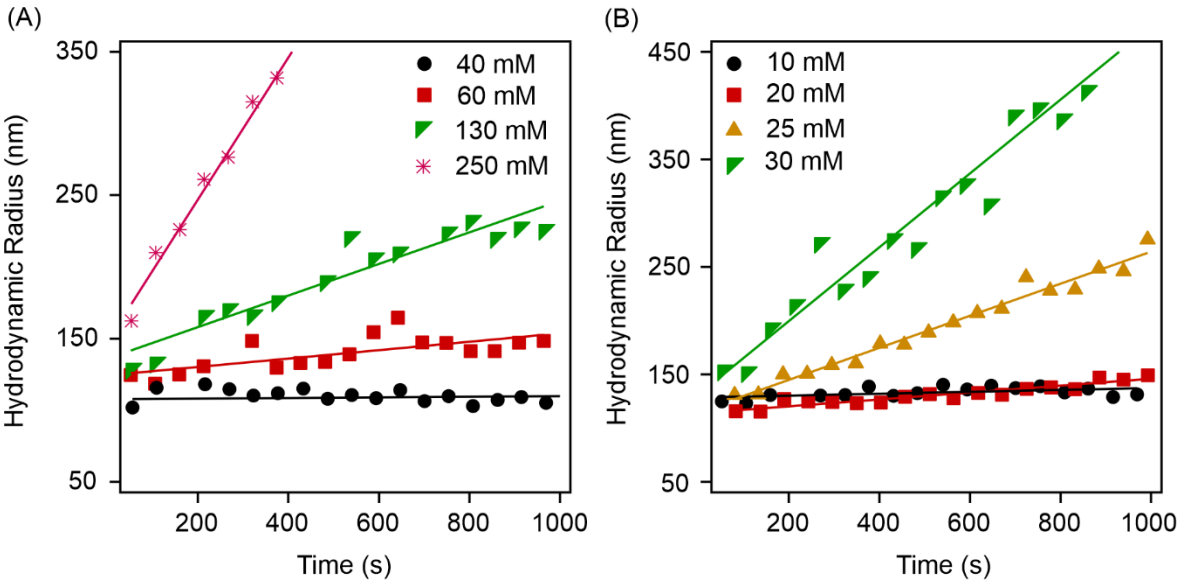

Figure S4. Change in hydrodynamic radius in time at different salt concentrations for dLDH/Alg (A) and dLDH/ALG/TMC (B) systems.

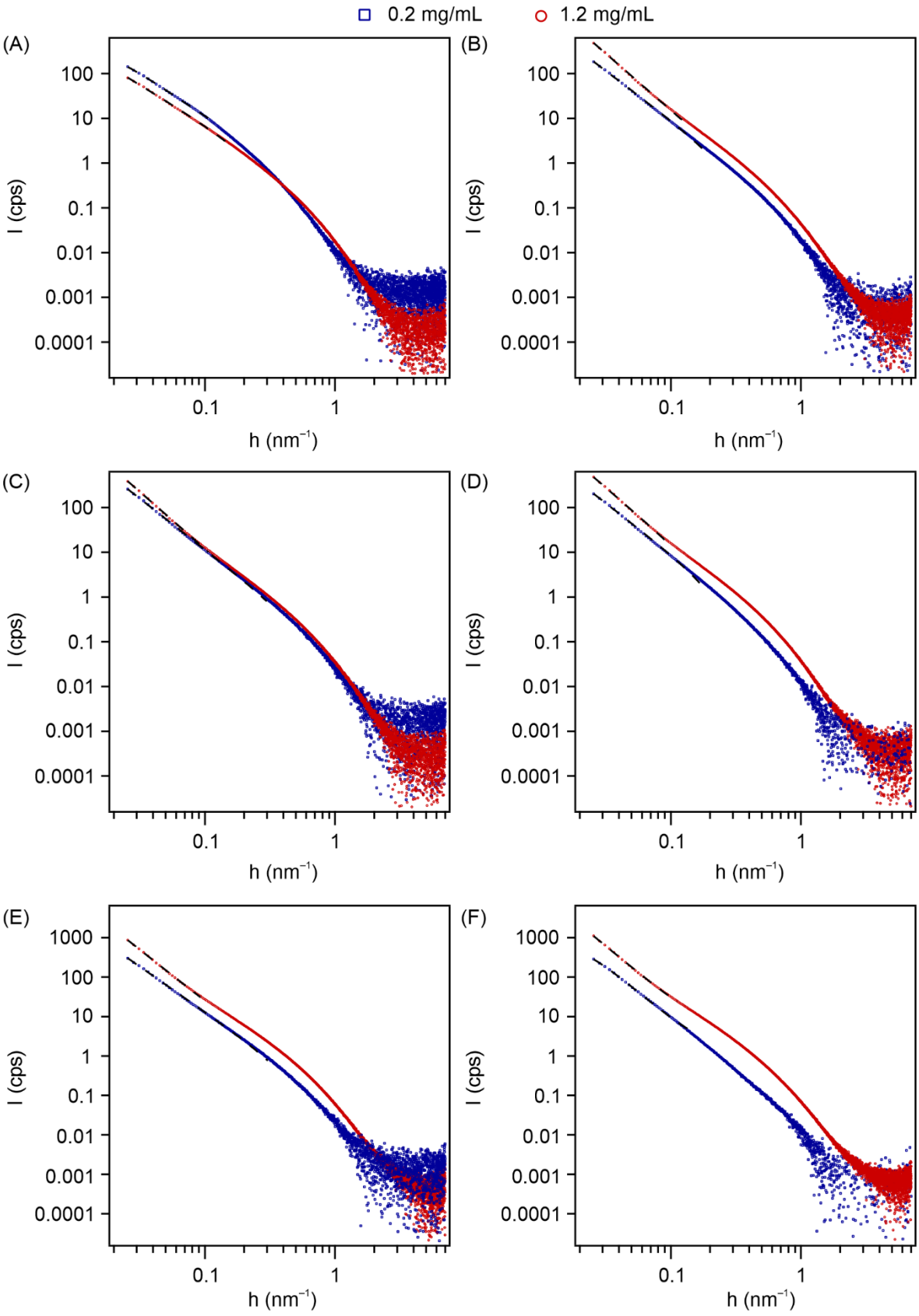

Figure S5. The SAXS scattering curves of dLDH (A), dLDHa (B), dLDHaH (C), dLDHaHt (D), dLDHaHtS (E), and dLDHaHtSC (F) samples at 0.2 mg/L and 1.2 mg/L.

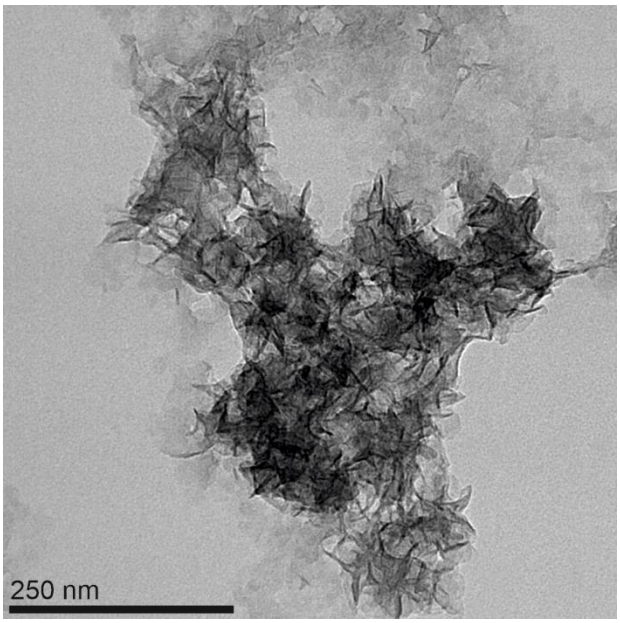

Figure S6. TEM image of dLDHaHtSC composite.

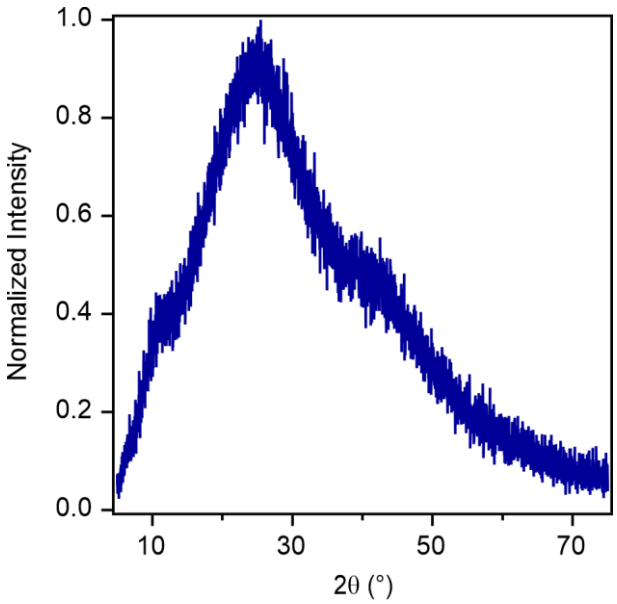

Figure S7. XRD diffractogram of LDH/TA at 1:1 Al^{3+}:TA ratio.

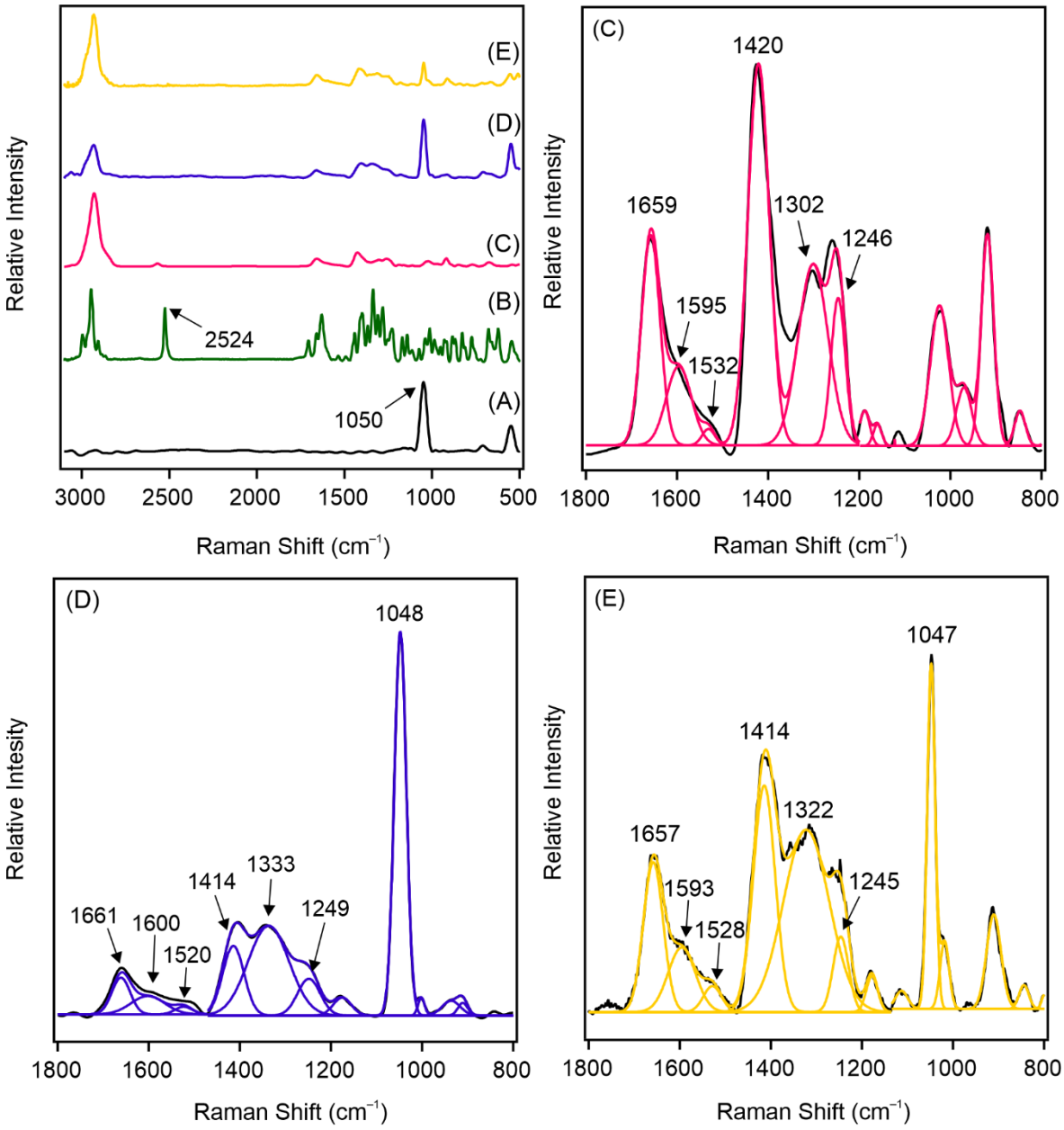

Figure S8. Raman spectra of LDH (A), GSH (B), GSH/NaOH (C), LDH/GSH/a (D) and LDH/GSH/c (E).

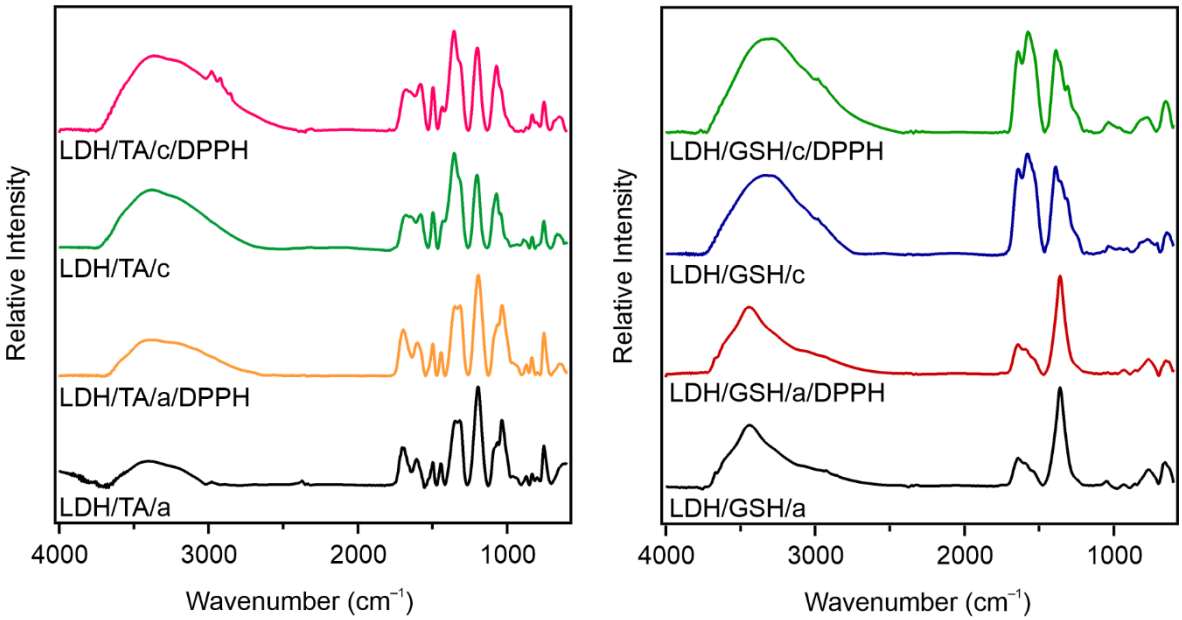

Figure S9. IR spectra of AO loaded samples before and after the reaction in DPPH assay.

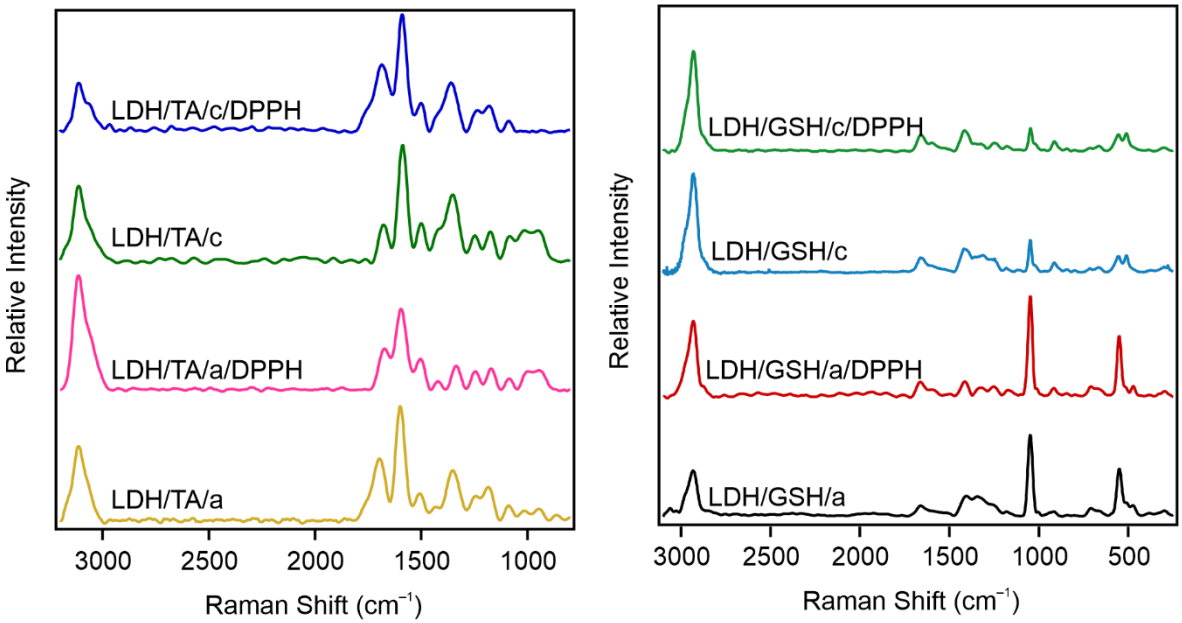

Figure S10. Raman spectra of AO loaded samples before and after the reaction in DPPH assay.

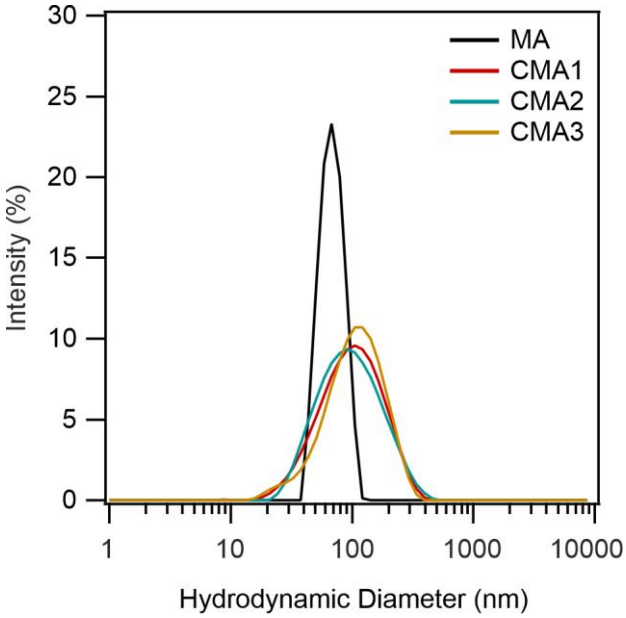

Figure S11. Intensity-weighted hydrodynamic diameter distribution graph of MA and CMA samples.

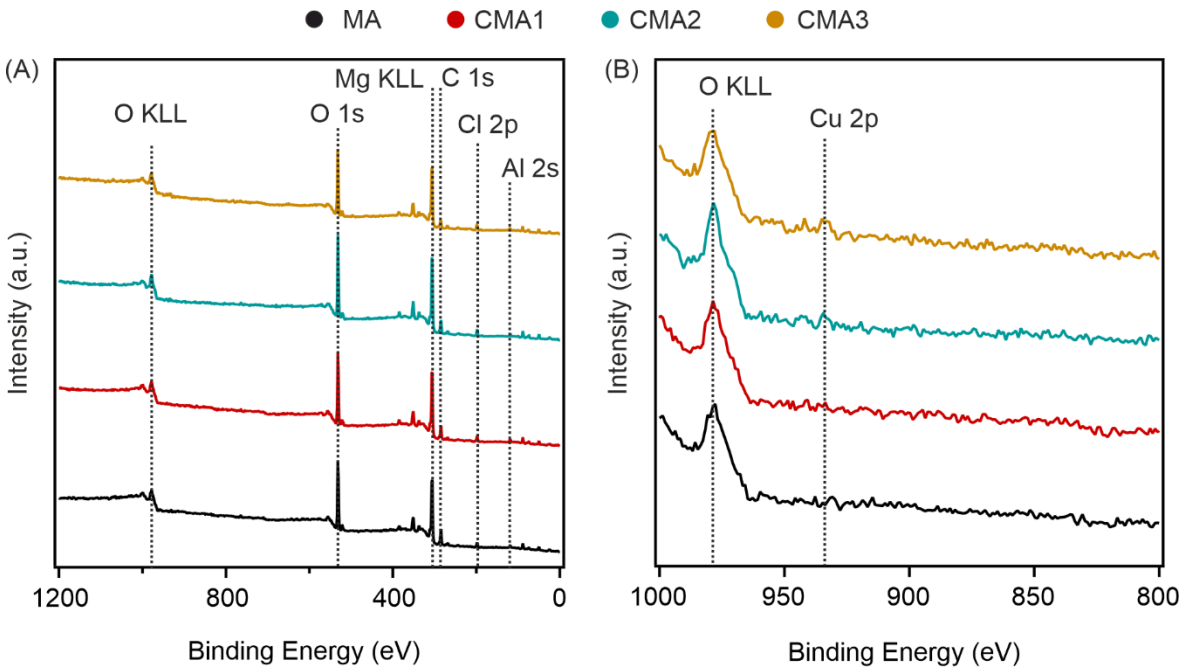

Figure S12. XPS survey scan in 1200 – 0 eV (A) and 1000 – 800 eV (B) range.

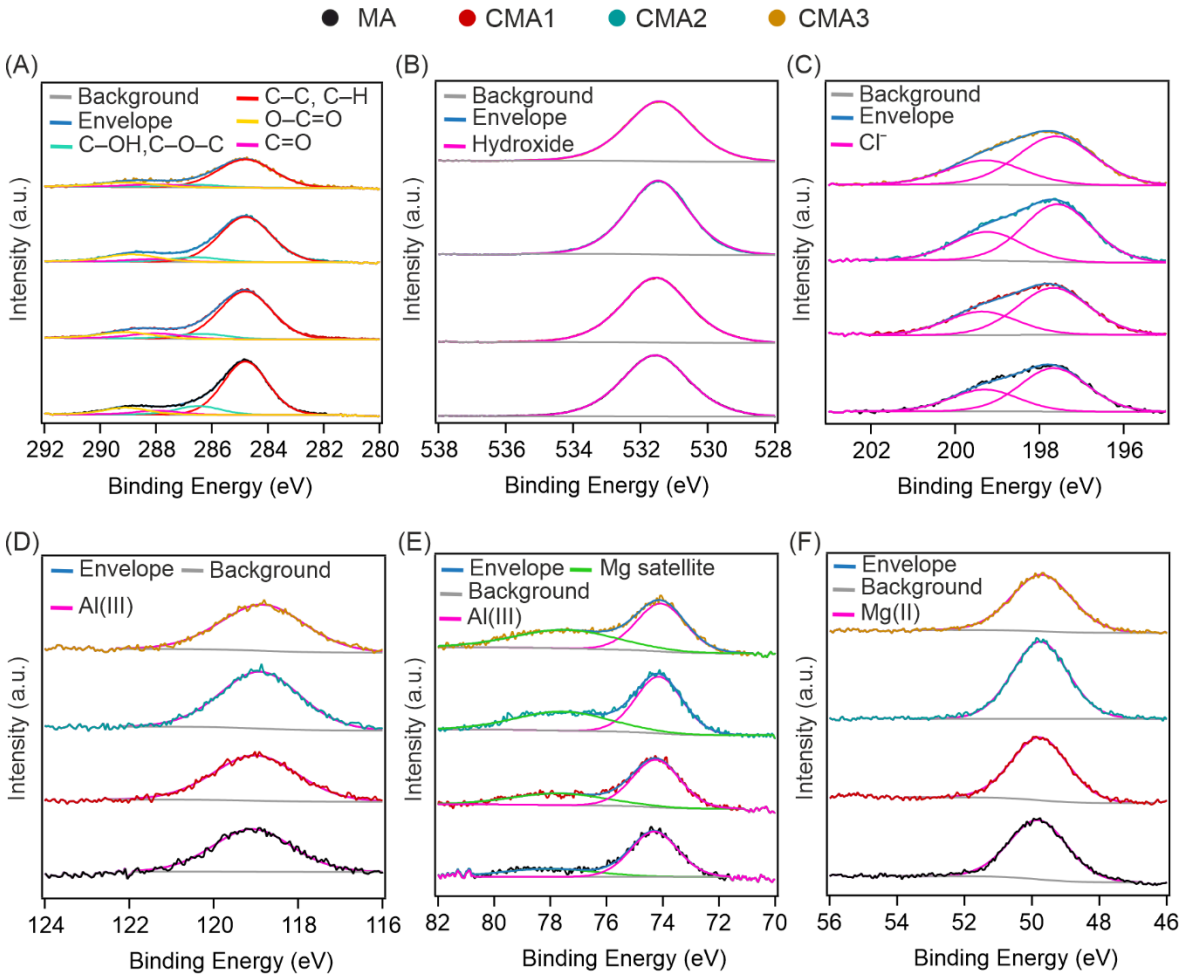

Figure S13. XPS spectra of C 1s (A), O 1s (B), Cl 2p (C), Al 2s (D), Al 2p (E), and Mg 2P (F).

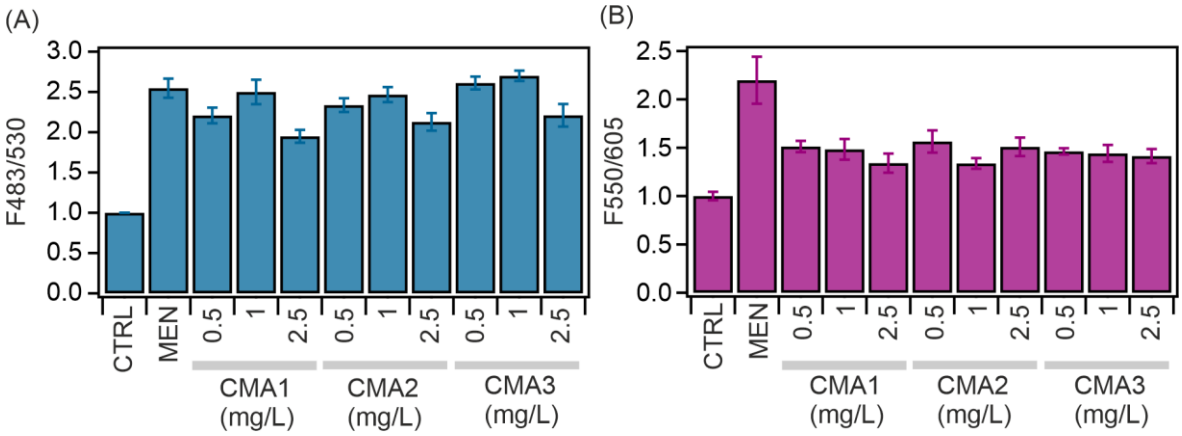

Figure S14. Intracellular ROS scavenging (A) and superoxide radical dismutation (B) activity of CMA samples in 0.5 – 2.5 mg/L concentration range.

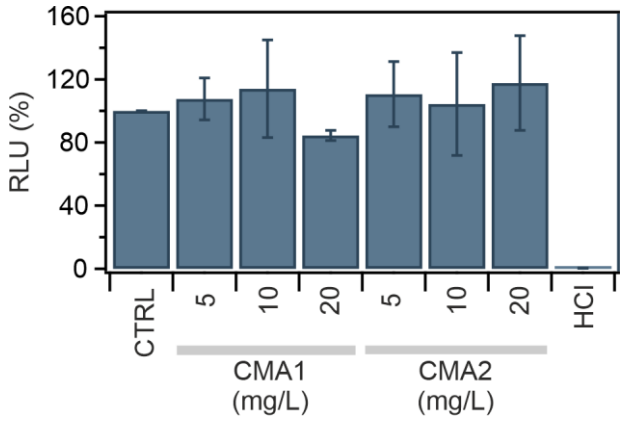

Figure S15. Relative luminescence intensity for CMA1 and CMA2 samples measured in CellTiter Glo® cell viability assay. The test was revealed in 5 – 20 mg/L nanozyme concentration range.